

PN-AACW-994

49916

3860465

OPTICAL AND THERMAL ANALYSIS
OF
PARABOLIC TROUGH SOLAR
COLLECTORS FOR TECHNICALLY
LESS DEVELOPED COUNTRIES

TECHNICAL REPORT 1

by

Halil M. Güven

Richard B. Bannerot

Mechanical Engineering Department
University of Houston - University Park
Houston, Texas 77004

June, 1984

Any opinions, findings, conclusions or recommendations expressed in this publication are those of the author(s) and do not necessarily reflect the views of the U.S. Agency for International Development (USAID).

OPTICAL AND THERMAL ANALYSIS OF
PARABOLIC TROUGH SOLAR COLLECTORS
FOR TECHNICALLY LESS DEVELOPED
COUNTRIES

TECHNICAL REPORT 1

Prepared by: Halil M. Güven,
Research Associate

Approved by: Richard B. Bannerot,
Principal Investigator

Prepared as part of the project,
"Medium Temperature, High Efficiency
Tracking and Non-tracking Solar Energy
Collectors for Rural and Industrial
Applications" for the Agency for
International Development under the
Agreement for Projects under USAID
Grant Agreement Dated August 26, 1978
between the President of India and
USAID for Technologies for the Rural
Poor.

USAID Project Grant No. 386-0465

June, 1984

Acknowledgements

This work was supported by United States Agency for International Development (USAID). The assistance given by the staff of Sandia National Laboratories - Albuquerque, N.M., is acknowledged. In particular, cooperation of Jim Banas, Arthur C. Ratzel and George W. Treadwell in obtaining EDEP computer code is appreciated.

Halil M. Güven

Richard B. Bannerot

Executive Summary

With the continued escalation of costs for traditional sources of energy, a need exists for low cost alternate energy systems to meet the energy needs of the industrialized as well as the developing nations of the world. This need is especially pronounced in countries that have no indigeneous oil resources and, consequently, rely on imported oil. Energy from the sun is abundant in many parts of the world, and solar energy systems definitely appear to have potential for providing low cost energy, especially for low to medium temperature applications such as home heating and industrial process heat.

In the U.S. and other industrialized countries where solar know-how and technology exists, however, at present solar energy is cost-effective for only a limited number of applications (e.g., domestic hot water). The situation, on the other hand, appears to be more favorable in the developing countries. The major share of the cost of solar energy lies in repayment of the initial capital investment for the installed cost of the conversion system that can transform insolation into a form of energy that can perform useful tasks. As much as 60 percent of the large initial expense of the solar energy conversion systems is for labor. Since labor costs in the developing countries are much lower than in the industrially developed countries, the installed cost of a solar system can be considerably less.

The use of parabolic trough solar collectors (PTCs, which are capable of supplying thermal energy over a wide range of

temperatures and presently are the leading solar technology in the intermediate temperature range) in developing country energy applications is investigated in this study. It is found that in the U.S., where most of the PTC research has been performed and the present PTC state-of-the-art has been developed, the main design objectives have been the 'maximization of thermal efficiencies' and 'mass production suitability'. These criteria, however, were found to be incompatible with the goals and design objectives of most developing countries, which favor labor-intensive designs and production techniques. Consequently, it is concluded that in order to be cost-effective, different 'optimum' PTC designs should be developed for different environments.

In this report, the first of two covering the analysis and design of PTC's, the existing analysis techniques for modeling PTC performance (developed in the U.S. mostly) are reviewed and their utilizability in analyzing the performance of PTC designs for developing countries are discussed. It is found that existing analytical techniques incorporated restrictive assumptions. For example, gross errors in manufacture, assembly and operation were assumed non-existent in optical models; nonetheless, this is a valid assumption for the U.S. design environment as it is a high technology design/production environment. New analytical models are developed that incorporate the effect of gross errors that may result from poor manufacture/assembly or from labor-oriented production/assembly or lesser technological capabilities. It is found that these new models can be effectively used in the design analysis of PTC's for developing country

energy applications.

The second technical report will emphasize the design synthesis of PTC's for developing countries. The analytical techniques developed herein will be used for developing optimum PTC designs for any given developing country energy application.

Abstract

Proper identification of all possible optical errors (and imperfections) and knowledge of their effects on the optical and overall performance of the trough is vital for the successful design and dimensioning of the trough. Such information would enable a designer to determine 'how much error is too much?' and to choose realistic values for error parameters (i.e., acceptable error tolerances) to carry out the preliminary design of troughs in an efficient manner.

The need for detailed knowledge of the effect of various errors and an effective method for determination of realistic error tolerances becomes much more apparent when one looks at the problem of designing parabolic troughs for production and use in technically less advanced design environments such as developing countries. In such environments, parabolic trough design goals and objectives may include:

- . Utilizing designs which require small capital investment in new production facilities and depend heavily on local labor.
- . Utilizing locally available materials and technology with minimum dependence on imported materials and components.
- . Employing designs that require no sophisticated maintenance.

However, the preferred labor-oriented production techniques may limit the quality and precision of the final product and result in parabolic troughs with 'less-than-maximum' optical and thermal efficiencies. Moreover, use of unskilled labor in production may

give rise to gross errors that may not be expected in technically advanced design environments. Therefore, when designing collectors for developing country environments, it is increasingly important for the designer to be fully aware of all potential errors and their effects on the performance, and design and dimension the trough accordingly, i.e., with built-in tolerances.

In the optical model presented here, potential optical errors are divided into two groups as random and non-random errors. Small-scale slope errors, mirror nonspecularity, apparent changes in sun's width, and small occasional tracking errors are classified as random errors and they are combined into a single random error parameter, σ , standard deviation of the effective error distribution. Reflector profile errors, misalignment of the receiver with the effective focus of the reflector, and misalignment of the trough with the sun are classified as non-random error parameters: non-random tracking error, β , and non-random receiver mislocation error, $(d_r)_y$. It is shown that the fraction of rays incident on the collector aperture that is intercepted by the absorber (i.e., intercept factor, γ) is then a function of both random and non-random errors as well as the collector geometry parameters such as concentration ratio (C) and rim angle (ϕ). Three error parameters universal to all collector geometries, universal error parameters, which combine random and non-random errors with collector geometry parameters are introduced. The universal error parameters are made up of one universal random error parameter, σ^* ($= \sigma C$), and two universal non-random error parameters, β^* ($= \beta C$) and d^* ($= (d_r)_y / D$, where D is absorber diameter). A detailed ray-trace computer routine which maps rays from elemental reflector surfaces to absorber surface is

used to validate the existence of the universal error parameters.

It is shown that the universal error parameters allow for comprehensive optical analysis of the parabolic troughs; the effect of the random and non-random errors on the performance of the trough can be summarized in universal design curves in the form of intercept factor versus universal error parameters for a given rim angle. The optical performance of the trough is found to be sensitive to both random and non-random errors. The optimum rim angle based on random errors alone is found to be broad (in the range of 80° to 120°). The optimum rim angle based on both random and non-random errors is found to be in the range of 105° to 120° . It is concluded that the results of this optical analysis can be used in comprehensive preliminary design studies for any given design environment.

A comprehensive thermal analysis model is also presented. A one-dimensional heat transfer model for the thermal analysis of the receiver subsystem is adopted. It is shown that this model can be used to calculate a heat-loss parameter q_L in Watts per m^2 of receiver surface area to characterize the thermal behavior of the receiver. It is shown that the presented thermal analysis can be used to size the annulus gap size. The method developed can be used in a comprehensive design and optimization method.

OPTICAL AND THERMAL ANALYSIS OF PARABOLIC TROUGH SOLAR COLLECTORS FOR TECHNICALLY LESS DEVELOPED COUNTRIES

TABLE OF CONTENTS

	<u>Page</u>
Acknowledgements	iii
Executive Summary	iv
Abstract	vii
Table of Contents	x
List of Symbols	xii
List of Figures	xvi
List of Tables	xxi
<u>Chapter 1</u> GENERAL INTRODUCTION	1
1.1 Background	1
1.2 Industrialized versus Developing Countries	4
1.3 Literature Survey and Discussion	5
1.4 Objectives and Outline of the Study	8
<u>Chapter 2</u> OUTLINE OF A COMPREHENSIVE PERFORMANCE SIMULATION MODEL FOR PARABOLIC TROUGHS	11
<u>Chapter 3</u> METHODS FOR MODELING ERRORS IN MANUFACTURE, ASSEMBLY AND OPERATION	15
3.1 Introduction	15
3.2 Optical Efficiency	16
3.3 Modeling Intercept Factor for On-Axis Operation	17
3.4 Description of Optical Errors	21
3.5 Analytical Techniques for Modeling Incident Sunshapes and Effective Sunshapes	29

	<u>Page</u>
3.5.1 Solar Irradiance Profile -- Incident Sunshape	29
3.5.2 Reflected Beam Profile -- Effective Sunshape	31
3.5.3 Analysis of Optical Errors	38
Statistical Error Analysis	39
Comprehensive Error Analysis	42
3.6 Effect of Off-Axis Operation	50
3.7 Summary	52
<u>Chapter 4</u> PRELIMINARY OPTICAL RESULTS AND DERIVATION OF UNIVERSAL ERROR PARAMETERS	53
<u>Chapter 5</u> RESULTS OF THE COMPREHENSIVE OPTICAL ANALYSIS	78
5.1 Introduction	78
5.2 Results of Optical Analysis with Random Errors Alone	79
5.3 Results of Optical Analysis with Random and Non-random Errors	82
5.4 Sensitivity of Error Tolerances to Changes in Rim Angle -- Optimal Rim Angles	98
5.5 Summary	104
<u>Chapter 6</u> THERMAL ANALYSIS OF PARABOLIC TROUGHS	106
6.1 Introduction	106
6.2 Description of the Problem and Assumptions	107
6.3 One-Dimensional Heat-Loss Model	110
6.4 Calculation of Heat-Loss Parameter q_L	116
6.5 Annulus Gap Sizing	118
6.6 Summary	121
<u>Chapter 7</u> CLOSURE	122
REFERENCES	124

LIST OF SYMBOLS

A_a	Reflector aperture area
A_{ij}	j_{th} attribute rating for the i_{th} alternative; a numerical value associated with an attribute of a particular alternative
A_j^{max}	Maximum attribute rating of attribute j
A_j^{min}	Minimum attribute rating of attribute j
A_r	Absorber tube area
C	Concentration ratio, $C = W/\pi D$
C_o	Optimum concentration ratio
C'_o	Optimum concentration ratio for sensitivity analysis
$\langle \cos \theta \rangle$	All-day average incidence factor
C_p	Specific heat at constant pressure
D	Absorber tube diameter
$D_{g,i}$	Diameter of inner surface of glass jacket (glazing)
$D_{g,o}$	Diameter of outer surface of glass jacket (glazing)
d_r	Distance between the actual focus and the center of the absorber tube
$(d_r)_x$	d_r along the lateral axis of the reflector
$(d_r)_y$	d_r along the optical axis of the reflector
d^*	Universal non-random error parameter due to receiver mislocation ($= (d_r)_y/D$)
d_i^+	Amount by which constraint i has exceeded goal (overachievement)

List of Symbols (Continued)

d_i^-	Amount by which constraints i is short of goal (underachievement)
f	Focal length of the reflector
g	Acceleration due to gravity
h_w	Heat-transfer coefficient due to wind
H_d/H_h	Ratio of diffuse to hemispherical irradiation
I_b	Beam solar irradiation
$\langle I_b \rangle$	All-day average beam insolation
$\langle I_b \cos\theta \rangle$	All-day average beam insolation and incidence factor product
k_{air}	Thermal conductivity of air
k_{ef}	Effective conduction coefficient due to conduction and natural convection in an annular space
k_{gas}	Thermal conductivity of the gas in the annular space of the receiver
k_{glass}	Thermal conductivity of glass
K_h	Sky clearness index
$K(\theta)$	Incidence angle modifier (see Eq. 3.2)
$\langle K(\theta) \rangle$	All-day average incidence angle modifier
ℓ	Annular gap width
L	Absorber tube length
\dot{m}	Working fluid flow rate
P_i	Priorities of goals; their subscripts serve to identify priority level for the goals
q_L	Heat loss per receiver surface area

List of Symbols (Continued)

q_{net}	Net heat flux absorbed by the absorber
$\langle q_{\text{net}} \rangle$	All-day average net heat flux absorbed by the receiver
\dot{Q}	Heat loss rate
R_{ij}	Normalized j_{th} attribute rating for the i_{th} alternative
T_a	Ambient temperature
T_{abs}	Absorber temperature (collector operating temperature)
T_{fin}	Inlet temperature of working fluid
T_{fout}	Outlet temperature of working fluid
$T_{g,i}$	Temperature of inner surface of glazing
$T_{g,o}$	Temperature of outer surface of glazing
U_L	Heat-loss coefficient for receiver based on absorber surface area
V_{wind}	Wind velocity
W	Reflector aperture width

Greek Symbols

α	Absorptance of selective coating
β	Reflector misalignment and tracking error angle (see Figure 3.3)
β^*	Universal non-random error parameter due to angular errors ($= \beta C$)
γ	Intercept factor at normal incidence
γ_o	Optimum intercept factor
γ_θ	Instantaneous (incidence angle dependent) intercept factor
δ	Solar declination angle

List of Symbols (Continued)

ϵ_{abs}	Emissivity of selective coating
$\epsilon_{g,i}$	Emissivity of glazing inner surface
$\epsilon_{g,o}$	Emissivity of glazing outer surface
ζ	Half optical cone angle (angular aperture)
η_o	Optical efficiency (see Eq.3.1)
$\langle \eta_c \rangle$	All-day average collector efficiency
$(\eta_c)_{noon}$	Overall collector efficiency at solar noon
θ	Angle of incidence of the sun's rays on the collector aperture measured from the normal to trough aperture
θ_{\perp}	Incidence angle projected to x-y plane (see Fig.3.1)
θ_{\parallel}	Incidence angle projected to y-z plane (see Fig.3.1)
θ_c	Incidence angle on the aperture at the cut-off time
θ_{noon}	Incidence angle at solar noon
λ	Latitude
μ	Angular shift of the mean of the standard distribution (see Eq.3.18)
ρ	Average specular reflectance of the reflecting surface
σ	Energy distribution standard deviation
σ^*	Universal random error parameter ($= \sigma C$)
τ	Transmissivity of the glass jacket
$(\tau\alpha)_n$	Effective transmittance-absorptance factor at normal incidence
ϕ	Trough rim angle (see Fig.2.1)
ω	Hour angle (subscript c designates hour angle at cut-off time).

LIST OF FIGURES

<u>Figure</u>	<u>Title</u>	<u>Page</u>
1.1	Temperature Ranges Attainable with Different Solar Technologies.....	2
2.1	Common Terminology of Parabolic Trough Collectors.	12
3.1	Definition of Coordinates and Projected Incidence Angles for Two-Dimensional Reflectors.....	18
3.2	Idealized Central Ray Optics of Parabolic Troughs.....	20
3.3	Description of Potential Optical Errors in Parabolic Trough Collectors.....	22
3.4	Schematic Representation of a Parabolic Mirror Surface Showing the Difference Between Slope Errors and Reflector Profile Errors.....	24
3.5	Ray Traces of Reflection from Perfect and Imperfect (Random) Mirror Surfaces Showing Perfectly Reflected Central Ray s_n and Imperfectly Reflected Central Ray s'_n	25
3.6	Schematic Representation of a Mirror Surface Showing the Difference Between Slope Errors and the Mirror Diffusivity.....	27
3.7	Abstract Representation of Scattering by Reflection.....	32

List of Figures (Continued)

<u>Figure</u>	<u>Title</u>	<u>Page</u>
3.8	Modeling of Potential Optical Errors in Parabolic Trough Collectors.....	44
3.9	Combination of Receiver Location and Parabola Profile Errors.....	49
4.1	Intercept Factor as a Function of Receiver Mislocation Along the Lateral Axis and Tracking Error for $\sigma = 0.0025$ radian.....	55
4.2	Intercept Factor as a Function of Receiver Mislocation Along the Lateral Axis and Tracking Error for $\sigma = 0.01$ radian.....	56
4.3	Intercept Factor as a Function of Receiver Mislocation Along the Lateral Axis and Tracking Error for $\sigma = 0.02$ radian.....	57
4.4	Intercept Factor as a Function of Receiver Mislocation Along the Optical Axis and Tracking Error for $\sigma = 0.0025$ radian.....	59
4.5	Intercept Factor as a Function of Receiver Mislocation Along the Optical Axis and Tracking Error for $\sigma = 0.01$ radian.....	60
4.6	Intercept Factor as a Function of Receiver Mislocation Along the Optical Axis and Tracking Error for $\sigma = 0.02$ radian.....	61
4.7	Intercept Factor as a Function of Tracking Error and Random Errors for $(d_r)_y = 0.0$ and 0.508 cm.....	63
4.8	Intercept Factor as a Function of Tracking Error and Random Errors for $(d_r)_y = 1.016$ and 1.424 cm.....	64
4.9	Intercept Factor as a Function of Concentration Ratio and Random Error Parameter (Zero Non-Random Errors).....	65
4.10	Intercept Factor as a Function of the universal Random Error Parameter (Zero Non-Random Errors)...	67

List of Figures (Continued)

<u>Figure</u>	<u>Title</u>	<u>Page</u>
4.11	Intercept Factor as a Function of Concentration Ratio and Tracking Error for $\sigma^* = 0.05$ radian and $(d_r)_y = 0.0$	68
4.12	Intercept Factor as a Function of Concentration Ratio and Tracking Error for $\sigma^* = 0.10$ radian and $(d_r)_y = 0.0$	69
4.13	Intercept Factor as a Function of Concentration Ratio and Tracking Error for $\sigma^* = 0.20$ radian and $(d_r)_y = 0.0$	70
4.14	Intercept Factor as a Function of the Universal Non-Random Error Parameter due to Angular Errors (β^*) and Various Random Error Levels (Zero Receiver Location Error)....	71
4.15	Intercept Factor as a Function of Concentration Ratio and Receiver Mislocation for $D = 1.27$ cm.....	72
4.16	Intercept Factor as a Function of Concentration Ratio and Receiver Mislocation for $D = 2.54$ cm.....	73
4.17	Intercept Factor as a Function of Receiver Diameter and Receiver Location Error.....	74
4.18	Intercept Factor as a Function of the Universal Non-Random Error Parameter due to Receiver Mislocation.....	75
5.1	Intercept Factor as a Function of the Universal Random Error Parameter and rim angle (Zero Non-Random Errors).....	80
5.2	Intercept Factor Versus Rim Angle and the Universal Random Error Parameter (Zero Non-Random Errors).....	31
5.3	Qualitative Representation of Intercept Factor as a Function of the Non-Random Error Parameters for Fixed Rim Angle and Various Value of Random Error Parameters.....	83
5.4	Allowable Non-Random Error Levels for $\gamma = 0.95$ and $\phi = 80^\circ$ and Various Random Error Levels....	84

List of Figures (Continued)

<u>Figure</u>	<u>Title</u>	<u>Page</u>
5.5	Allowable Non-Random Error Levels for $\gamma = 0.95$ and $\phi = 90^\circ$ and Various Random Error Levels.....	85
5.6	Allowable Non-Random Error Levels for $\gamma = 0.95$ and $\phi = 100^\circ$ and Various Random Error Levels.....	86
5.7	Allowable Non-Random Error Levels for $\gamma = 0.95$ and $\phi = 110^\circ$ and Various Random Error Levels.....	87
5.8	Allowable Non-Random Error Levels for $\gamma = 0.95$ and $\phi = 120^\circ$ and Various Random Error Levels.....	88
5.9	Allowable Non-Random Error Levels for $\gamma = 0.75$ and $\phi = 80^\circ$ and Various Random Error Levels.....	89
5.10	Allowable Non-Random Error Levels for $\gamma = 0.75$ and $\phi = 90^\circ$ and Various Random Error Levels.....	90
5.11	Allowable Non-Random Error Levels for $\gamma = 0.75$ and $\phi = 100^\circ$ and Various Random Error Levels.....	91
5.12	Allowable Non-Random Error Levels for $\gamma = 0.75$ and $\phi = 110^\circ$ and Various Random Error Levels.....	92
5.13	Allowable Non-Random Error Levels for $\gamma = 0.75$ and $\phi = 120^\circ$ and Various Random Error Levels.....	93
5.14	Effect of Rim Angle on the Allowable Non-Random Error Levels for $\sigma^* = 0.1$ rad.....	95
5.15	Effect of Rim Angle on the Allowable Non-Random Error Levels for $\sigma^* = 0.2$ rad.....	96
5.16	Effect of Rim Angle on the Allowable Non-Random Error Levels for $\sigma^* = 0.35$ rad. and $\gamma = 0.75$	97
5.17	Allowable Non-Random Error Level d^* as a Function of Rim Angle and β^* for $\sigma^* = 0.2$ and for $\gamma = 0.95$ and 0.75	99
5.18	Allowable Non-random Error Level d^* as a Function of Rim angle and β^* for $\sigma^* = 0.3$ and $\gamma = 0.75$	100
5.19	Allowable Non-Random Error Level d^* as a Function of Rim Angle and β^* for $\sigma^* = 0.4$ and $\gamma = 0.75$	101

List of Figures (Continued)

<u>Figure</u>	<u>Title</u>	<u>Page</u>
5.20	Allowable Random Error Level d^* as a Function of Rim Angle and β^* for $\sigma^* = 0.0$ and $\gamma = 0.95$ and 0.75	102
5.21	Allowable Non-Random Error Level β^* as a Function of Rim Angle and σ^* for $d^* = 0.0$ and $\gamma = 0.95$ and 0.75	103
6.1	Cross Section of Receiver Subsystem.....	108
6.2	Two-Dimensional Energy Exchange to the Working Fluid [40].....	108
6.3	One-Dimensional Receiver Heat-Loss Model.....	111
6.4	Wind Induced Heat-Loss from Receiver.....	115
6.5	Heat-Loss Coefficient U_L as a Function of Average Absorber Tube Temperature and Absorber Tube Diameter.....	117
6.6	Annulus Gap Sizing for Alternate Gases using a 2.54 cm Absorber Tube for an Absorber Temperature of 315°C	120
6.7	Annulus Gap Sizing for an Absorber Temperature of 200°C	121

LIST OF TABLES

<u>Table</u>	<u>Title</u>	<u>Page</u>
3.1	Summary of Potential Errors	28
3.2	Typical Focal Lengths and Slope Errors for Model Parabolas of Various Materials and Processes	45
6.1	Reference Trough Receiver Design Parameters	117

Chapter One

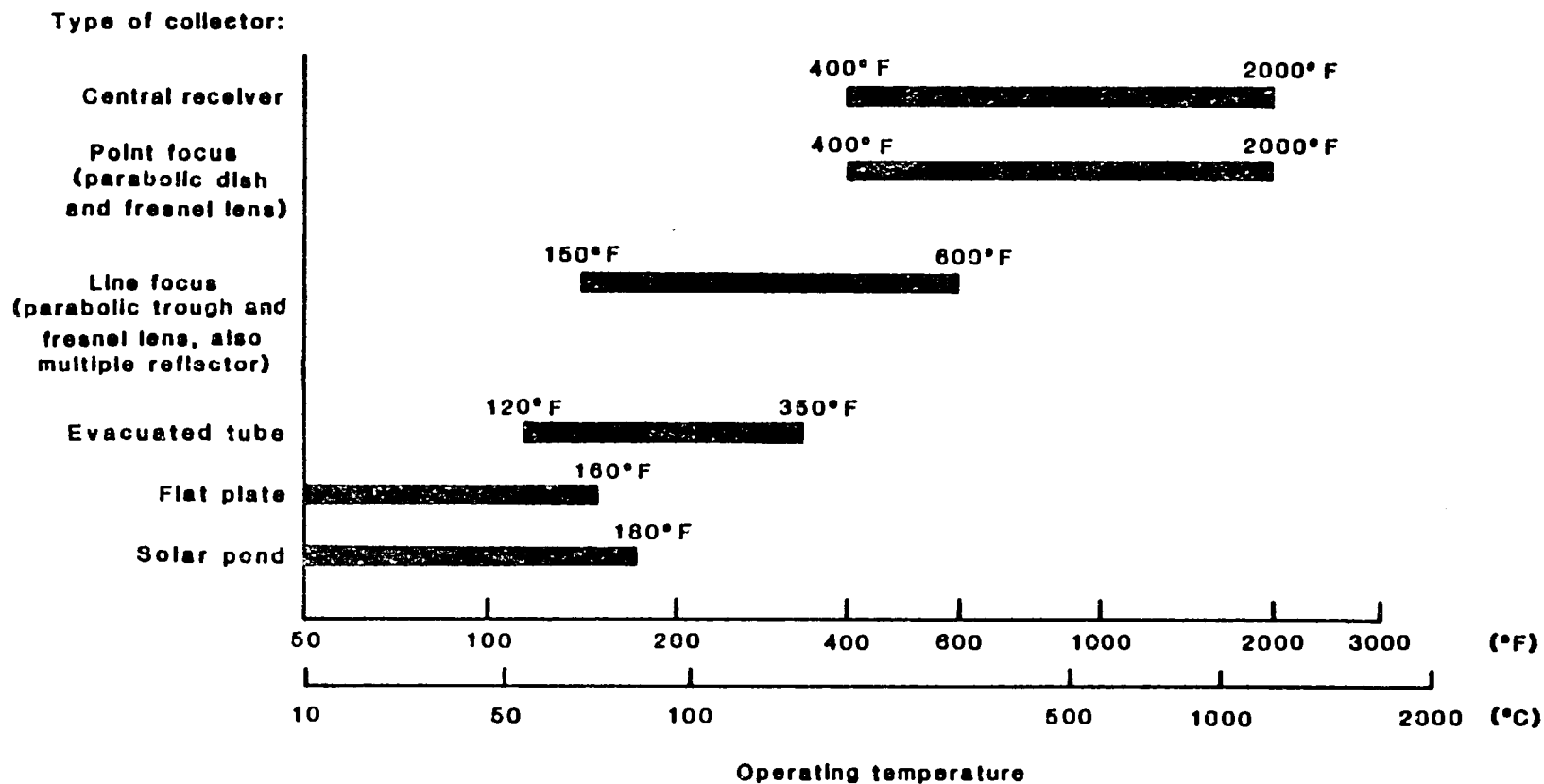
GENERAL INTRODUCTION

1.1 Background

The continuing expansion of fossil fuel reserve estimates in the 1960's, lulled the world into a false sense of energy security. During this period, the U.S. and other industrialized nations of the west based their entire economic growth on the nonrenewable energy resources and the developing countries of the world followed their lead by initiating many fossil-fuel-intensive development programs to accelerate agricultural production through the use of irrigation, chemical fertilizers and hybrid seeds, and to provide for industrial development through rural electrification and road construction. Nevertheless, the energy crisis of 1973 and the subsequent ten-fold increase in oil prices has greatly decreased the attractiveness of many fossil-fuel-intensive development and economic growth programs in both industrialized and developing countries.

In response to the energy crisis, interest in solar energy and other alternative energy sources was intensified and the development of indigenous fossil fuel resources, conservation programs, improvements in energy conversion and efforts to utilize renewable sources were initiated. This intensified research and development in renewable energy sources resulted in the demonstration of the technical feasibility of many alternative energy options. The attainable temperature ranges for various technically feasible solar energy utilization systems [1,2]^{*} are shown in Figure 1.1. Nonetheless, in the U.S. where solar know-how and

^{*} Numbers in brackets refer to references in Reference section.



Note: Line-focus, evacuated tube, and flat-plate collectors are commercially available; central receivers, pointfocus collectors and solar ponds are still being developed.

Figure 1.1 Temperature ranges attainable with different solar technologies (from Reference 2).

technology exists, at present, solar energy is cost-effective for only a limited number of applications (e.g., domestic hot water) [2,3]. The economic value of a solar energy utilization system, is equivalent to the incremental cost of the cheapest competing energy source that supplies the energy to accomplish the same task as the solar system. At the present time with government orchestrated energy pricing policies, tax-exemptions, etc., especially favorable to conventional energy, it is difficult to make a true cost estimate. However, rough estimates of collection efficiencies, material costs, heat exchange efficiencies, etc., recently indicate that in the U.S., for example, thermal energy from a solar system would cost more than that from a conventional source.

The situation, however, appears to be more favorable in developing countries. The major share of the cost of solar energy lies in repayment of the initial capital investment for the installed cost of the conversion system that can transform insolation into a form of energy that can perform useful tasks. As much as 60 percent of the large initial expense of the solar energy conversion systems is for labor [4]. Since labor costs in the developing countries are much lower than in industrially developed countries, the installed cost of a solar system could be considerably less. Furthermore, since many developing countries have no indigenous oil resources, the price of the cheapest competing energy source, which is usually imported oil, is considerably higher than, for example, in the U.S. Thus, a solar industry,

utilizing local labor and materials as much as possible, may be cost-effective today or in the near future for many applications in developing countries.

1.2 Industrialized versus Developing Countries

Of the existing solar technologies (Figure 1.1), parabolic trough and flat plate collectors have a more-or-less fully developed technology, and they are commercially available in the U.S. Parabolic Trough Collectors (PTC's) are capable of supplying thermal energy over a wide range of temperatures (up to about 300°C), and therefore they can be used for a variety of applications ranging from electricity for rural applications (agricultural pumping) all the way to industrial hot water and steam production. Consequently, at present, they are the best candidates for widespread use in developing country energy applications.

In mounting an effort to encourage the utilization of PTC's in developing country energy applications, however, it is important to be fully aware of the differences in design philosophy and design objectives between industrialized and developing countries. In an industrialized environment* like the U.S., design goals and objectives for PTC's included [5]:

- . High performance -- thermal efficiencies of 60-70%
at 600°F (305°C);

*Throughout this text 'environment' is defined as a country (or region) with certain given economic and technical capabilities.

- . Designs suitable for mass-production;
- . Low-costs achieved with low-labor, mass-production materials and processes.

On the other hand, in a semi-industrialized and technically less advanced environment (e.g., developing countries), design goals and objectives for PTC's include the use of:

- . designs which require small capital investment in new production facilities and raw material and which depend heavily on local labor;
- . locally available materials and technology with minimum dependence on imported materials and components;
- . designs that require no sophisticated maintenance.

The problem is then to satisfy the goals and objectives of designs in developing countries with an 'information base' derived from industrialized countries. However, an important question that needs to be answered first is:

- . Is the current 'information base' in PTC technology comprehensive and flexible enough to be used in developing PTC designs suitable for developing country energy applications?

The answer to this question is given in the next section.

1.3 Literature Survey and Discussion

An extensive search of the literature and communication with the researchers in the world's leading laboratory in PTC technology, Sandia National Laboratories, Albuquerque, N.M.,

unveiled a wealth of scientific information on PTC analyses and performance evaluations (e.g., [6-14]). These included numerous studies on optical and thermal analyses as well as studies on manufacturing techniques, selective coatings, methods for reducing slope errors, flexible hose design, materials improvement, wind loading, etc.

After carefully studying the available literature, it was concluded that state-of-the-art PTC modeling was not comprehensive enough to be utilized for performance simulations in a comprehensive design method which would incorporate changes in the design environment. Therefore, the answer to the question posed in the preceding section is no. The reasons for the deficiencies that existed in the PTC analysis models at the beginning of this investigation are discussed in the following paragraphs.

As a direct consequence of the 'low-labor mass-production' goal of the U.S. design environment, research efforts were invested in the development of one 'standardized' PTC design for all applications and geographic locations throughout the U.S. The 'transportable', 'standard' PTC design concept is emphasized in almost all the available studies. For example, Treadwell [14], in a study investigating the influence of geographic location on the PTC performance, stated:

"... a single-axis tracking parabolic trough solar collector could have a common optimum design for use in all regions of the U.S. This determination has an impact upon mass-production of troughs since different

geometric configurations might be optimum for different regions of the U.S. and could result in multiple production lines and controlled distribution. Neither is necessarily compatible with the desired cost reductions that could result from large volume production."

Subsequently, this design objective led to the development of performance simulation models which were almost specifically tailored for design analysis of a very limited number of PTC geometries. For example, Sandia researchers chose a 2m-aperture width 90°-rim angle reflector and a 2.5cm-diameter cylindrical receiver with selective coating for their 'high-quality' PTC design in 1976 [15] and this design formed the basis for all of their subsequent studies and modeling (e.g., [13,14]). A fundamental study to develop comprehensive mathematical models which could be used for all collector geometries was not undertaken.

In developing country design environments:

- . Big mass-production facilities and large-volume production (which require efficient transportation-distribution systems too) may be out of question. Instead, small-scale labor-intensive, 'distributed production shops' may play a more important role in cost-effectiveness and hence widespread use of PTC's. Therefore, different geometric configurations can be considered for different locations (just the opposite of the ONE optimum design philosophy

stated above). In fact, in such environments 'redesigning' PTC's for different applications and locations may be a must to compensate for performance reductions resulting from poor manufacture and/or poor maintenance. Therefore, it is desirable to have simulation models that can analyze different collector geometries.

- . The preferred labor-oriented production techniques and lesser technological capabilities will limit the quality and precision of the final product and also introduce gross optical errors. Therefore, when designing PTC's for developing country applications, the effect of such errors should be accounted for in the design calculations. (In the state-of-the-art PTC optical model [18], gross errors in manufacture, assembly and operation were assumed non-existent. Nonetheless, this is a valid assumption for the U.S. design environment as it is a high technology design/production environment.)

1.4 Objectives and Outline of the Study

The main objectives of the work to be presented in this report can therefore be stated as follows:

1. To develop a comprehensive PTC optical model which incorporates the effect of gross errors.

2. To develop a comprehensive performance model, including both optical and thermal effects, which can be used to analyze different collector geometries and which can eventually be used in comprehensive design studies to develop 'optimum' PTC designs for developing country design environments.

In Chapter Two, the outline of a 'comprehensive' performance simulation model for PTC's is given. The specific deficiencies that existed in the PTC 'information base' at the beginning of this study are discussed.

In Chapter Three, the first step in the development of a comprehensive optical model for the PTC's is presented. That is, the nature of the gross optical errors in manufacture, assembly and operation are described and techniques are developed for modeling the gross (systematic) errors. Potential errors are classified as random and non-random errors.

In Chapter Four, error parameters universal to all collector geometries are derived and preliminary results from the optical model are presented. The new error parameters are called 'universal error parameters'. Three universal error parameters (one random, σ^* , and two non-random, β^* and d^*) are introduced to characterize the various potential errors. The universal error parameters enable the designer to analyze different geometries.

In Chapter Five, typical results from the comprehensive optical model developed in Chapters Three and Four are presented.

The model is validated by comparing the results with those of the previous investigators. It is concluded that the optical model developed is comprehensive as well as versatile and therefore it can be used in a comprehensive design method to develop optimum collector designs for developing countries.

In Chapter Six, analysis of the thermal behavior of PTC's is presented. Available literature on thermal analysis of PTC's is reviewed and the use of these studies in a comprehensive PTC design method is discussed.

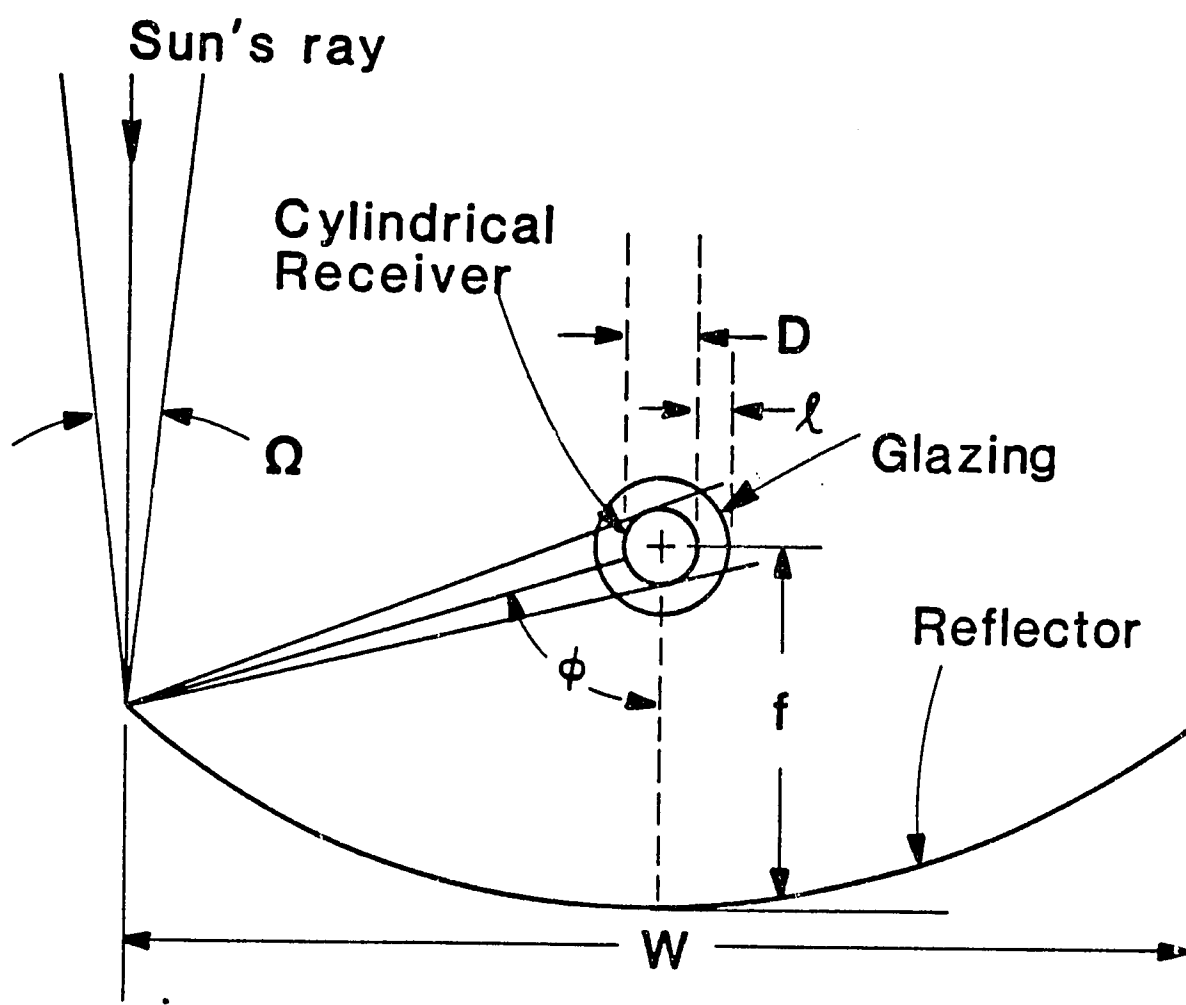
Concluding remarks, discussions and recommendations are given in Chapter Seven.

Chapter Two

OUTLINE OF A COMPREHENSIVE PERFORMANCE SIMULATION MODEL FOR PARABOLIC TROUGHS

A PTC consists of a cylindrical parabolic reflecting surface (reflector), a receiver assembly centered along the reflector's focal line and a tracking mechanism. The receiver assembly usually has two components: an absorber surface and a transparent outer cover (glazing). The collector tracks the sun on a continuous basis focusing the sun's rays onto the absorber surface which becomes heated and transfers energy to the fluid flowing through it. The heat transferred to the fluid can provide energy for many types of practical energy applications. Figure 2.1 presents the common terminology for PTC's.

A PTC performance simulation model consists of two parts: an optical analysis for the reflector system and a thermal analysis for the receiver system. These can be decoupled and hence dealt with separately if the optical properties of the materials used are assumed to be temperature independent. It turns out that in most solar thermal systems, including PTC's, this is an excellent approximation. Therefore, the two analyses, optical and thermal, can be carried out completely independent of each other and this, undoubtedly, brings about a considerable simplification in the performance simulation modeling.



- f = Focal length
- ϕ = Rim angle
- W = Aperture width
- D = Receiver diameter
- Ω = Acceptance angle
- ℓ = Gap width

Figure 2.1 Common terminology of Parabolic Trough Collectors.

With respect to the thermal analysis of cylindrical receivers (with no insulation) , one can find a rather well developed literature which includes extensive experimental data, too. These studies are reviewed and their utilizability in a comprehensive PTC design method are discussed in Chapter Six.

With regard to the optical analysis of PTC's, however, one cannot find a comprehensive 'information base'. The state-of-the-art optical models for PTC's were found to be incomplete (i.e., have restrictive assumptions) and hence were not directly adaptable to a comprehensive PTC design method. As discussed earlier, the major deficiency was found to be in the handling of the optical errors.

In the state-of-the-art optical modeling (e.g., [16]), the optical errors were treated as random processes and their occurrences were represented as normal distributions with zero mean. Gross (large-scale) systematic optical errors, which are more of a rule than exception in low-technology environments, were assumed to be non-existent. This assumption seems to be a valid one for an industrialized, high-technology design environment where a micro-computer controlled tracker, precise manufacturing techniques and sophisticated quality control equipment (e.g., laser ray-trace [17] for assessing the optical quality of the reflector) can be used.

When designing PTC's for low-technology design environments, however, the effect of gross errors in manufacture,

assembly and operation should be incorporated into the collector simulations and accounted for in the design calculations. Therefore, it was concluded that studies were needed to:

- . model the effect of gross (systematic) optical errors;
- . determine the minimum concentration ratio (relative sizes of reflector aperture and absorber tube, $W/\pi D$) that is capable of delivering energy at a specified temperature for given optical error levels;
- . determine trade-offs between accuracy and quality of reflector surface (e.g., slope errors and reflectivity) and efficiency, and between concentration ratio and absorber coating properties.

The following chapters present the development and results of comprehensive optical and thermal analysis models

Chapter Three

METHODS FOR MODELING ERRORS IN MANUFACTURE, ASSEMBLY AND OPERATION

3.1 Introduction

The upper limit to the concentration that a parabolic trough can achieve is set by the sun's width. In practice, however, the average concentration ratio of a trough is degraded to values much below this upper limit due to:

- . apparent changes in sun's width and incidence angle effects;
- . physical properties of the materials used in receiver and reflector construction;
- . imperfections (or errors) that may result from poor manufacture and/or assembly, imperfect tracking of the sun, and poor operating procedures.

Proper identification of all the factors that affect the optical performance and hence precise knowledge of their effects are vital for the successful design and dimensioning of the trough.

In this chapter procedures are presented for modeling the effect of various manufacturing, operational and material imperfections (errors), and hence methods are developed for calculating the intercept factor for different trough geometries having different error levels.

3.2 Optical Efficiency

Instantaneous optical performance of a trough can be measured by the optical efficiency, which is the fraction of incident radiation absorbed by the absorber tube and is expressed as:

$$\eta_o = \rho(\tau\alpha)_{\text{eff}} \gamma_\theta \quad (3.1)$$

where

- ρ = Average specular reflectance of the reflective surface,
- $(\tau\alpha)_{\text{eff}}$ = Effective transmittance-absorptance factor for the receiver,
- θ = Angle of incidence of the sun's rays on the collector aperture,
- γ_θ = Instantaneous intercept factor (defined as the fraction of rays incident upon the aperture that reach the receiver for a given incidence angle θ).

The optical efficiency, η_o , given by Eq.(3.1), varies with angle of incidence between the aperture surface normal and the incoming radiation. There are several factors that contribute to the decrease of optical efficiency with increasing incidence angle. These factors include the incident angular dependence of glazing transmittance and absorptance. Also, the instantaneous intercept factor γ_θ decreases with incidence angle. This decrease is brought about in two ways. First, there is beam spreading due to reflector longitudinal slope and nonspecularity errors. Second, the apparent sun image becomes wider due to the longer reflected path length. Fortunately, the incidence angle effects can be separated out

by using the so-called incidence angle modifier [18], $K(\theta)$. The incidence angle modifier $K(\theta)$ defines how the optical efficiency decrease with incidence angle, relative to the trough's normal incidence optical efficiency. The incidence angle modifier at a given angle θ is defined as [18]:

$$K(\theta) \equiv \frac{[\rho(\tau\alpha)_{\text{eff}}\gamma_{\theta}](\theta)}{(\eta_o)_n} = \frac{(\eta_o)_{\theta}}{(\eta_o)_n} \quad (3.2)$$

where, $(\eta_o)_n$ is the normal incidence optical efficiency and it is expressed as follows:

$$(\eta_o)_n = [\rho(\tau\alpha)_n] \gamma \quad (3.3)$$

where

$(\tau\alpha)_n$ = Effective transmittance-absorptance factor at normal incidence,

γ = Intercept factor at normal incidence,

Therefore, Eq.(3.1) can be rewritten as:

$$\eta_o = [K(\theta)][\rho(\tau\alpha)_n] \gamma \quad (3.4)$$

This definition of the optical efficiency allows a clear distinction of the factors contributing to it. The first bracketed term, accounts for all the incidence angle related effects. The second bracketed term represents the optical effects of the physical properties of the materials used in receiver and reflector construction. The last term, the intercept factor, γ , contains the effects of various manufacturing, operation and materials imperfections/errors.

3.3 Modeling Intercept Factor for On-Axis Operation

In Figure 3.1, the coordinate system chosen for the

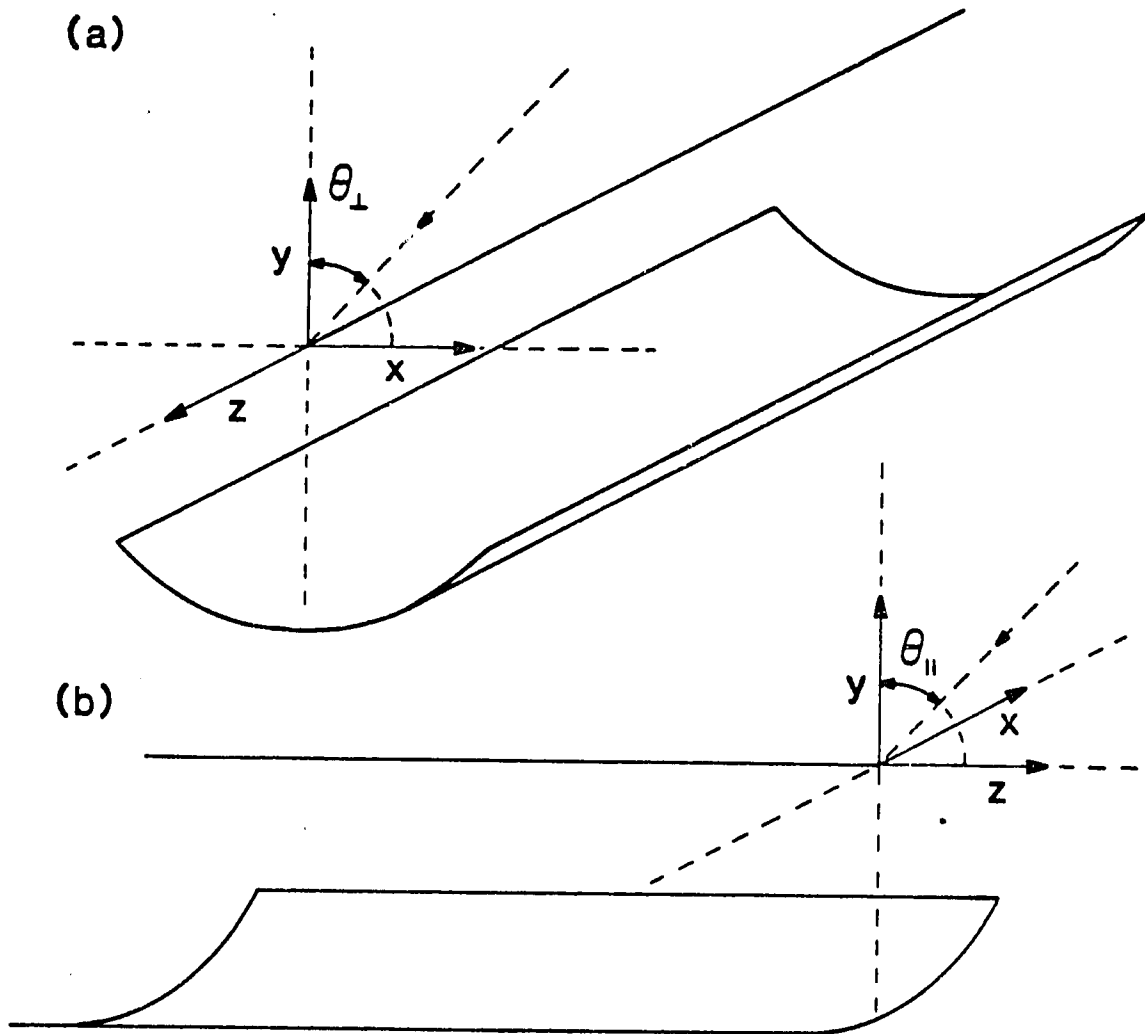


Figure 3.1 Definition of coordinates and projected incidence angles (a) θ_{\perp} and (b) θ_{\parallel} for two-dimensional reflectors (from Ref. 16).

optical analysis of the trough is shown. The z axis is placed along the tracking axis, and y axis along the axis of symmetry or optical axis, as shown in Fig. 3.1. θ_{\perp} and θ_{\parallel} are the projections of the incidence angle of the sun on the x - y plane and on the y - z plane, respectively. With perfect tracking the misalignment angle θ_{\perp} vanishes and θ_{\parallel} equals the incidence angle. The collector is said to be on-axis when the incidence angle is zero, i.e., the direction of the incident central ray from the sun is perpendicular to the aperture plane of the trough. In this section models are presented for the calculation of intercept factors for on-axis operation.

Intercept factor is defined as the fraction of the rays incident on the aperture that are intercepted by the receiver. In this work, γ is defined as a purely geometric quantity without regard to absorption; absorption losses will be accounted for later by a multiplicative factor, the reflectance-transmittance-absorptance product ($\rho\tau\alpha$), as shown in Equation (3.1).

For simplicity, an "ideal" (but nonexistent) situation could be considered where the sun is a point source; there is no atmospheric (aureole) effects; there are no errors in the construction and operation of the system nor optical losses. In this ideal case the central ray from the sun is incident along the direction of the arrow in the Figure 3.2. A light ray would reflect from the trough at P and go toward the focal point O of the parabola. In this case, the intensity distribution of both incident and reflected rays would be

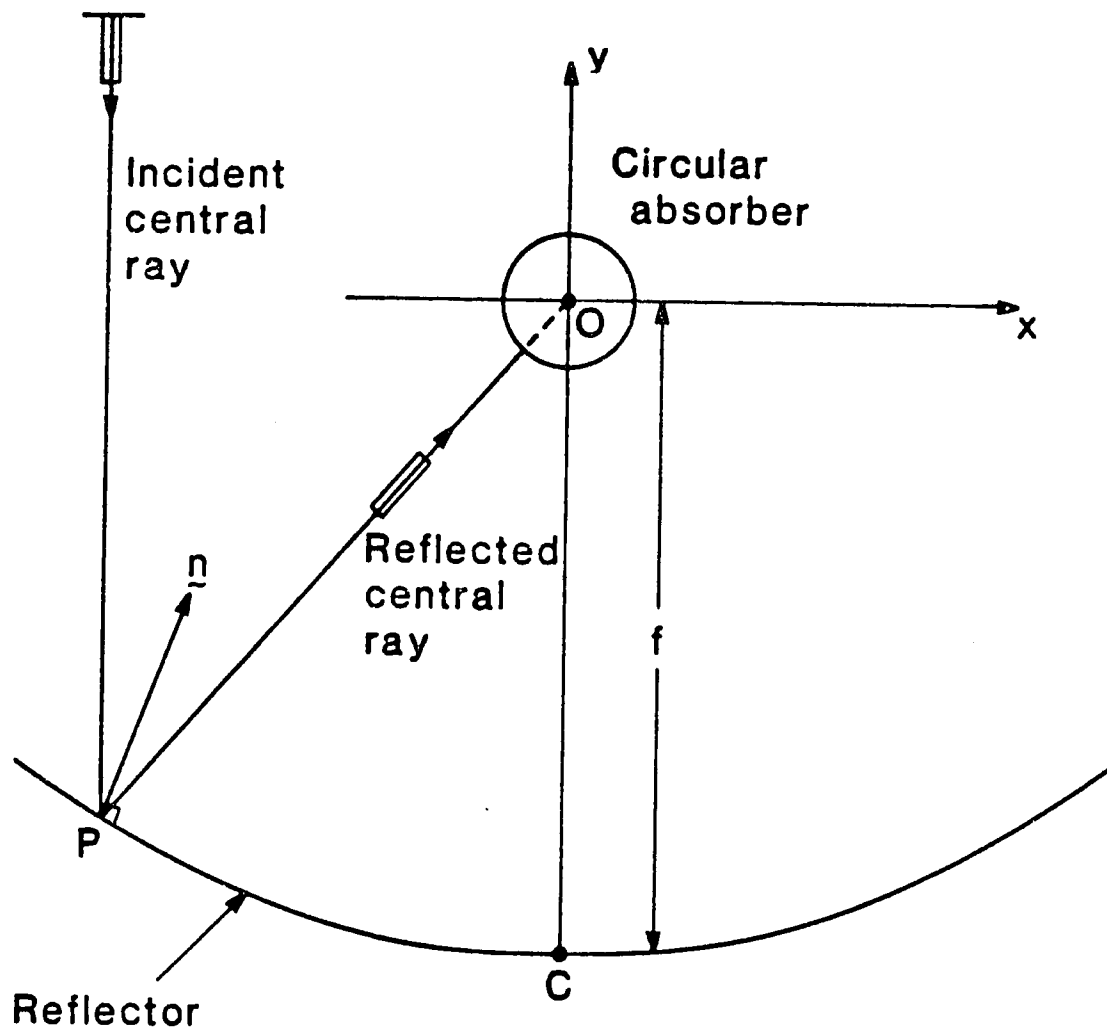


Figure 3.2 Idealized central ray optics of parabolic troughs.

delta functions, and it would be a simple matter to analytically calculate the flux-density pattern on the absorber tube and to determine the intercept factor.

In the real world, however, life is not so simple. The sun's rays do not arrive at the site as a collimated beam but as a somewhat dispersed beam. Moreover, even the central ray coming from the center of the solar disc may not reflect in the ideal manner but deviate from it because of slope errors on the trough near P or because of sun-tracking errors. The exact direction of the reflected ray is not known because a deterministic description of the direction of the surface normal at P is not available. Therefore, a statistical description is developed which will enable one to calculate the probability that the ray will reflect into a specified interval of directions which is adequate for calculating averages.

In the following, first, detailed descriptions of potential optical errors in the trough construction and operation are presented. Then, statistical characterization of the sunshape and errors are presented and discussed. Finally, numerical evaluation of the intercept factor using the statistical descriptions is presented.

3.4 Description of Optical Errors

Figure 3.3 presents a schematic representation of various types of potential errors that may be encountered

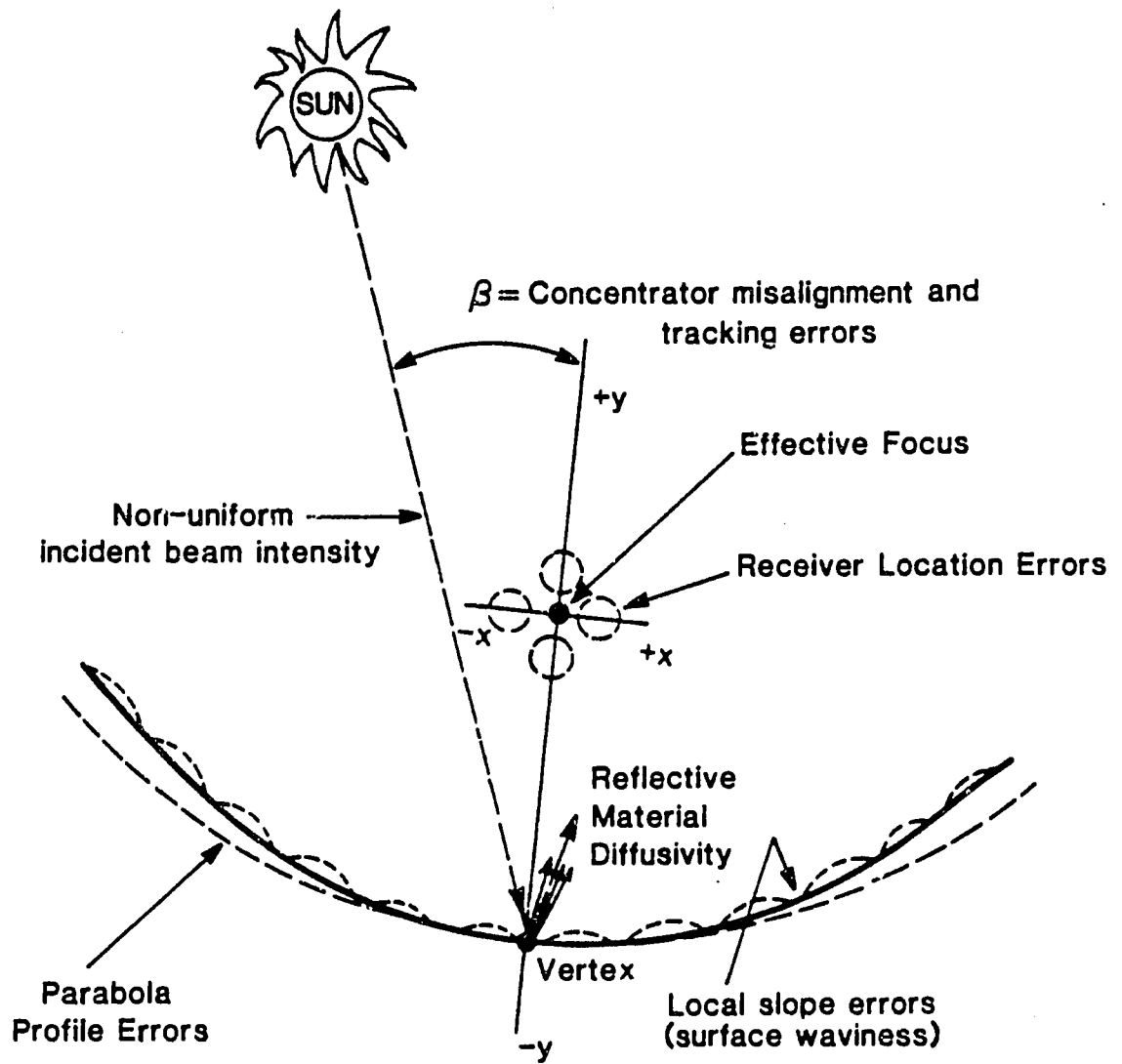


Figure 3.3 Description of potential optical errors in parabolic trough collectors.

in parabolic troughs. These can be listed as: errors associated with the reflecting surface, mislocation of the receiver with the effective focus of the reflecting surface, and misalignment of the collector aperture with respect to the sun (e.g., tracking errors).

First, the errors associated with the reflecting surface are considered. As a hypothetical example, the reflecting surface of the trough is assumed to be composed of a thin sheet of material, one surface of which is reflective. When this sheet is attached to its supporting structure (ribs), various distortions occur in the surface. The resulting surface has a wavy pattern and in general the mean surface obtained by averaging out the waves also may differ from the ideal (desired) surface. Finally, the reflecting surface may have a small-scale structure consisting of a grainy texture plus a striation pattern. All these factors will contribute to the blurring of the concentrated image at the receiver. However, they can be characterized as three basically independent modes of reflector error. As shown in Figure 3.4, the actual mean surface deviates from the ideal in such a way as to displace the effective focus. A local slope error primarily dependent on the deviation of the actual wavy surface from its mean contributes a deflection which approximates twice the angular deviation between the actual surface from the mean as is shown in Figure 3.5. Finally, small-scale structure consisting of a grainy texture can be characterized as a material property, namely, nonspecularity (diffusivity) of the reflective material. Figure 3.4

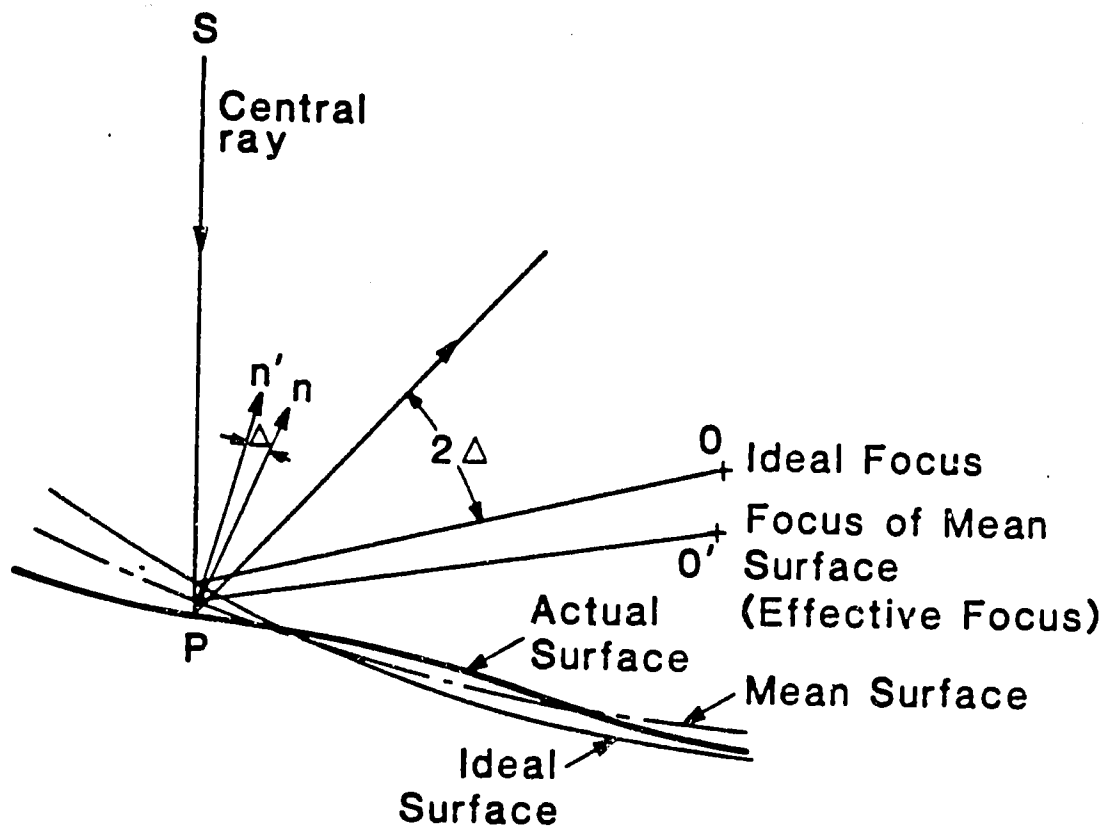


Figure 3.4 Schematic representation of a parabolic mirror surface showing the difference between slope errors and reflector profile errors.

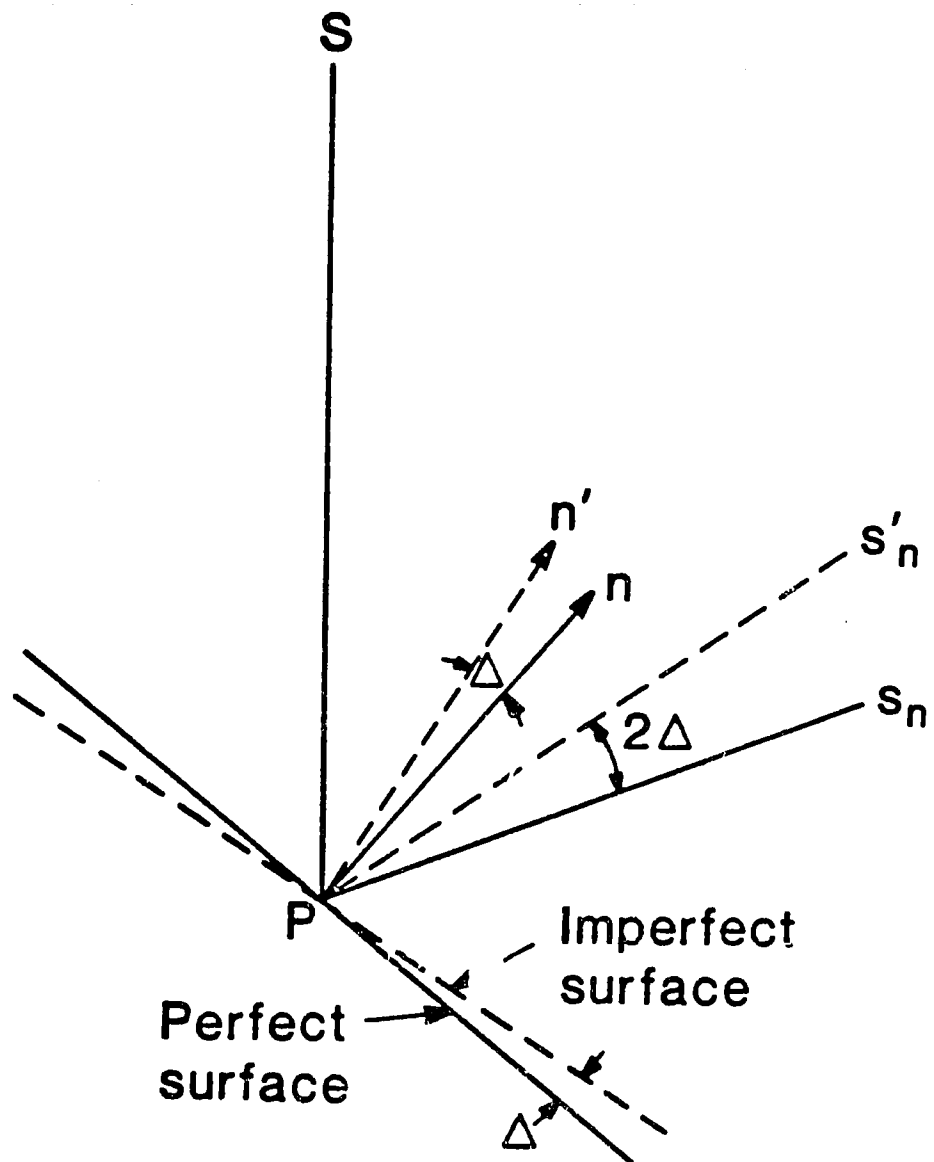


Figure 3.5 Ray traces of reflection from perfect and imperfect (random) mirror surfaces showing perfectly reflected central ray s_n and imperfectly reflected central ray s'_n .

illustrates the difference between slope errors and reflector profile errors, and Figure 3.6 illustrated the difference between slope errors and mirror diffusivity.

Two additional sources of error are those associated with the alignment and positioning of the receiver with respect to the expected focus and with the tracking accuracy of the collector drive system. As shown in Figure 3.3 at any given time the center of the absorber tube may be positioned at a distance away from the effective focus of the reflector due to:

- . errors in positioning the receiver tube during assembly;
- . change in the effective focus of the reflector during operation;
- . thermal growth and expansion of the receiver and its insulation during operation;
- . sagging of the receiver between supports which themselves are elastic and will be distorted by thermal gradients.

Furthermore, at a given time, the projected central ray from the sun may strike the reflector aperture plane at an angle (instead of striking the plane perpendicularly). This will be due to the rotation of the vertex-to-focus axis of the reflector during assembly or instantaneous misalignment of the reflector with the sun (tracking errors).

Table 3.1 presents a summary of the discussed imperfections/ errors according to their source of origin.

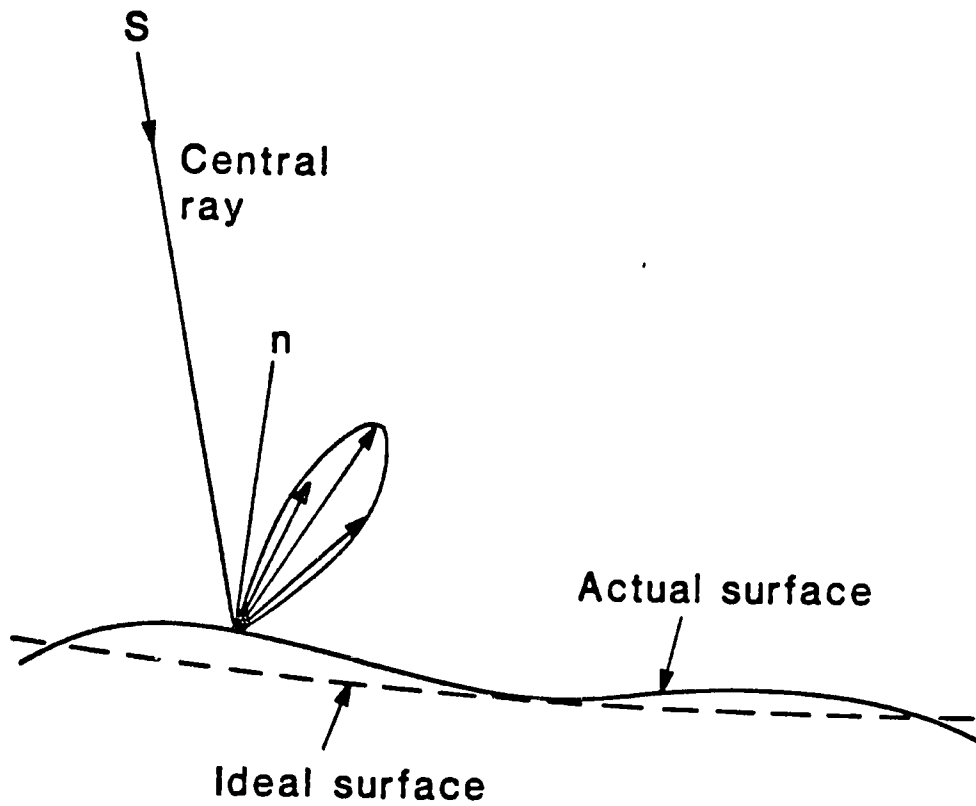


Figure 3.6 Schematic representation of a mirror surface showing the difference between slope errors and the mirror diffusivity.

TABLE 3.1 SUMMARY OF POTENTIAL ERRORS

MATERIALS
. Nonspecularity (diffusivity) of the reflective material
MANUFACTURE and ASSEMBLY
. Local slope errors (surface waviness) of the reflector that may result from distortion of its surface during manufacture,
. Profile errors: Average shape of the reflector (obtained by averaging the local slope errors or waves) may differ from a parabola. This may be due for example to distortions during manufacture and/or assembly. (It may also develop after collector has been in operation over a period of time.)
. Misalignment of the reflector during assembly. That is, reflector may be rotated (or twisted) about the vertex-to-focus axis during assembly (see Figure 3.3).
. Mislocation of the receiver tube. The receiver tube may be misaligned with respect to the effective focus of the reflector during manufacture and/or assembly (Figure 3.3)
OPERATION
. Tracker equipment may cause tracking bias/error due to its poor quality or tracking biases may develop after the collectors have been in operation for some time.
. Profile errors may develop or increase due to wind loading, temperature effects, etc., during operation.
. Nonspecularity (or diffusivity) of the reflective surface may increase with time, due to weathering or accumulated dust on reflector.
. Misalignment of the receiver with the effective focus may develop during operation due to one or a combination of the following:
(i) sagging or buckling of the receiver tube because of thermal expansion (if insufficient thermal expansion tolerance exists in the design);
(ii) permanent expansion of the receiver as a result of thermal cycling over a period of time;
(iii) change in location of the effective focus, due for example to increased profile errors in the reflector.

3.5 Analytical Techniques for Modeling Incident Sunshapes and Effective Sunshapes

3.5.1 Solar Irradiance Profile -- Incident Sunshape

In the early optical analyses of parabolic troughs (e.g., [6] and [9]) the sun's rays were assumed to be parallel, i.e., the sun was assumed to be an infinitely remote point-source. However, the sun is not a point-source and the solar disc has a finite size. In recognition of the finite size of the sun later studies [8 , 19] assumed a finite uniform intensity solar disc. But, this is not a realistic assumption either. A random photon from the sun is drawn from a distribution of directions and possesses different intensities depending upon where it originates on the sun. Therefore, a non-uniform distribution of intensity exists across the visible solar disc. This variation in intensity is directly observed and presumably arises from the interaction of complex mechanisms in the emitting solar atmosphere as well as atmospheric scattering in the terrestrial atmosphere. The directional distribution is widened by atmospheric scattering especially during hazy atmospheric conditions. Light clouds can cause considerable broadening of this distribution [20]. Scattering at a reflecting surface will cause a further modification of the sun's intensity distribution.

In the present work, an exponential function is used to describe the solar intensity. A probability density function describes the distribution of the sun's rays with respect to the direction of the central ray from the sun and is called the

"sunshape" [21, 22]. Therefore, the radiant intensity of the sun's rays for a total incident flux of I_b is described by a normal (Gaussian) distribution function as follows [21]:

$$I_{\text{sun}}(\zeta) = \frac{I_b}{2 \pi \sigma_{\text{sun}}^2} \exp\left[-\frac{\zeta^2}{2 \sigma_{\text{sun}}^2}\right] \quad (3.5)$$

where σ_{sun} is the scattering parameter (standard deviation of the scattered distribution) and ζ is the half optical cone angle (angular aperture). The optical cone angles (ζ) may be either one or two dimensional for parabolic trough or heliostat methods of energy collection respectively.

This representation of the sun's rays intensity distribution is particularly adaptable to treating the random scattering at material surfaces or effective scattering induced by manufacturing errors and tolerances. A set of sixteen "standard" sunshapes generated from measurements performed by Lawrence Berkeley Laboratory [23] are available in the literature. These sunshapes are intended to represent a wide range of shapes of interest to solar applications. The RMS width of these distributions ranges from a minimum value of 3.55 mrad to a maximum of 22.6 mrad.

Approximation of the intensity distribution of the sun across the solar disc by a normal probability distribution is found to be adequately accurate for optical analysis of troughs when optical errors are large compared to the width of the sun [16].

3.5.2 Reflected Beam Profile -- Effective Sunshape

The reflected beam profile can be characterized by using cone optics [24]. The reflection of radiation from a finite source, such as the sun, is illustrated in Figure 3.7.

The incident energy on a flat differential reflector of area dA is, as shown in Figure 3.7:

$$d^2e_i = Id\omega_i \cos\theta dA \quad (3.6)$$

where

I = Intensity distribution of the incident beam: assumed to be a normally scattered (Gaussian) function (Eq. (3.5)),

ω_i = solid angle containing incident radiation
($d\omega_i = \sin\zeta d\zeta d\gamma$).

In Eq. (3.5), the scattering parameter σ_{sun} which is the standard deviation of the scattered distribution, is usually small and on the order of 0.010 radian; therefore, small-angle approximations are valid.

The irradiance on the reflecting element is found by integrating over the complete solar disc, to be:

$$\begin{aligned} e_i &= 2 \int_0^{2\pi} \int_0^{\infty} d^2e_i(\zeta d\zeta d\gamma) \cos\theta dA \\ &= I_b \cos\theta dA \end{aligned}$$

The total specularly reflected radiation is assigned the symbol e_r and is composed of all the energy reflected to a surface normal to the specularly-reflected central ray. At the reflector, the magnitude of the intensity along an incident ray becomes negligible if the deviation, ζ , from the central ray is

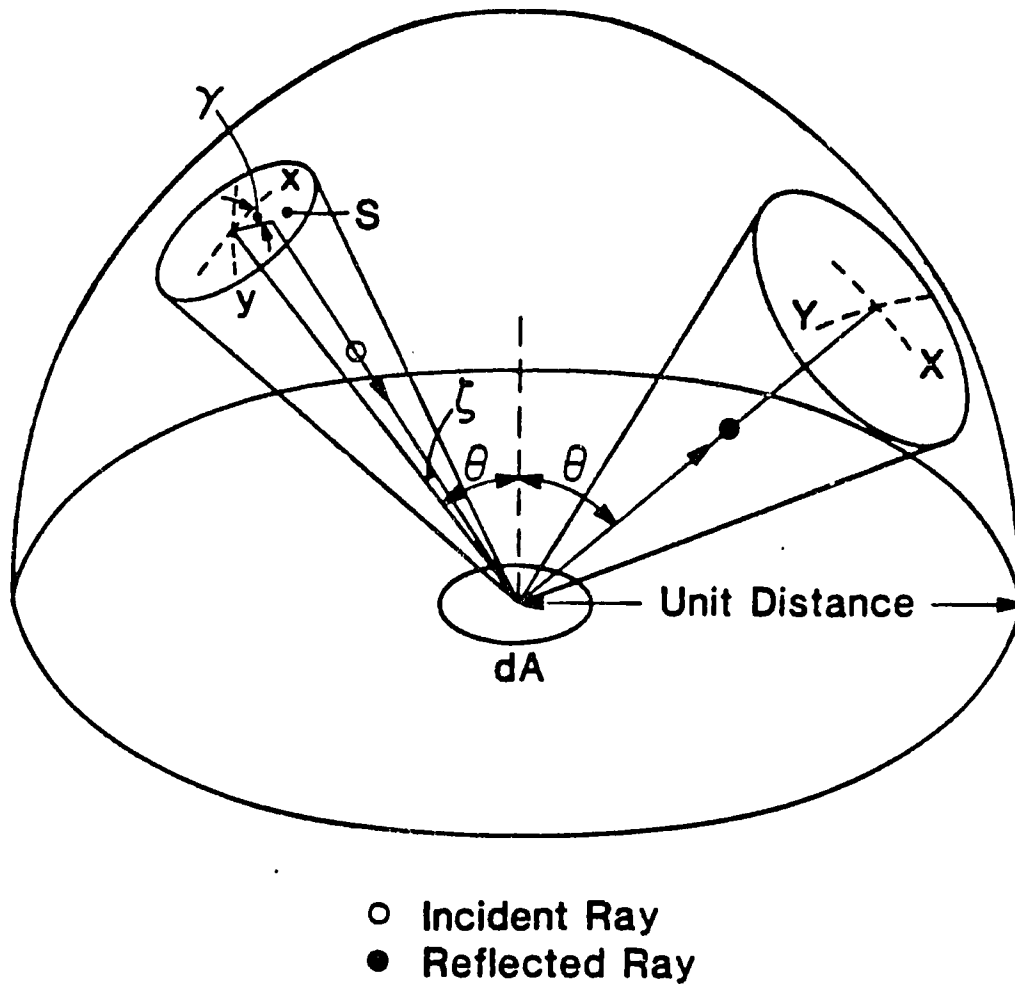


Figure 3.7 Abstract representation of scattering by reflection.

large with respect to σ_{sun} . A small multiple of σ_{sun} suffices (e.g., $2.5\sigma_{\text{sun}}$). It is also assumed that the surface is a good specular reflector; therefore, the magnitude of the intensity of a reflected ray will also vanish if the reflected ray from the direction of specular reflection for a given incident ray is large with respect to the scattering parameter σ_{mir} , descriptive of the material. An element of the reflected energy, d^4e_r , is assigned to be of higher order than the incident energy, d^2e_i , because the reflected energy arises from integration over the entire incident image. It is assumed that the reflection function is of the form $K \cdot \exp(-\zeta_r^2/2\sigma_{\text{mir}}^2)$ where ζ_r is the angular deviation from the specular direction for each incident ray, and K is yet undetermined constant. Cartesian coordinates may be assumed to exist on the unit radius hemisphere centered at dA since the angular deviation of a reflected ray from the specular direction of the ray from (x,y) is given by $(X-x, Y-y)$ such that $\zeta_r^2 = (X-x)^2 + (Y-y)^2$. The reflectance of the surface is given by the ratio of the energy in the incident ray to that in the reflected ray. Consequently, a rather general formulation of the reflectance function is given by

$$\rho(X-x, Y-y) = \frac{d^4e_r}{d^2e_i} \quad (3.7)$$

This yields an expression for the reflected energy as

$$d^4e_r = \rho(X-x, Y-y)I(x, y)(dx \, dy)(dA \cos\theta)dX \, dY \quad (3.8)$$

Which is in terms of the reflected intensity:

$$d^4e_r = I_r(X-x, Y-y)(dA \cos\theta)dX dY \quad (3.9)$$

The reflectance ρ is assumed to be of the form

$$\rho(X-x, Y-y) = K \cdot \exp(-((X-x)^2 + (Y-y)^2)/2\sigma_{mir}^2)$$

This is a reasonable assumption since one expects the reflectance to be even in the deviations $(X-x)$ and $(Y-y)$ and to vanish strongly with increased deviation. If the reflection is isotropic, as implied by the single parameter σ_{mir} , the total reflected energy is given by:

$$\begin{aligned} \frac{d^2e_r(X,Y)}{dX dY} &= \frac{K \cdot I_b}{2\pi\sigma_{sun}^2} \int_S \exp\left(\frac{-x^2}{2\sigma_{sun}^2}\right) \exp\left(\frac{-(X-x)^2}{2\sigma_{mir}^2}\right) dx \\ &\cdot \int_S \exp\left(\frac{-y^2}{2\sigma_{sun}^2}\right) \exp\left(-\frac{(Y-y)^2}{2\sigma_{mir}^2}\right) dy (dA \cos\theta) \quad (3.10) \end{aligned}$$

The preceding integrals are to be evaluated over the entire incident image, and since the incident intensity vanishes strongly for increasing values of X and Y , it is permissible to set the integration limits to be $(-\infty, \infty)$ without risk of error from the small angle assumptions. The right hand side of the reflected energy evaluation becomes the product of two convolutions, and the resulting expression is easily evaluated by the method of Fourier transforms as follows:

$$\frac{d^2e_r(X,Y)}{dX dY} = \frac{K \cdot I_b}{2\pi\sigma_{sun}^2} \int_{-\infty}^{\infty} \exp\left(\frac{-x^2}{2\sigma_{sun}^2}\right) \exp\left(\frac{-(X-x)^2}{2\sigma_{mir}^2}\right) dx$$

$$\begin{aligned}
& \cdot \int_{-\infty}^{\infty} \exp\left(\frac{-y^2}{2\sigma_{\text{sun}}^2}\right) \exp\left(-\frac{(Y-y)^2}{2\sigma_{\text{mir}}^2}\right) dy (dA \cos \theta) \\
& = \frac{K \cdot I_b}{2\pi\sigma_{\text{sun}}^2} \int_{-\infty}^{\infty} f_1(x) f_2(X-x) dx \int_{-\infty}^{\infty} g_1(y) g_2(Y-y) dy (dA \cos \theta) \\
& = \frac{K \cdot I_b}{2\pi\sigma_{\text{sun}}^2} (f_1(x) \otimes f_2(x)) (g_1(y) \otimes g_2(y))
\end{aligned}$$

Since the Fourier transform of a convolution is the product of the transforms of the two functions, the Fourier transform of the first product is readily expressed as

$$F(\alpha) = \mathcal{F}(f_1(x) \otimes f_2(x)) = \mathcal{F}(f_1(x)) \cdot \mathcal{F}(f_2(x))$$

$$F(\alpha) = \sigma_{\text{sun}} \sigma_{\text{mir}} \exp\left(-\frac{\alpha^2}{2}(\sigma_{\text{sun}}^2 + \sigma_{\text{mir}}^2)\right)$$

This standard form can be evaluated in the X domain as:

$$f(X) = \frac{\sigma_{\text{sun}} \sigma_{\text{mir}}}{\sigma_{\text{sun}}^2 + \sigma_{\text{mir}}^2} \exp\left(\frac{-x^2}{2(\sigma_{\text{sun}}^2 + \sigma_{\text{mir}}^2)}\right)$$

A similar procedure results in the same function for $g(X)$ which allows the final representation of the reflected energy as:

$$\frac{d^2 e_r}{dX dY}(X, Y) = \frac{K \cdot I_b}{2\pi\sigma_{\text{sun}}^2} (dA \cos \theta) \frac{(\sigma_{\text{sun}} \sigma_{\text{mir}})^2}{(\sigma_{\text{sun}}^2 + \sigma_{\text{mir}}^2)} \exp\left(-\frac{(x^2 + y^2)}{2(\sigma_{\text{sun}}^2 + \sigma_{\text{mir}}^2)}\right) \quad (3.11)$$

The total reflected energy is then

$$e_r = \int d^2e_r(X,Y)dX dY = K.I_b\sigma_{mir}^2$$

This allows the evaluation of K from the definition of the total spectral reflectance, R, which is assumed to be measured by a wide aperture device normal to the spectrally-reflected central ray

$$e_r = K.I_b\sigma_{mir}^2 = R.I_b$$

$$K = \frac{R}{\sigma_{mir}^2}$$

The reflectance function becomes

$$\rho(X-x, Y-y) = \frac{R}{\sigma_{mir}^2} \exp\left(-\frac{(X-x)^2}{2\sigma_{mir}^2}\right) \exp\left(-\frac{(Y-y)^2}{2\sigma_{mir}^2}\right) = \frac{R}{\sigma_{mir}^2} \exp\left(-\frac{\zeta^2}{2\sigma_{mir}^2}\right)$$

And the reflected image in terms of intensity can be expressed by regrouping the expression for $d^2e_r(X,Y)$ as follows

$$d^2e_r(X,Y) = \frac{R.I_b}{2\pi(\sigma_{sun}^2 + \sigma_{mir}^2)} \exp\left(-\frac{(X^2 + Y^2)}{2(\sigma_{sun}^2 + \sigma_{mir}^2)}\right) (dA \cos\theta) (dXdY) \dots(3.12)$$

The preceding expression is of the form

$$d^2e_r(X,Y) = I_{eff} d\omega_i dA$$

Consequently, the reflected image has the radiant intensity distribution

$$I_{eff}(X, Y) = \frac{R.I_b}{2\pi(\sigma_{sun}^2 + \sigma_{mir}^2)} \exp\left(-\frac{(X^2 + Y^2)}{2(\sigma_{sun}^2 + \sigma_{mir}^2)}\right) \quad (3.13a)$$

or

$$I_{\text{eff}}(\zeta) = \frac{R \cdot I_b}{2\pi\sigma_{\text{tot}}^2} \exp\left(-\frac{\zeta^2}{2\sigma_{\text{tot}}^2}\right) \quad (3.13b)$$

where

$$\sigma_{\text{tot}}^2 = \sigma_{\text{sun}}^2 + \sigma_{\text{mir}}^2$$

$$\zeta^2 = X^2 + Y^2$$

The preceding results demonstrate that the reflected intensity has the same functional form as the incident intensity when a normally-scattered source and normally-scattering reflectance is assumed. Reference [25] presents empirical results which demonstrate that normal scattering is descriptive of most actual surfaces encountered in solar energy utilization.

The preceding derivation is based on a two-dimensional sunshape description because solar intensity distribution data is usually reported as a radial distribution $I_{\text{radial}}(\zeta)$ in $\text{W/m}^2\text{sr}$, ζ being measured from the center of the solar disc. For line focus systems like a trough it is convenient to transform the radial distribution to a linear one since a one-dimensional description is required. The appropriate description is formed by simply assuming that lateral slices are taken across the two-dimensional sunshape such that

$$I_{\text{linear}}(\zeta_{\perp}) = \int_{-\infty}^{\infty} I_{\text{radial}}((\zeta_{\parallel}^2 + \zeta_{\perp}^2)^{\frac{1}{2}}) d\zeta_{\parallel} \quad (3.14)$$

where ζ_{\perp} is the angular coordinate in the plane normal to the focal line and ζ_{\parallel} the angular coordinate parallel to the

focal line (similar to the coordinates θ_{\perp} and θ_{\parallel} shown in Figure 3.1). Integration of Eq.(3.14), using Eq.(3.5), results in an expression for the one-dimensional solar intensity distribution:

$$I_{\text{sun,linear}}(\zeta) = \frac{I_b}{\sigma_{\text{sun,linear}}(2\pi)^{\frac{1}{2}}} \exp\left(-\frac{\zeta^2}{2\sigma_{\text{sun,linear}}^2}\right)$$

Since the sunshape has a circular geometry, the one-dimensional rms width ($\sigma_{\text{sun,linear}}$) is related to $\sigma_{\text{sun}}(\text{radial})$ by:

$$\sigma_{\text{linear}} = \frac{\sigma_{\text{radial}}}{\sqrt{2}} \quad (3.15)$$

In this sense, the sun appears to be narrower for a line focus collector than for a point focus collector where a two-dimensional sunshape description is required.

Similarly, the reflected beam profile given by Eq.(3.13b) is modified as follows

$$I_{\text{eff}}(\zeta) = \frac{I_b R}{\sigma_{\text{tot}}(2\pi)^{\frac{1}{2}}} \exp\left(-\frac{\zeta^2}{2\sigma_{\text{tot}}^2}\right) \quad (3.16)$$

where

$$\sigma_{\text{tot}}^2 = \sigma_{\text{sun,linear}}^2 + \sigma_{\text{mir,linear}}^2$$

3.5.3 Analysis of Optical Errors

In this section models are presented for characterizing and assessing the effect of optical errors described in section

First, a statistical approach for modeling the effect of the errors is described. Then the shortcomings and errors associated with this approach are discussed and a comprehensive approach for modeling the effect of errors (on the optical performance of the trough) is presented.

Once again, the independent optical errors are:

- . mirror diffusivity,
- . local slope errors,
- . parabola profile errors,
- . receiver location errors,
- . reflector alignment and tracking errors.

Statistical Error Analysis

In the statistical error analysis, all five errors are assumed to be statistically independent stochastic processes and their occurrences, when averaged over time and over the entire collector or array of collectors, are assumed to be approximately normal (Gaussian) distributions with zero mean [16, 22]. Then, the resulting scattered intensity distribution of the energy directed to the absorber tube (from the reflector), that is, the effective sunshape, is obtained from the convolution of the sunshape successively with the normal scattering functions describing the independent modes of scattering. As shown in the preceding section, a normal distribution function remains a normal distribution function when convoluted with other normal distribution functions.

Therefore, the effective sunshape is a normal distribution with an overall scattering parameter, σ_{tot} , equal to the square root of the sum of the squares of the individual scattering parameters. For example, Bendt [16] presents σ_{tot} as follows:

$$\sigma_{\text{tot}} = \sqrt{\sigma_{\text{sun}}^2 + \sigma_{\text{mir}}^2 + (2\sigma_{\text{slope}})^2 + \sigma_{\text{track}}^2 + \sigma_{\text{displacement}}^2} \quad (3.17)$$

where, terms under the radical represent the standard deviations of: the sun's energy distribution, the mirror nonspecularity error distribution, the slope error distribution (averaged over an entire collector surface), the tracking error distribution (time-averaged over several oscillations of tracking error for an entire field of collectors) and the receiver location error distribution (averaged over an entire field collectors and time). Twice the standard deviation of the slope error is employed because, as shown in Figure 3.5, reflector optics result in doubling of the slope error as the deviation from the mean specular direction.

In summary, a normal (Gaussian) distribution approximation for the optical errors permits the convolution calculations to reduce to a simple addition of the standard deviations and allows for the characterization of the errors with a single error parameter.

Obviously, the described statistical approach has a lot of merit; it provides a 'common-denominator' for the combination

of various errors into a single parameter (σ_{tot}), and thus simplifies the analysis and calculations tremendously by reducing the number of independent variables. However, the normal distribution assumption for errors, which is the backbone of this approach, is not valid for all errors for all practical applications. For example, reflector alignment and tracking errors can be assumed to be random (and, consequently, have normal distributions) only when they are averaged over an entire field of collectors and over a long time. Similarly, the receiver location errors are subject to the same restraint. Therefore, representation of these errors by normal distributions with zero mean is not valid when small scale applications, for example, small installations for home heating, are analyzed. Furthermore, even if all of the errors are forced or assumed to have normal distributions, the resulting single error parameter, σ_{tot} , obscures most of the information a designer will need during the preliminary design phase. Therefore, it is necessary to handle some of the errors differently and have more than one error parameter to characterize and quantify the geometric effects resulting from error distributions that do not have zero mean (This will also help incorporate the effects of 'gross' optical errors).

In a recent study, Treadwell [26] addresses a similar issue and attempts to quantify the effect of tracking and receiver location errors separately, i.e., separate from

the effect of the rest of the errors that are lumped into σ_{tot} . However, he fails to introduce new 'universal' error parameters, and as a result, ends up presenting results for a limited number of cases. (Three concentration ratios and two reflected energy distribution standard deviations are considered for a 90°-rim angle reflector.) Moreover, in his study, the analysis of errors are embedded in a complex collector model which takes into account geographic effects as well, thereby making the results site - dependent. Therefore, the presented results are highly restricted and lack the degree of flexibility a designer will need when designing troughs for different environments and sites.

Comprehensive Error Analysis

In the present study, a more general and comprehensive approach is taken. First, errors are divided into two groups: random and non-random (systematic). Then, universal error parameters are obtained for the characterization and analysis of the different types of errors.

Random and non-random (systematic) error groups are explained as follows:

Random Errors

Random errors are defined as those errors which are truly random in nature and, therefore, can be represented by normal (probability) distributions with zero mean. They are treated statistically and give rise to spreading

(widening) of the reflected energy distribution (see Figure 3.8). These errors are identified as follows:

- (i) Scattering effects that are associated with the optical material used in the reflector. Reference [25] presents empirical results which demonstrate that normal scattering is descriptive of most actual surfaces encountered in solar energy utilization. Reference [27] lists values of specular reflectance, ρ , and scattering parameter σ_{mir} for glass, plastic and metals.
- (ii) Scattering effects caused by random slope errors (e.g., waviness of the reflector surface due to distortions that may occur during manufacture and/or assembly). Slope errors of this kind can be characterized by normal scattering [28]. Pettit et. al. [17] have recently shown that scattering that results from slope errors can be measured using laser ray-trace techniques and the value of the scattering parameter, σ_{slope} , can be related to the fabrication method used (see Table 3.2) in the construction of the reflector. Bendt et.al.[29] present methods for determining σ_{slope} without laser ray tracing.
- (iii) Misalignment of the collector (with the sun) due to purely random tracking errors (which last only

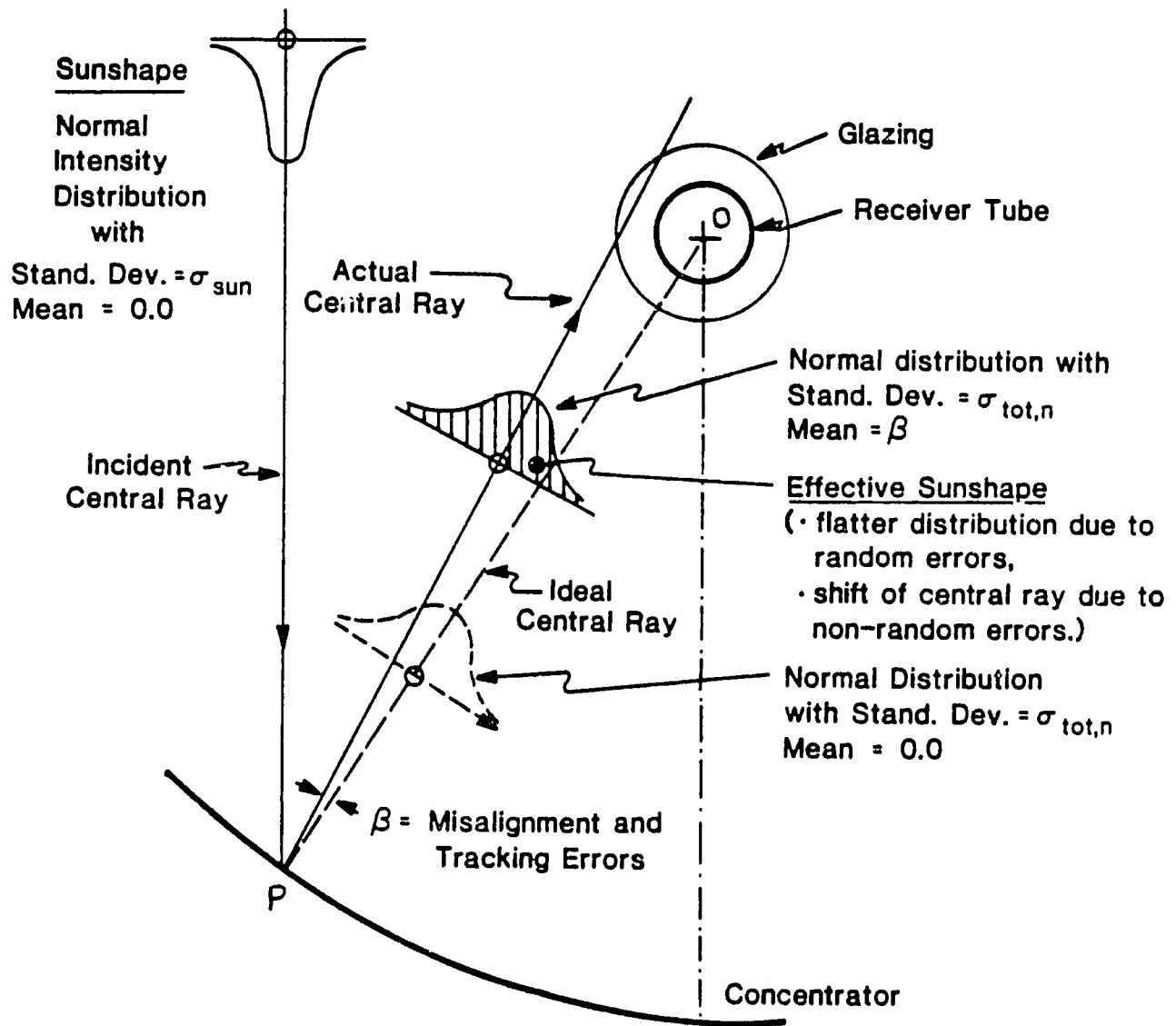


Figure 3.8 Modeling of potential optical errors in parabolic trough collectors.

TABLE 3.2¹ Typical Focal Lengths and Slope Errors for Model
Parabolas of Various Materials and Processes

				As Manufactured		After 13 Months of Temperature and Humidity Cycling	
Types of Structure	Materials	Fabrication Method	Cost Estimates ² (\$/ft ²)	Focal ^a Length (cm)	RMS Slope Error, σ (mrad)	Focal Length (cm)	RMS Slope Error, σ (mrad)
Laminates	Plywood 19 mm thick-7 ply	High Pressure Laminating Press	1.4	73.1	7.9	80.0	7.3
Sandwiches	Fiberglass Skin Corrugated Fiberglass Core, 51 mm thick	Low Pressure Press	2.1	77.9	2.5	78.5	2.5
	Paper Skin and Corrugated Paper Core, 51 mm thick	Low Pressure Press	1.9	74.3	2.4	72.2	4.9
	Aluminum Skin and 9.5 mm Cell, Aluminum Honeycomb Core, 38 mm thick	Autoclave	2.5	77.2	1.8	77.6	4.7
	Bent glass over Foam Glass	Vacuum Forming	3.0	76.5	1.5	In Testing	
Molded Structures	Sheet Molding Compound Molded with Integral Ribs, 19 mm deep	Closed Die Forming in Hot Mold	1.8	74.0	2.4	In Testing	
^a Note the nominal focal length was 76.2 cm.							

¹ From Reference [17].

² 1976 Dollars.

a very short period of time) can also be assumed to have normal distributions.

Non-random (Systematic) Errors

Errors which are assumed to have a single deterministic value, instead of a distribution of values, are called 'non-random'. They are characterized, in general, as those errors which can be related directly to anticipated errors in manufacture/assembly and/or in operation. In general these errors will cause the central ray of the reflected energy distribution (effective sunshape) to shift from the design direction PO (see Figure 3.8). The non-random errors are identified as follows:

- (i) Reflector profile errors, due for example to deflection (flattening) or severe waviness of the reflector surface. They will cause a permanent change in the location of the focus of the reflector. Hence the reflected rays may miss the receiver, if the receiver is located at the design focus of the parabola (reflector).
- (ii) Consistent misalignment of the trough with the sun, due for example to a constant tracking error or rotation of the trough's vertex-to-focus axis during assembly. This will shift the location of the focus to the left or to the right of the ideal focus and may cause the central ray of the reflected

beam to miss the receiver.

- (iii) Misalignment of the receiver with the effective focus of the trough (due to reasons discussed in section 3.3.1). This kind of error will also be systematic and it will cause the central ray(s) to miss the receiver.

In the present study, random errors are modeled statistically, by a total reflected energy distribution standard deviation at normal incidence, $\sigma_{\text{tot},n}$ and the effective sunshape is expressed as:

$$I_{\text{eff}}(\zeta) = \frac{\rho I_b}{\sigma_{\text{tot},n} (2\pi)^{\frac{1}{2}}} \exp\left(-\frac{1}{2}\left(\frac{\zeta - \mu}{\sigma_{\text{tot},n}}\right)^2\right) \quad (3.18)$$

where,

ζ = Angular aperture (radians),

ρ = Average specular reflectance of the reflective surface,

I_b = Beam solar radiation, W/m^2

μ = Angular shift of the mean of the distribution (radians).

The scattering parameter for random errors is given by:

$$\sigma_{\text{tot},n} = \sqrt{\sigma_{\text{sun},n}^2 + \sigma_{\text{mirror},n}^2 + 4\sigma_{\text{slope},n}^2 + \dots} \quad (3.19)$$

where,

$\sigma_{\text{sun},n}$ = Energy distribution standard deviation of the sun's rays at normal incidence and solar noon.

- $\sigma_{\text{slope},n}$ = standard deviation of the distribution of local slope errors at normal-incidence,
- $\sigma_{\text{mirror},n}$ = diffusivity of the reflective material at normal-incidence.

The non-random errors are analyzed as geometric effects, i.e., provisions are built into the optical model which allow for the analysis of such errors. Each one of these errors will be characterized by a single deterministic value. The following physical measures will be used in quantifying the non-random errors:

- . Reflector profile errors : Distance between the effective and ideal focus of the reflector measured along the optical axis of the reflector,
- . Receiver location errors : Distance between the ideal focus of the reflector and center of the absorber tube,
- . Misalignment errors : Angle between the central ray from the sun and the normal to reflector's aperture plane (β in Fig.3.3).

Because reflector profile errors and receiver location errors along the optical axis (in $\pm y$ direction) essentially bring about the same effect (see Figure 3.9), they can be accounted for together, in a single parameter. Hence, there are only two independent non-random variables and these are β and d_r . (Note that d_r is the distance between the effective focal point of the trough and the center of the

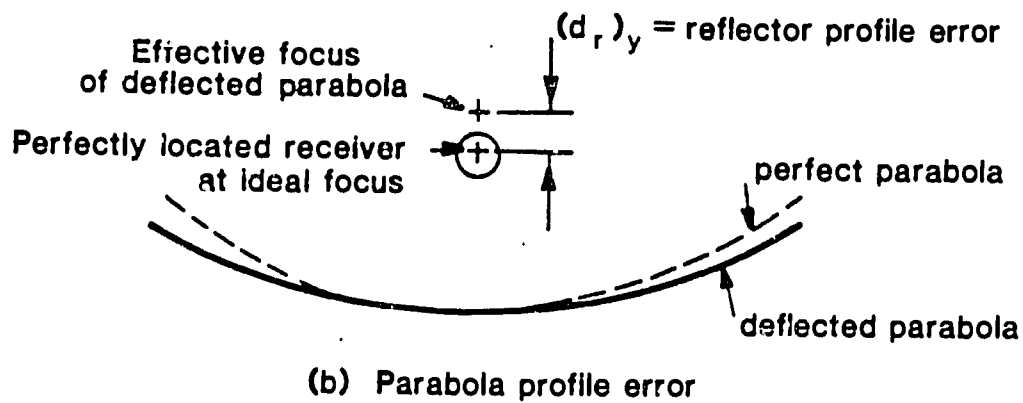
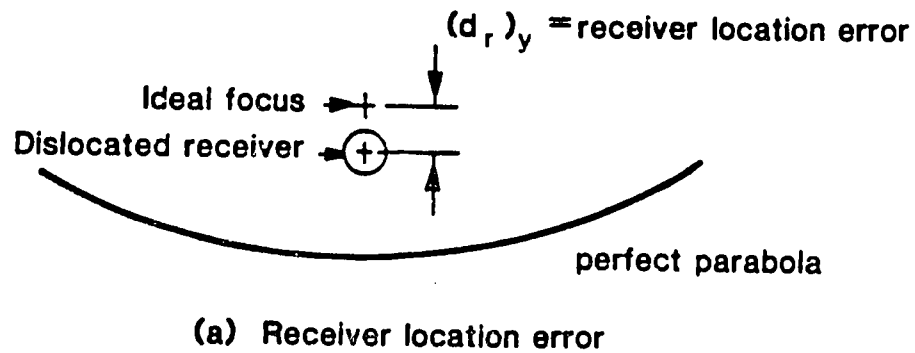


Figure 3.9 Combination of receiver location and parabola profile errors.

absorber tube.) The non-random errors are modeled as geometric effects and they are accounted for by a finite angular shift in the mean (μ in Eq.(3.18)) of the reflected energy distribution.

In summary, instead of one now there are three error parameters, one random ($\sigma_{\text{tot},n}$) and two non-random (β and d_r), to characterize various optical errors. This will, of course, complicate the optical analysis. However, as it will be seen in the following chapters, having three error parameters will substantially enhance the effectiveness and reliability of design calculations. Moreover, the three error parameters will allow for a comparison of the effects of different errors and help to determine and minimize the 'crucial' errors (errors which degrade the performance the most). Also, this will allow for a trade-off study between errors.

3.6 Effect of Off-Axis Operation

The collector is said to be in off-axis operation when the direction of the incident central ray is not perpendicular to the aperture plane of the trough. Off-axis operation affects the performance of the trough in two ways:

- (i) The elevation of the sun from the x-y plane (see Figure 3.1) has an effect on the width of the image on the receiver (abberation effects),
- (ii) In troughs of finite length there will be loss of radiation from the ends of the reflectors (end effects).

Nevertheless, the end effects can be minimized by using end reflectors, long troughs or polar mounts [30]. The end effects are not taken into account in the present collector design studies. It is assumed that this effect will be accounted for when the decision on the length of the ΔT -string is made after the application type and the tracking mode are known.

Rabl et.al. [16] have shown that the width of the solar image on the receiver will vary as $1/\cos\theta_{||}$. Therefore, for off-axis operation, the scattering parameter σ_{sun} in Eq.(3.17) will need to be changed to:

$$\sigma_{\text{sun}} = \frac{\sigma_{\text{sun},n}}{\cos\theta_{||}} \quad (3.20)$$

However, in the present work, design studies are based on instantaneous on-axis operation only, therefore, variations in the width of the solar image are not taken into account explicitly. Instead, all the off-axis effects including the variations in the width of the solar image are assumed to be lumped into an incidence angle modifier, $K(\theta)$, which is to be experimentally measured as recommended by the researchers at NASA-Lewis and Sandia Laboratories [31]. Rabl et.al.[18] have presented empirical equations for experimentally measured incidence angle modifiers for several parabolic trough collectors manufactured by various U.S. companies like Acurex, Solar Kinetics, Hexel (Sandia), Hexel (SERI) and Del.

3.7 Summary

In this chapter a thorough study of the optics of the PTC's was presented. Potential optical errors in manufacture, assembly and operation of troughs were identified. Models were developed for modeling and analysis of the errors. It was shown that the fraction of the solar rays intercepted by the collector absorber tube, intercept factor, is a function of collector geometry parameters C , ϕ and D as well as the random (σ) and the non-random (β , d_r) error parameters. The effect of off-axis operation of the collector on performance was also discussed. In the following chapter, preliminary results of the comprehensive optical analysis are presented. Also, the derivation of universal error parameters which combine collector geometry parameters with error parameters is given.

Chapter Four
PRELIMINARY OPTICAL RESULTS AND
DERIVATION OF UNIVERSAL ERROR PARAMETERS

The value of the intercept factor is governed by random and non-random errors as well as the concentrator geometry (concentration ratio C and rim angle ϕ). So, the intercept factor at normal-incidence, γ , can be written as:

$$\gamma = \text{fn}(\phi, C, D, \sigma = \sigma_{\text{tot},n}, \beta, d_r) \quad (4.1)$$

where D is the absorber tube diameter. A modified version of the EDEP code [32] developed at Sandia is utilized for analyzing the effect of errors on the intercept factor. This code uses a ray-trace technique to project the effective sunshape, given by Eq. (3.16), onto a circular absorber tube and then to output, the amount of energy intercepted by the absorber tube.

The EDEP code was used extensively in design and analysis of Sandia's prototype troughs [13, 14, 15, 26]. It has been validated and shown to be a sufficiently detailed optical simulation model. Therefore, instead of starting from scratch, the decision has been made to utilize EDEP's basic numerical structure as the starting point in the present study. As indicated earlier, the original code handled all the optical errors as random assuming normal distributions (with zero mean) for their occurrences. The code has been modified to handle random and non-random errors. Provisions were built into the code to handle deterministic angular pointing errors (β) and receiver mislocation errors (d_r); these were modeled as geometric effects. Also, the code has been restructured in

order to facilitate its use and applicability to comprehensive design studies and determination of error-tolerances. The new code is named EDEP2. Its input includes geometry parameters (ϕ , C and D) and error parameters (σ , β and d_r) and it outputs the geometric intercept factor. No transmission-absorption losses are included in the geometric intercept factor (Eq. (4.1)). These are accounted for by a separate multiplicative factor, $\rho\tau\alpha$, as shown in Eq.(3.1).

Many computer simulations were made using different sets of values for the parameters ϕ , C, σ , β and d_r . Results of these runs are summarized in Figures 4.1 through 4.18.

In Figures 4.1 through 4.8, effect of changing random and non-random error parameters (σ , β , d_r) for a fixed collector geometry (C=20, D=2.54cm and $\phi=90^\circ$) is studied. First, the simultaneous effect of receiver mislocation in the lateral direction, $(d_r)_x$, and tracking errors are studied for different values of random error levels (Figures 4.1, 4.2 and 4.3). A lower limit of 0.0025 radians, which is the standard deviation of the energy distribution of the sun's rays at solar noon on a clear day, is chosen for the random error parameter, σ . As expected, curves in Figures 4.1 to 4.3 are unsymmetric; receiver mislocation in the lateral direction produces a non-uniform effect when combined with simultaneous tracking errors. This is expected because tracking errors move the focus of the the reflector along the lateral axis and the effect of this shift is either compensated or magnified by the lateral receiver mislocation: for a positive β , receiver mislocation

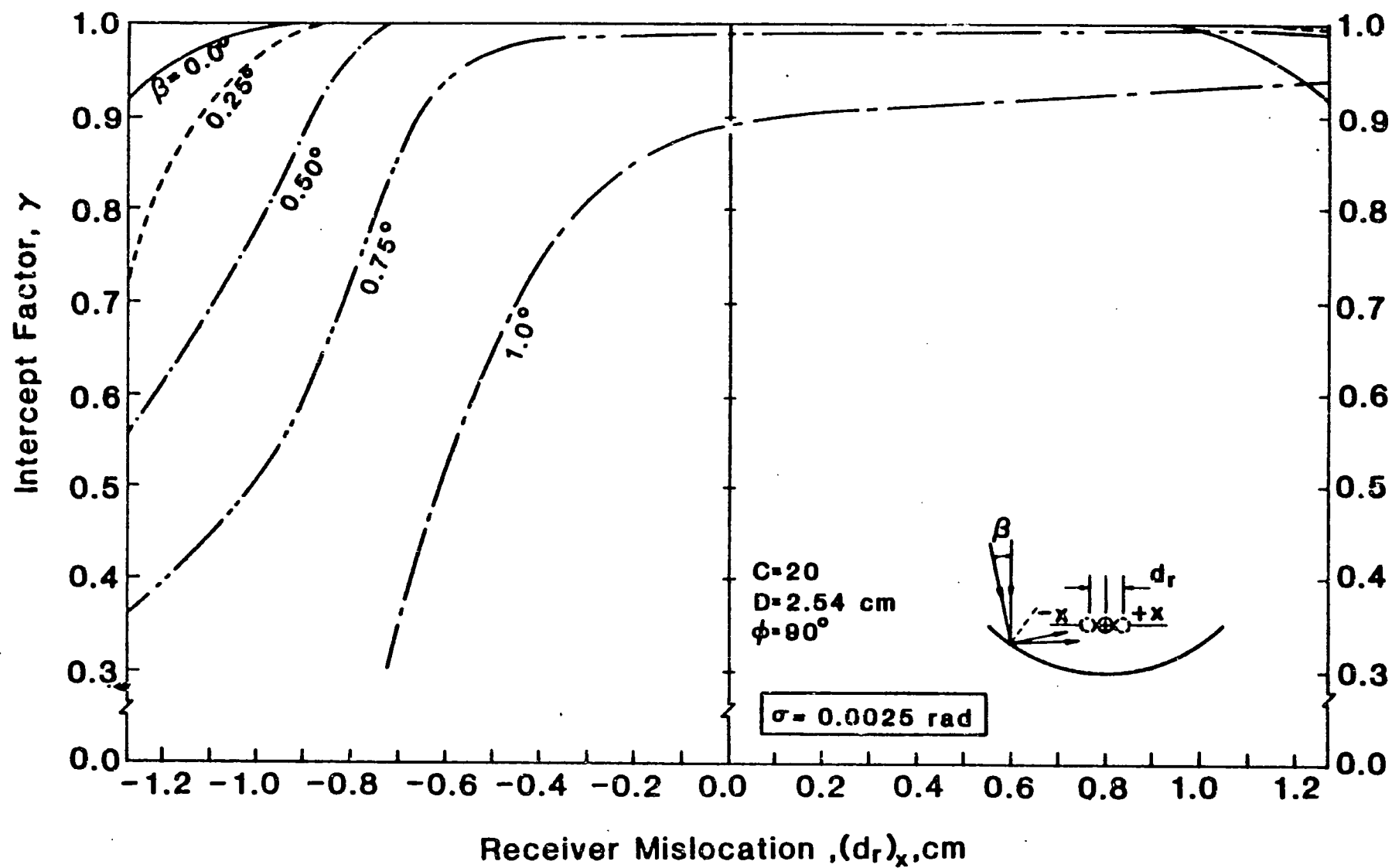


Figure 4.1 Intercept factor as a function of receiver mislocation along the lateral axis and tracking error for $\sigma = 0.0025$ radian.

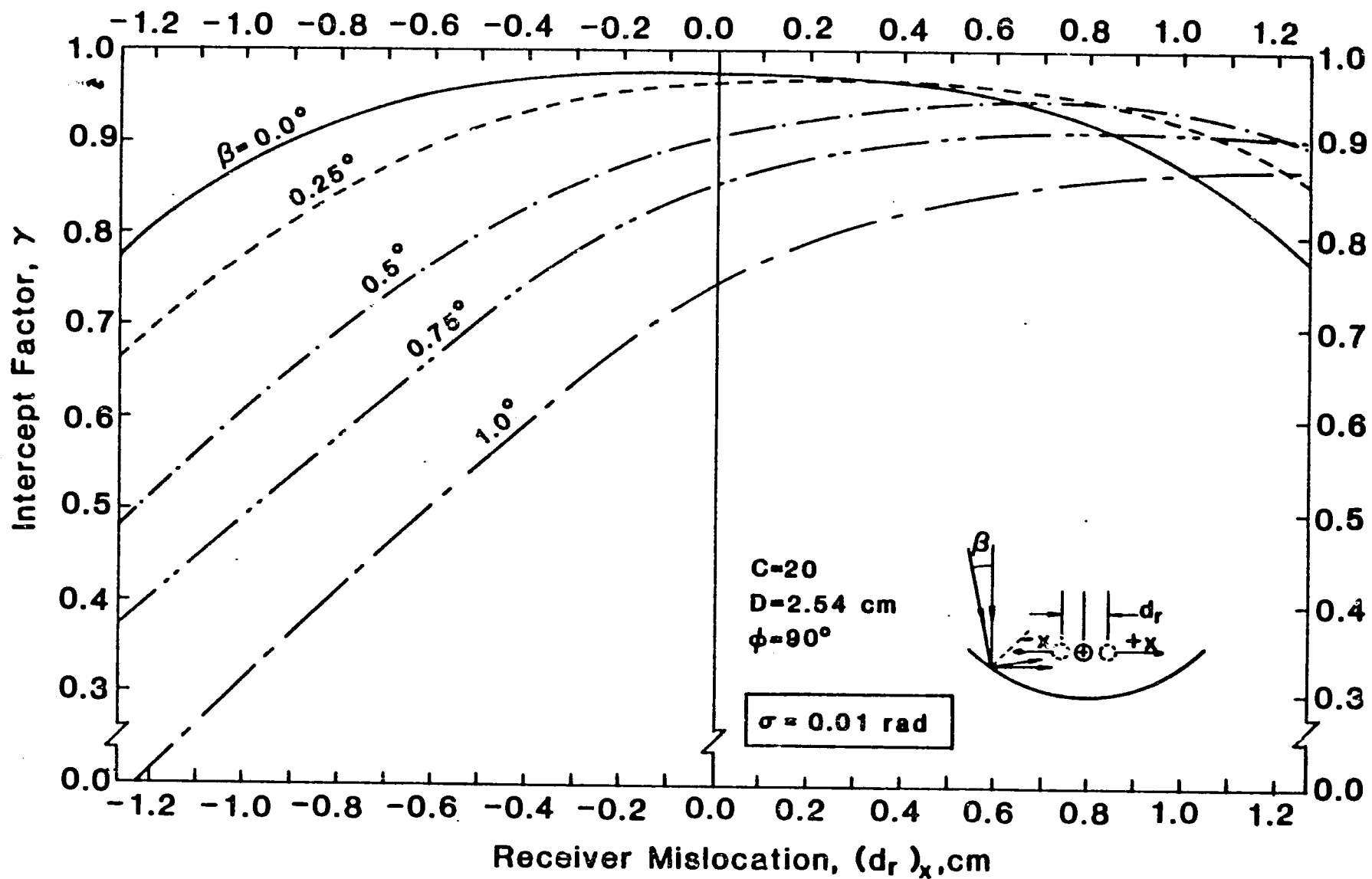


Figure 4.2 Intercept factor as a function of receiver mislocation along the lateral axis and tracking error for $\sigma = 0.01$ radian.

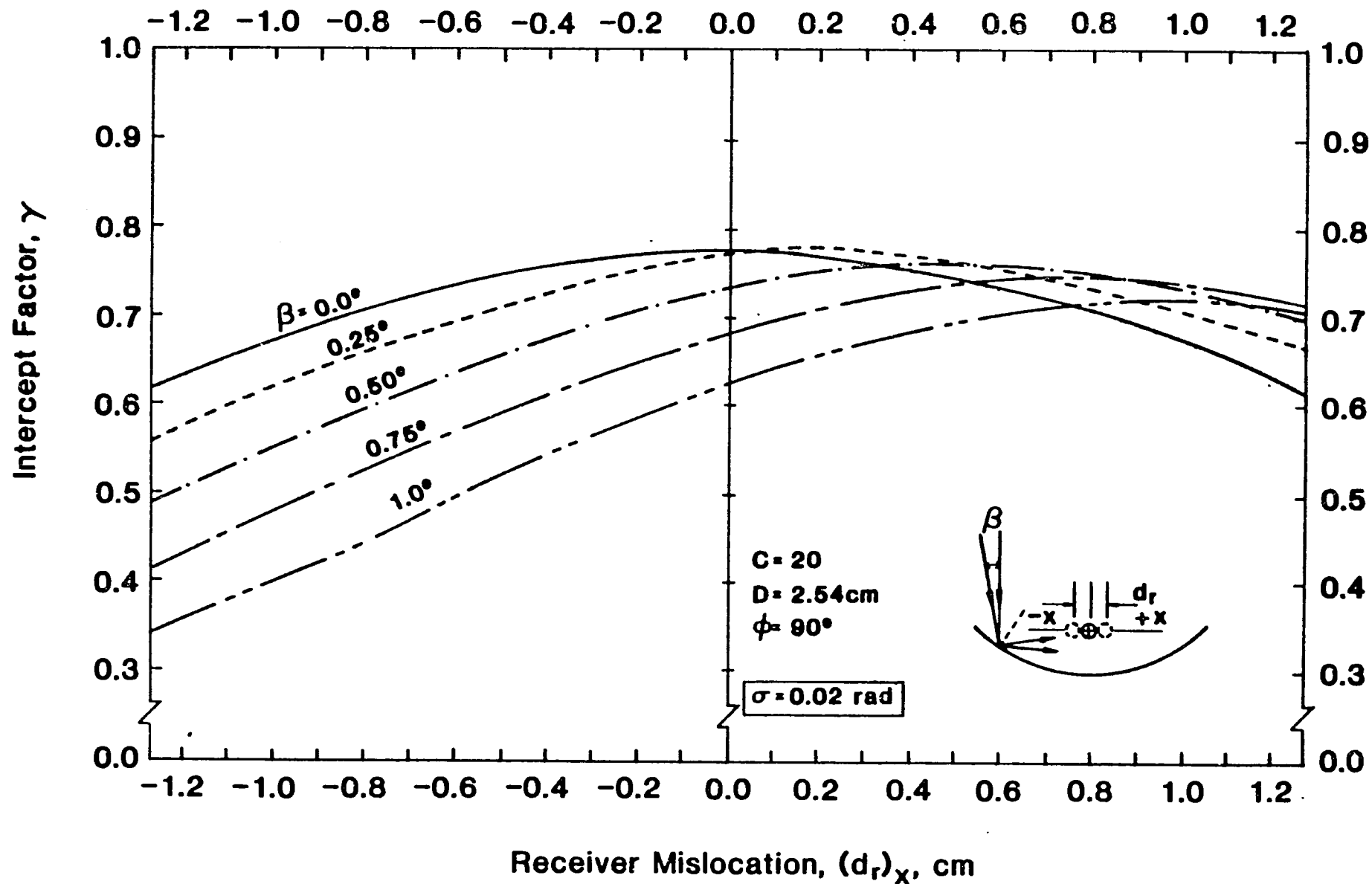


Figure 4.3 Intercept factor as a function of receiver mislocation along the lateral axis and tracking error for $\sigma = 0.02$ radian.

mislocation in +x direction compensates for the tracking error while mislocation in -x direction compounds the effect of the tracking errors. Next, the simultaneous effect of receiver mislocation along the optical axis (vertex-to-focus axis) and tracking errors are studied for different random error levels (see Figures 4.4 through 4.6). As shown in the figures, receiver mislocations in +y direction bring about the same effect as the mislocations in -y direction, therefore, curves in the figures are symmetric. Again, as expected, for higher random error levels the curves are flatter. Obviously, this is due to flattening of the intensity distribution of the effective sunshape.

For the design studies, it will be appropriate to consider receiver location errors along one axis alone; this will eliminate the complications that may arise due, for example, to odd coupling of the errors. In this study, receiver mislocations along the optical axis, i.e., $\pm(d_r)_y$, are chosen to represent the receiver location errors. This choice is supported by the following arguments:

- . In most real-life applications occurrence of receiver location errors in the y-direction have the highest expectancy because the sagging of the receiver due to its own weight and/or due to thermal expansions will result in mislocation in this direction.
- . Reflector profile errors shift the effective focus along the optical axis and therefore, for a receiver located at a distance d_r away from the effective focus, the axial component of d_r , $(d_r)_y$, which

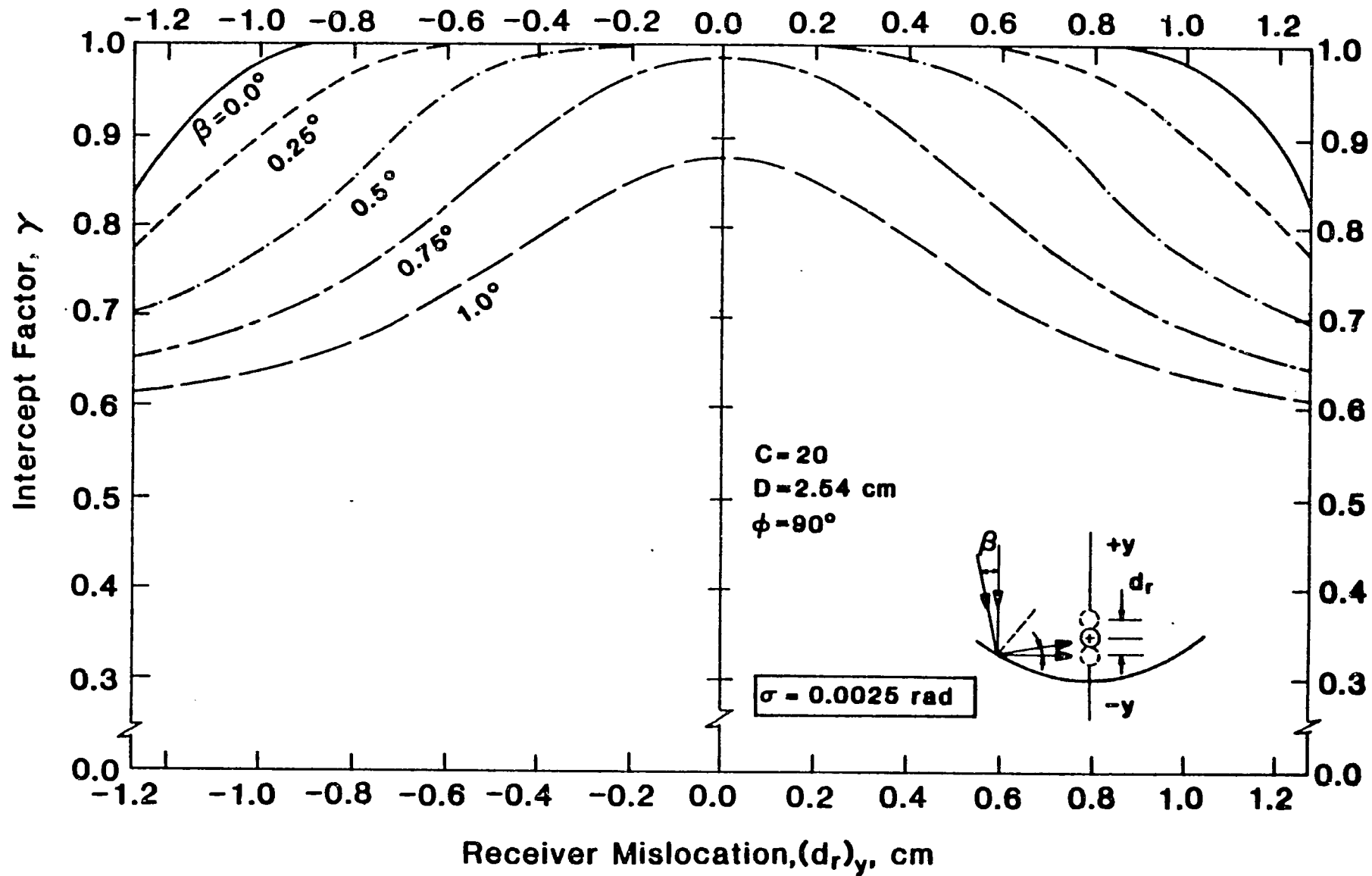


Figure 4.4 Intercept factor as a function of receiver mislocation along the optical axis and tracking error for $\sigma = 0.0025$ radian.

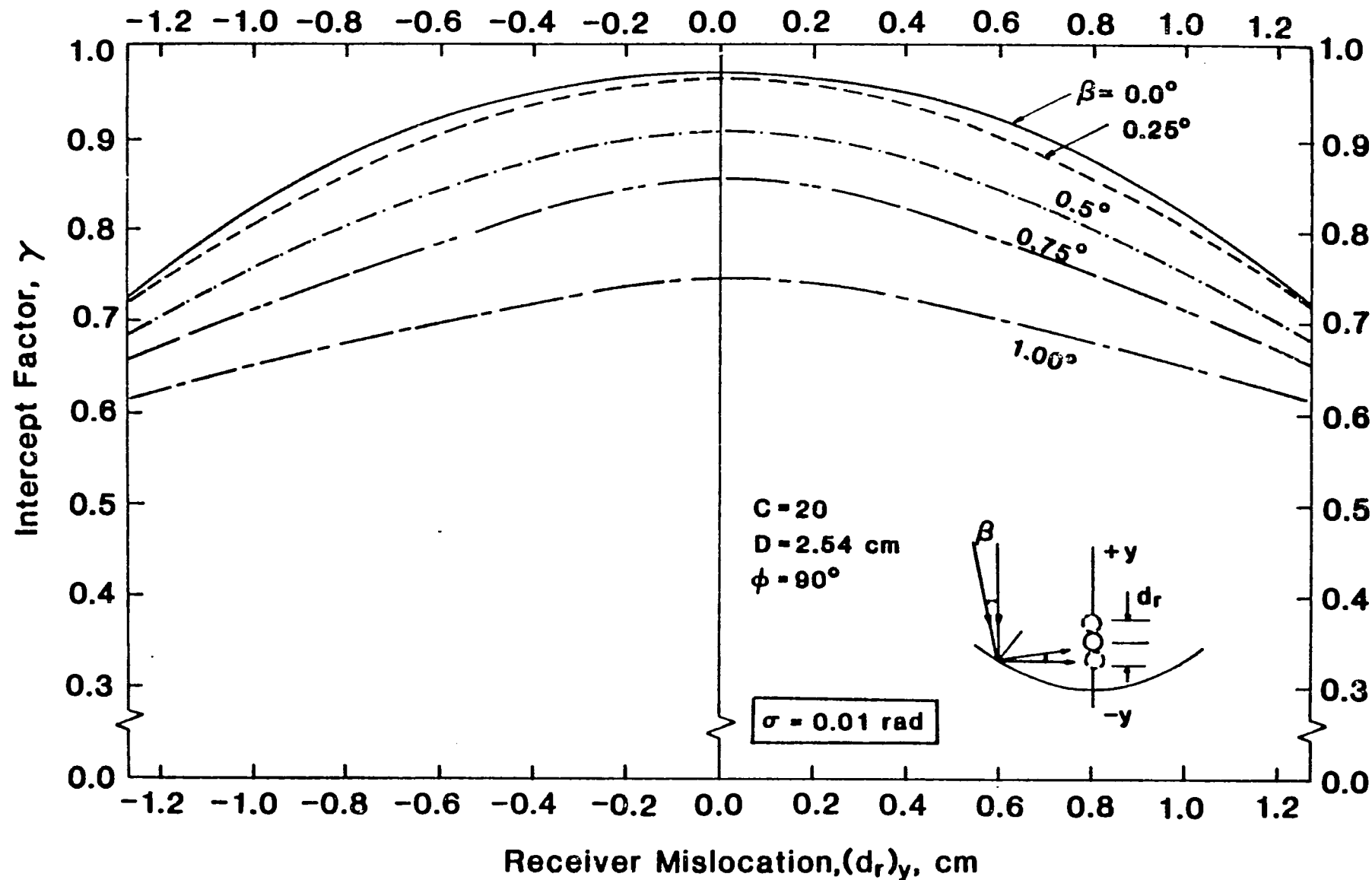


Figure 4.5 Intercept factor as a function of receiver mislocation along the optical axis and tracking error for $\sigma = 0.01$ radian.

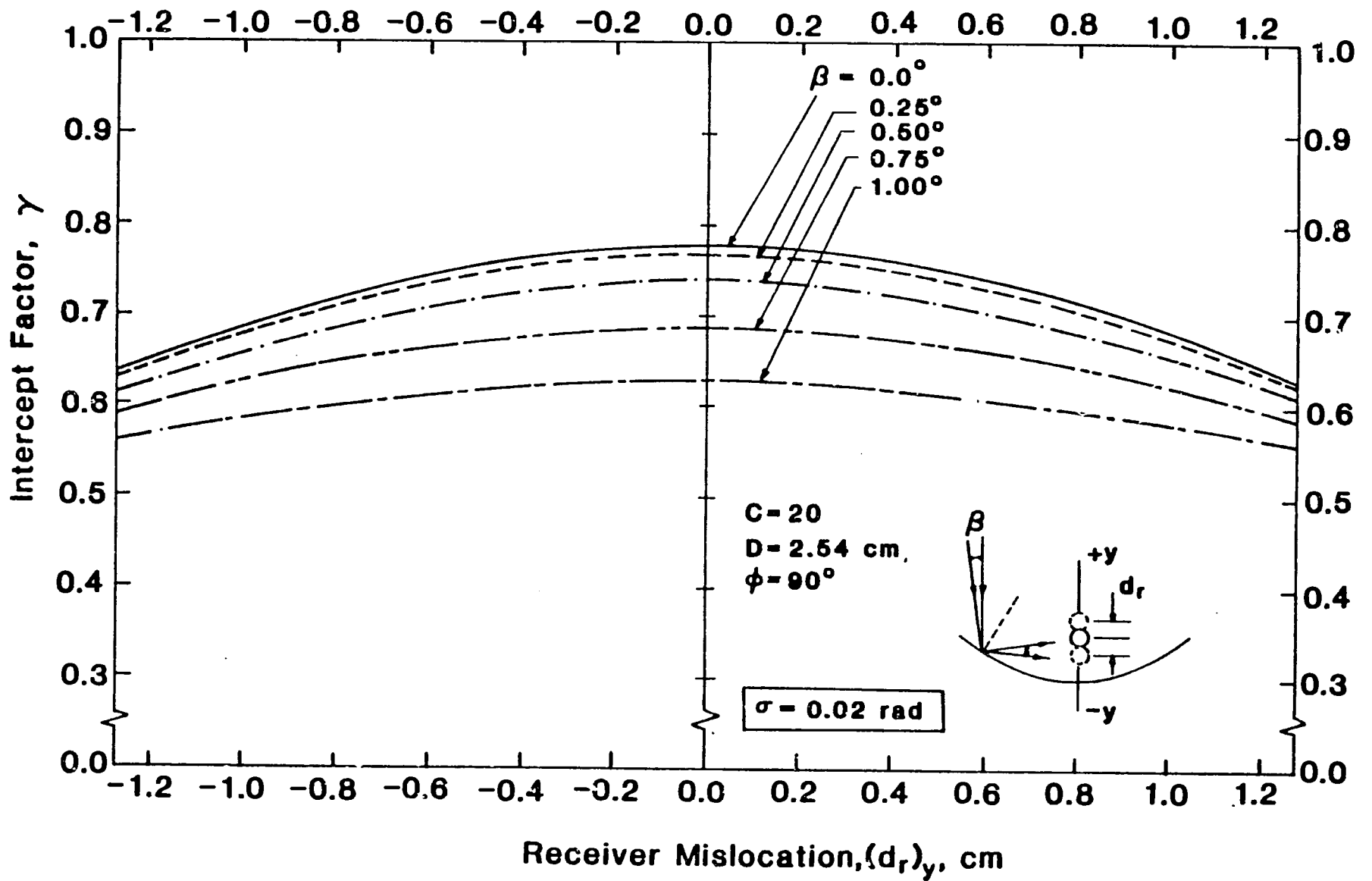


Figure 4.6 Intercept factor as a function of receiver mislocation along the optical axis and tracking error for $\sigma = 0.02$ radian.

combines reflector profile errors with the receiver mislocation errors along the optical axis (see Figure 3.9), will be larger than lateral component of d_r , $(d_r)_x$.

- . Comparison of Figures 4.1-4.3 with Figures 4.4-4.6 shows that, for a given tracking error, the intercept factor drops more rapidly when the receiver is mislocated in the y-direction (except when positive tracking errors, $+\beta$, and receiver mislocation in -x direction exist together). Therefore, $(d_r)_y$ can be taken as the dominant direction for receiver location errors.
- . Unsymmetric effects produced by the receiver mislocation in the lateral axis will introduce undesirable complications into the generalization of the results.

Next, the effect of positive and negative tracking errors ($\pm \beta$) for different random error levels is studied (Figures 4.7 and 4.8). As shown in the figures, when receiver mislocations in the y-direction alone are considered, positive and negative tracking errors produce the same effect and of course this will be helpful in the generalization of the results that will follow shortly.

In Figures 4.9 through 4.18, the effect of changing the geometric parameters, C and D is studied. Also in these figures are presented justifications for combining the error variables σ , β , and $(d_r)_y$ with the geometric variables C and D to yield a set of three error parameters universal to all collector geometries.

In Figure 4.9 concentration ratio C is plotted versus intercept factor, γ , for different random error levels. The

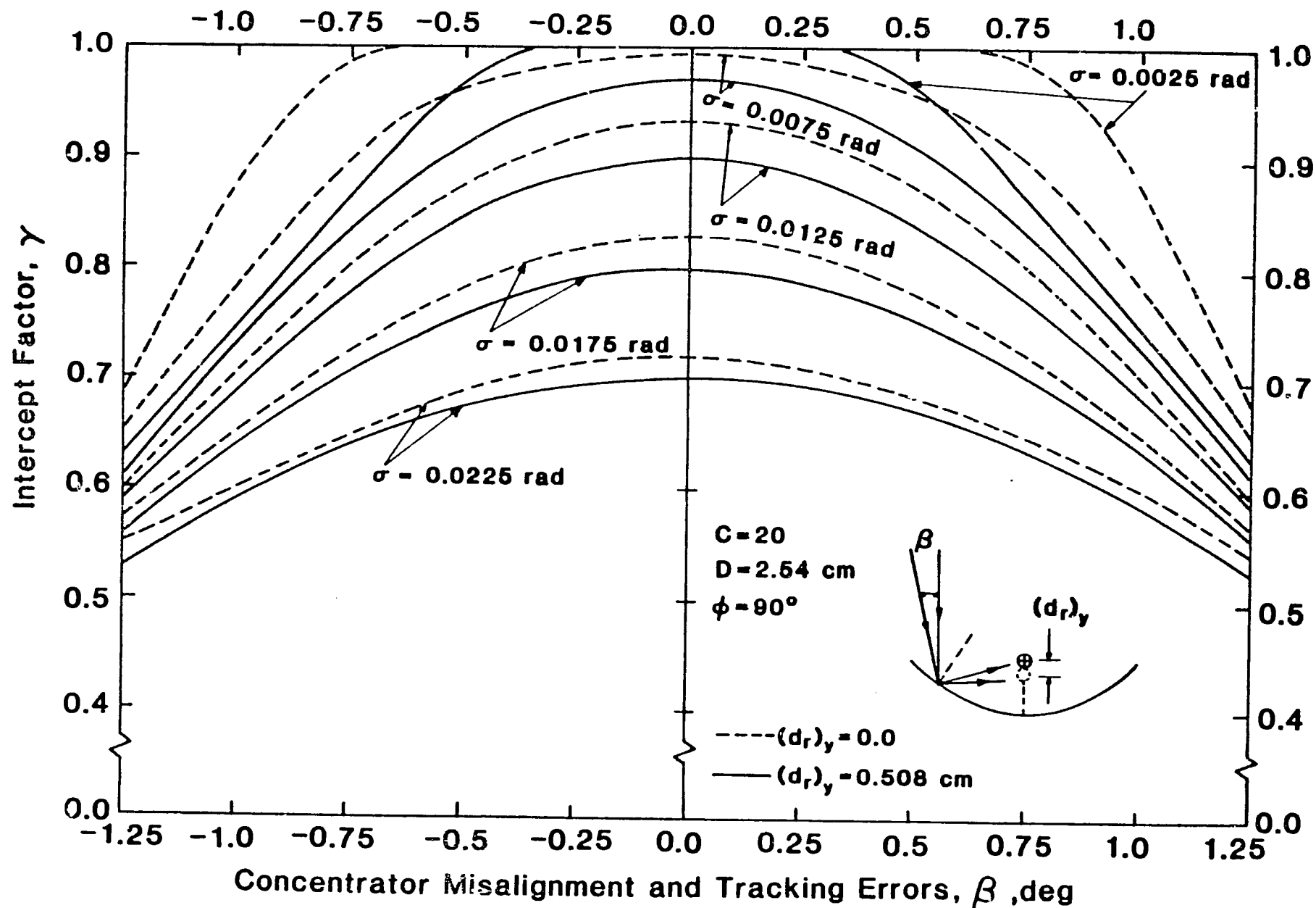


Figure 4.7 Intercept factor as a function of tracking error and random errors for $(d_r)_y = 0.0$ and 0.508 cm.

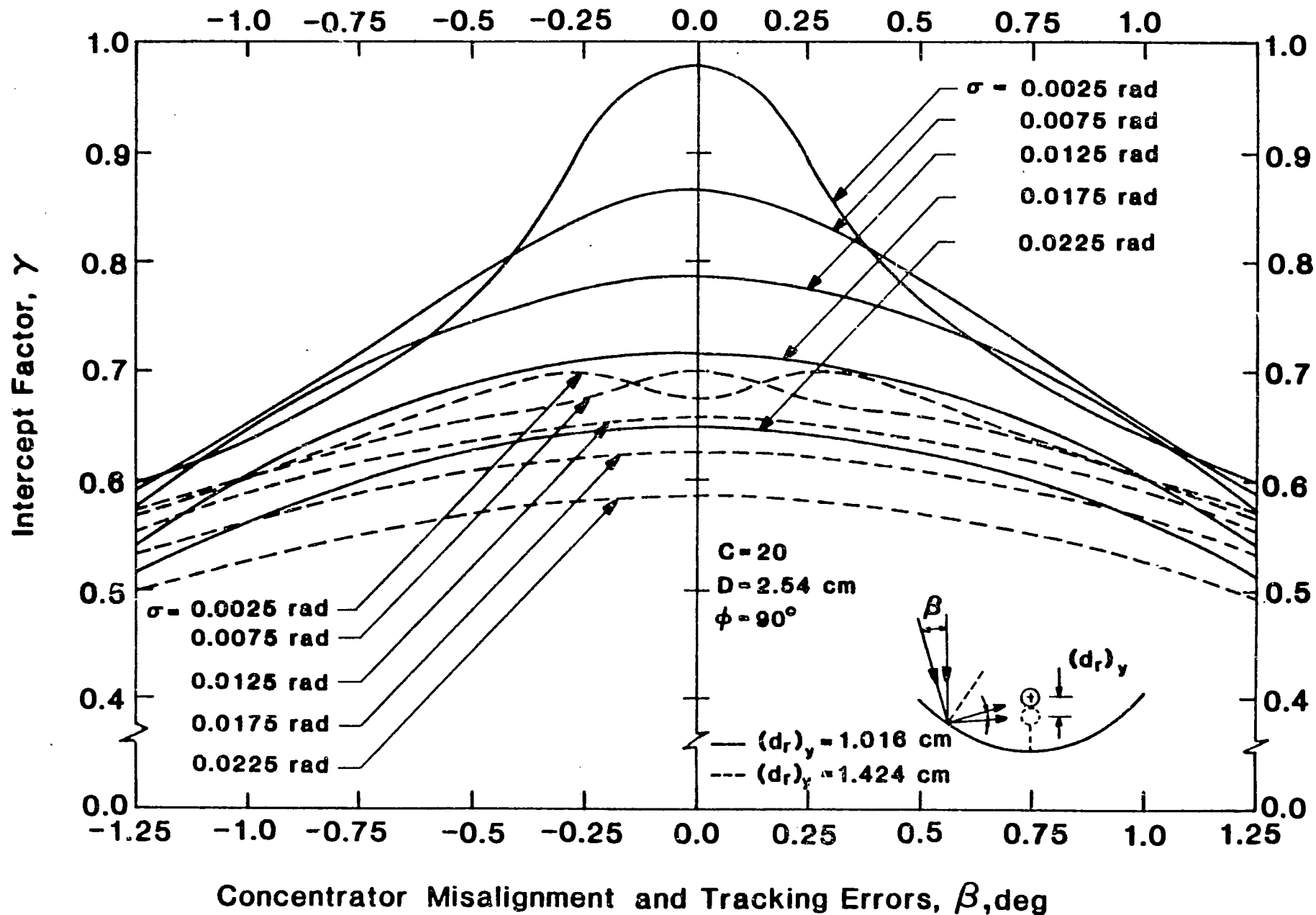


Figure 4.8 Intercept factor as a function of tracking error and random errors for $(d_r)_y = 1.016$ and 1.424 cm.

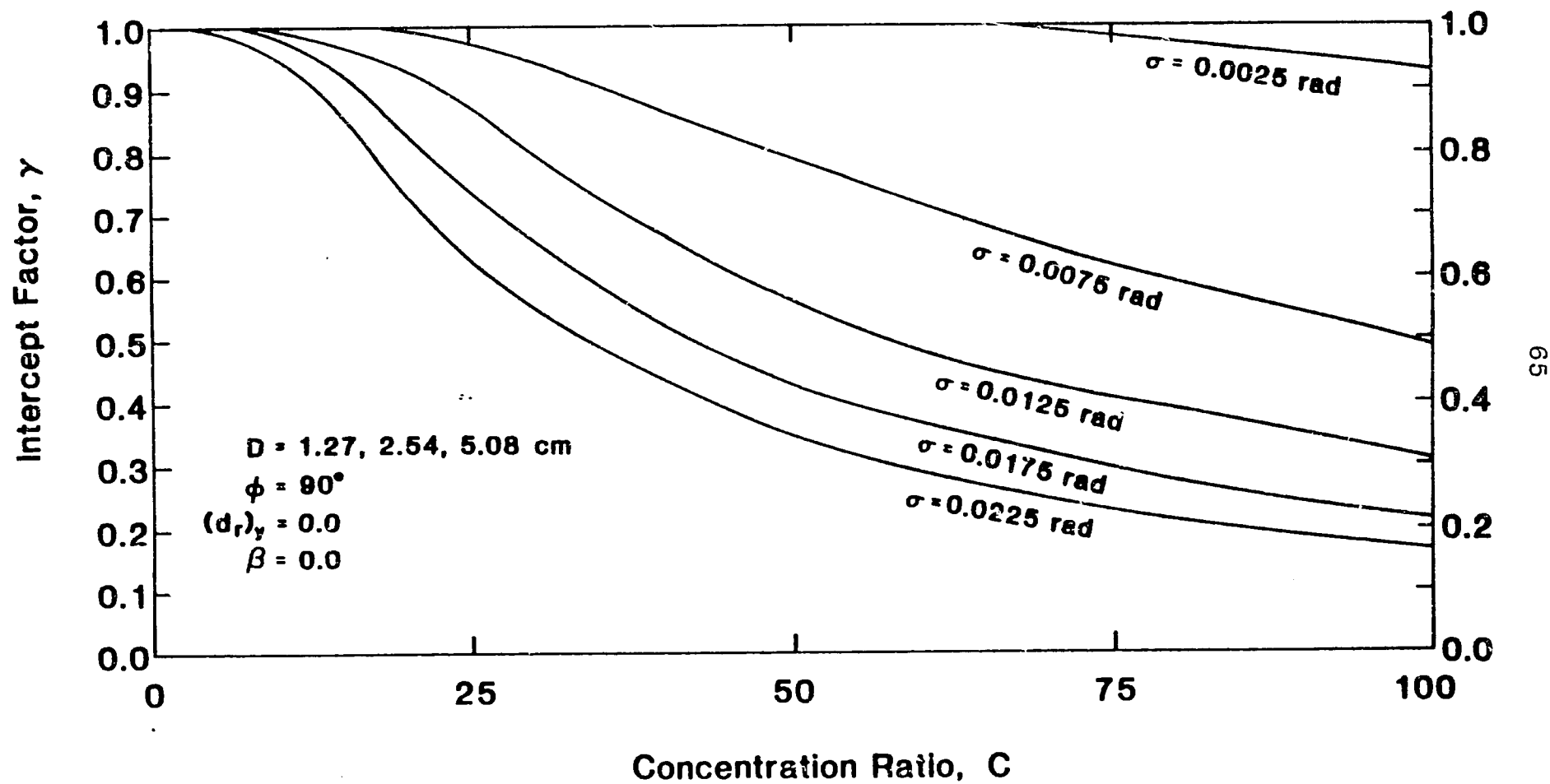


Figure 4.9 Intercept factor as a function of concentration ratio and random error parameter (zero non-random errors).

results are repeated for three different values of absorber tube diameter and it was found that, for perfect tracking ($\beta=0$) and perfectly aligned receiver (i.e., $(d_r)_y=0$), the intercept factor is not a function of the absorber tube diameter. As shown in the figure, the intercept factor decreases as the concentration ratio increases. This decrease is more pronounced for higher random error levels. In Figure 4.10, the intercept factor is plotted against a new parameter, $\sigma^*=\sigma C$, which is called the 'universal random error parameter'. This parameter collapses the five curves in Figure 4.10 into a single curve.

In Figures 4.11 to 4.13, again the concentration ratio C is plotted versus intercept factor, this time for different tracking errors and for three fixed random error level, $\sigma^*=0.05, 0.1, 0.2$ rad. As expected, the figures show that, intercept factor rapidly drops to zero when concentration ratio increases; this is particularly true for large tracking errors. Again, it is found that, for a perfectly aligned receiver, i.e., $(d_r)_y=0.0$, intercept factor is not a function of the absorber tube diameter. Figure 4.15 shows that curves in each of the Figures 4.11, 4.12 and 4.13 reduce to a single curve when intercept factor is plotted against a 'universal non-random error parameter', β^* , which is the product of the tracking error and the concentration ratio.

Figures 4.15 and 4.16 show plots of intercept factor versus concentration ratio for different receiver location

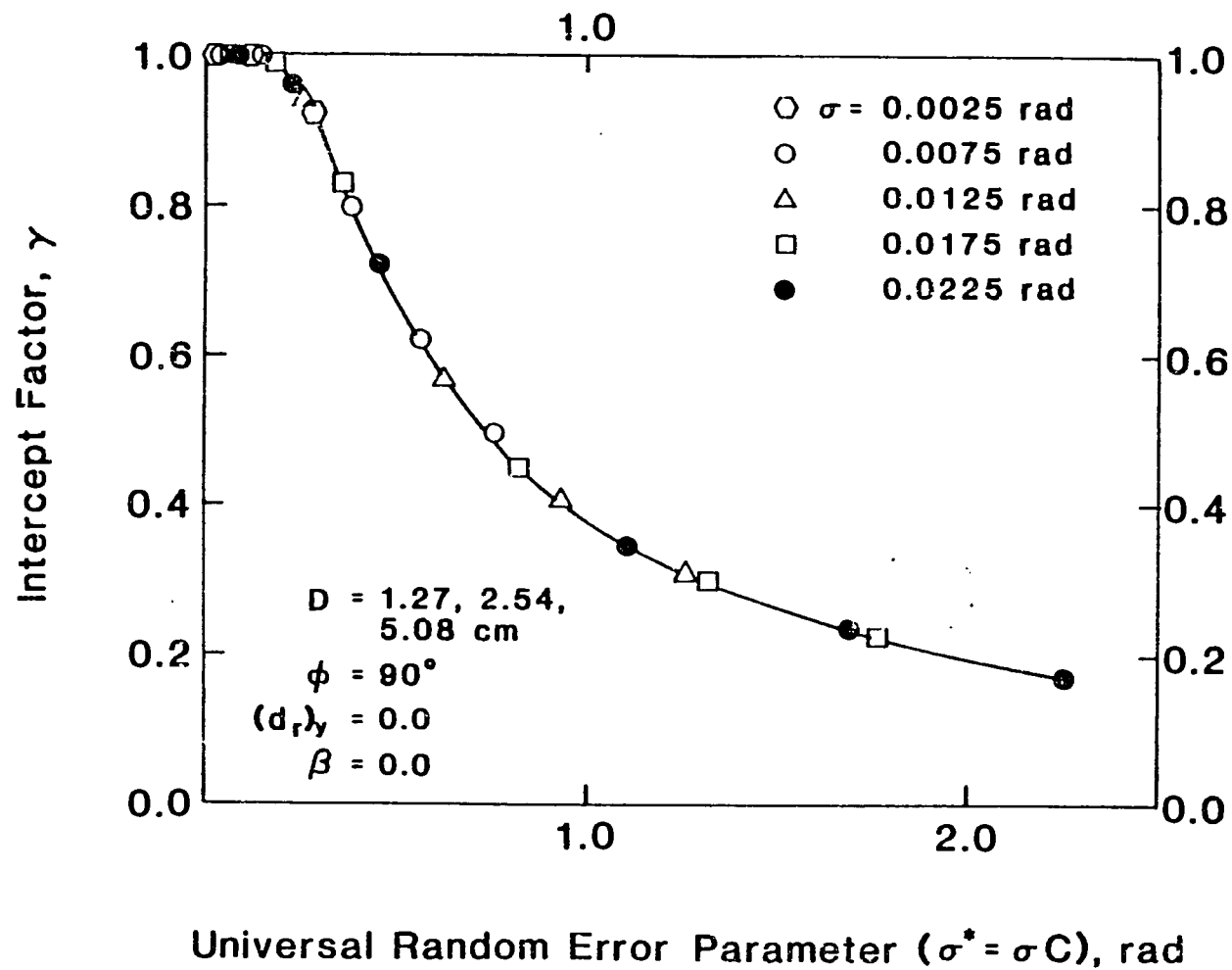


Figure 4.10 Intercept factor as a function of the universal random error parameter (zero non-random errors).

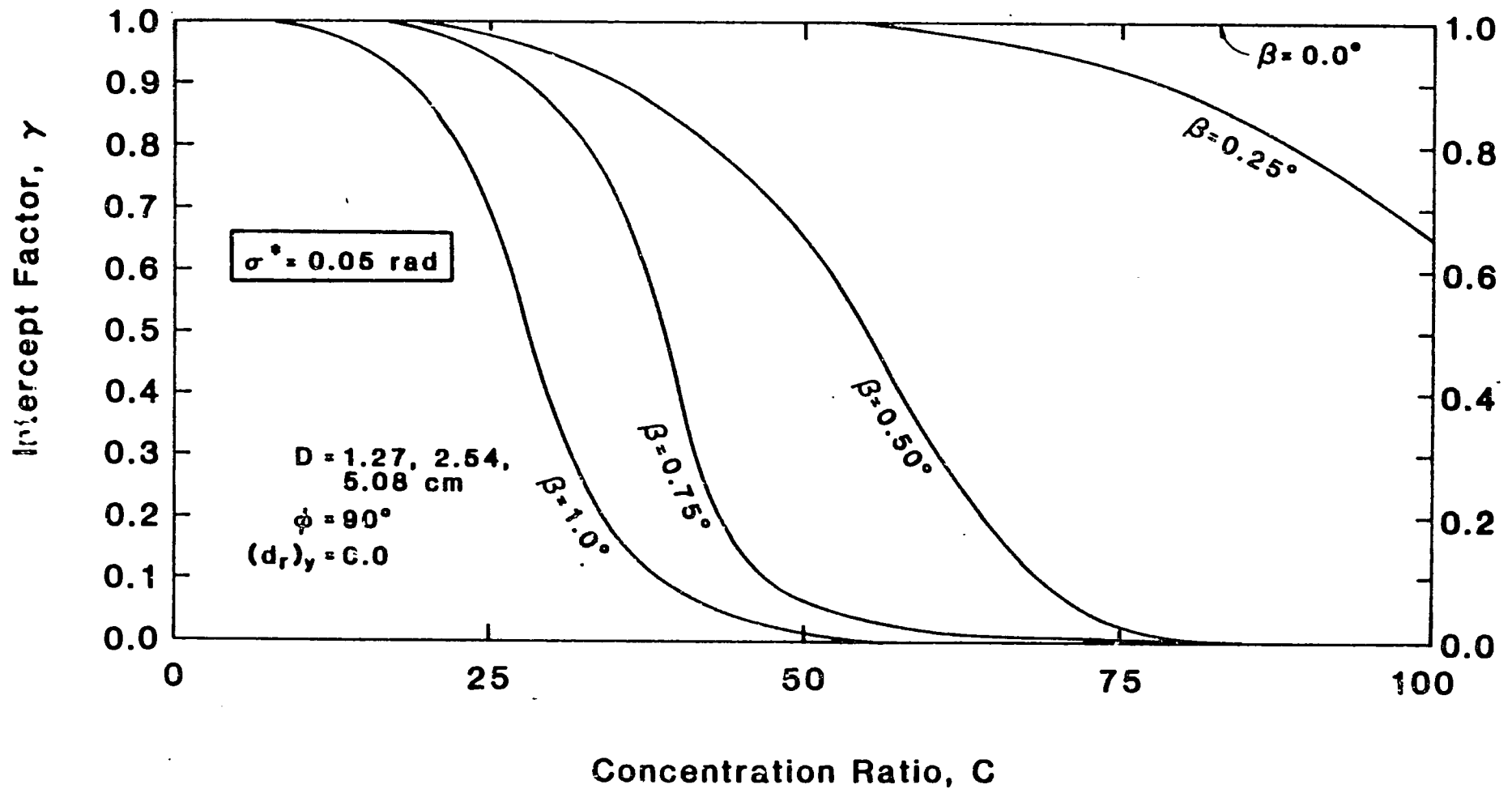


Figure 4.11 Intercept factor as a function of concentration ratio and tracking error for $\sigma^* = 0.05$ radian and $(d_r)_y = 0.0$.

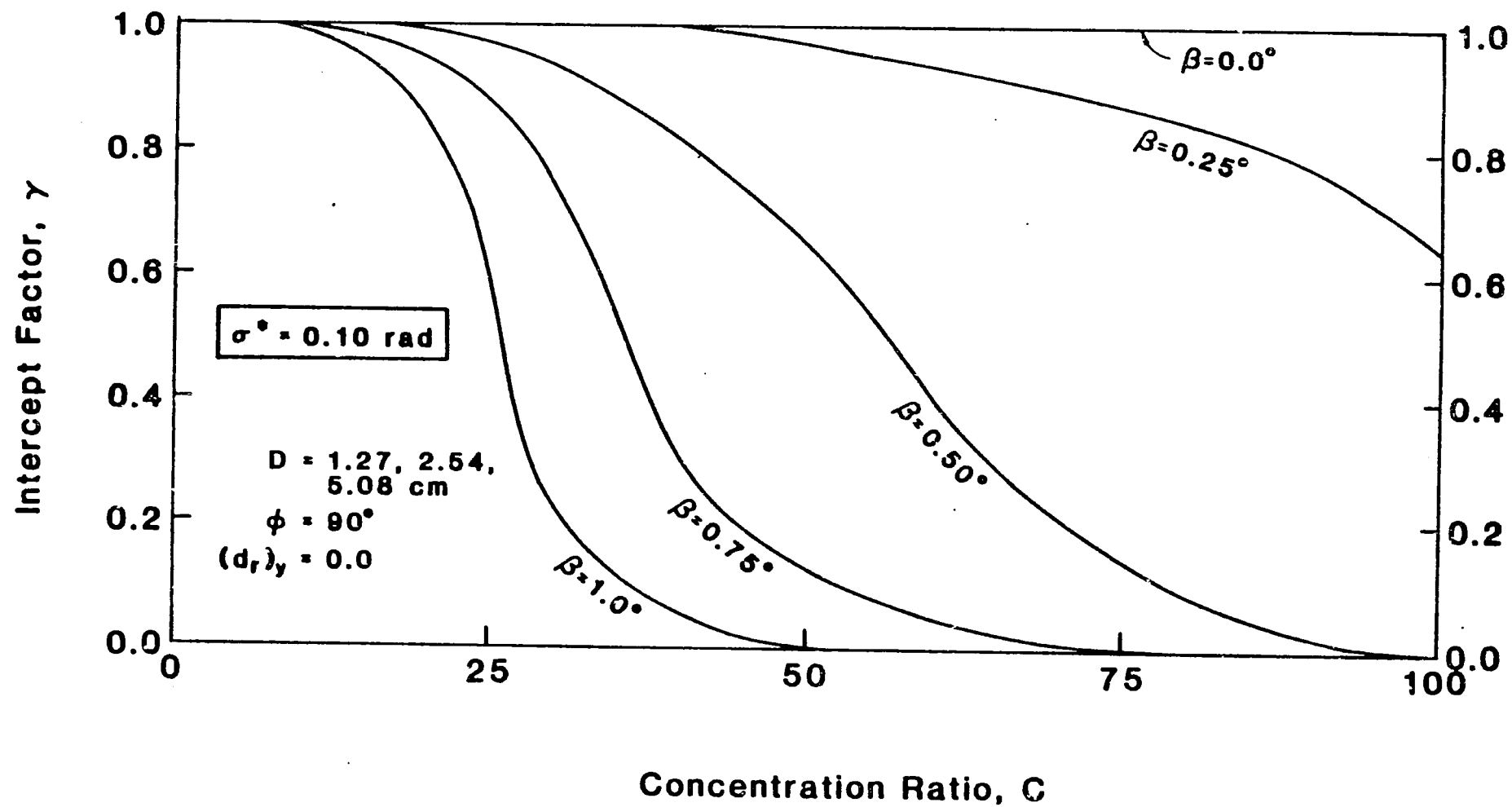


Figure 4.12 Intercept factor as a function of concentration ratio and tracking error for $\sigma^* = 0.10$ radian and $(d_r)_y = 0.0$.

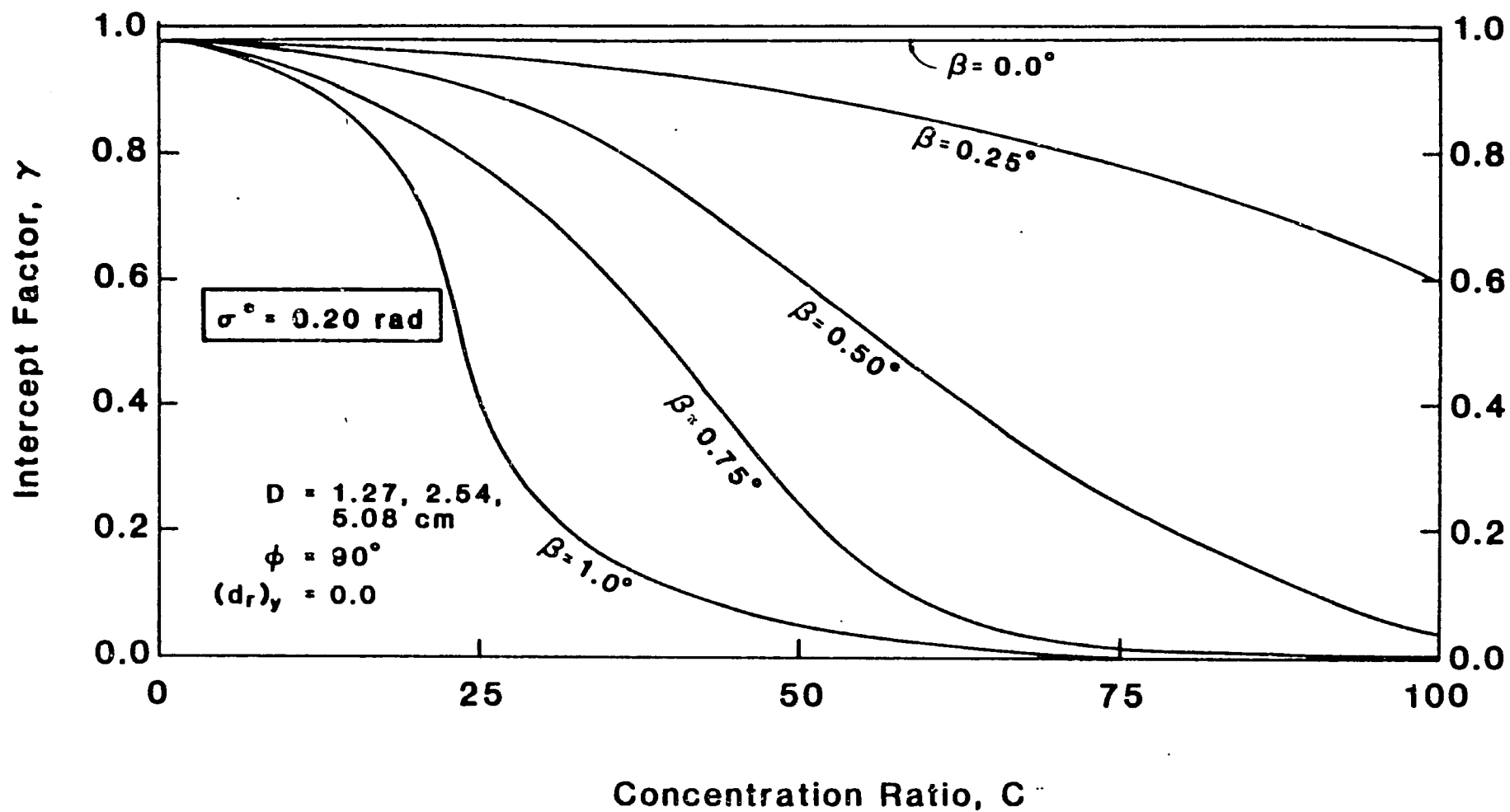
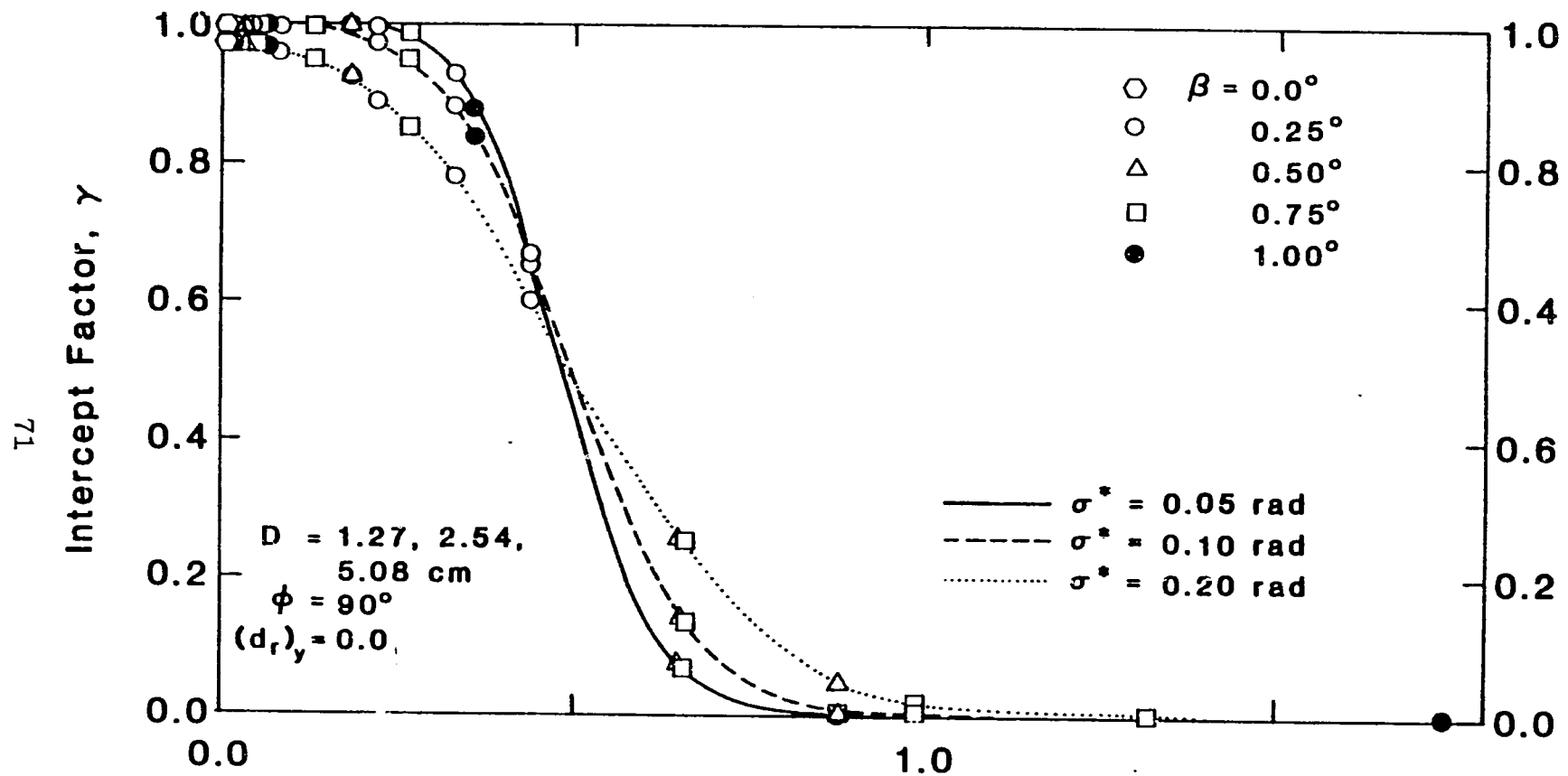


Figure 4.13 Intercept factor as a function of concentration ratio and tracking error for $\sigma^* = 0.20$ radian and $(d_r)_y = 0.0$.



Universal Non-Random Error Parameter ($\beta^* = \beta C$), rad

Figure 4.14 Intercept factor as a function of the universal non-random error parameter due to angular errors (β^*) and various random error levels (zero receiver location error).

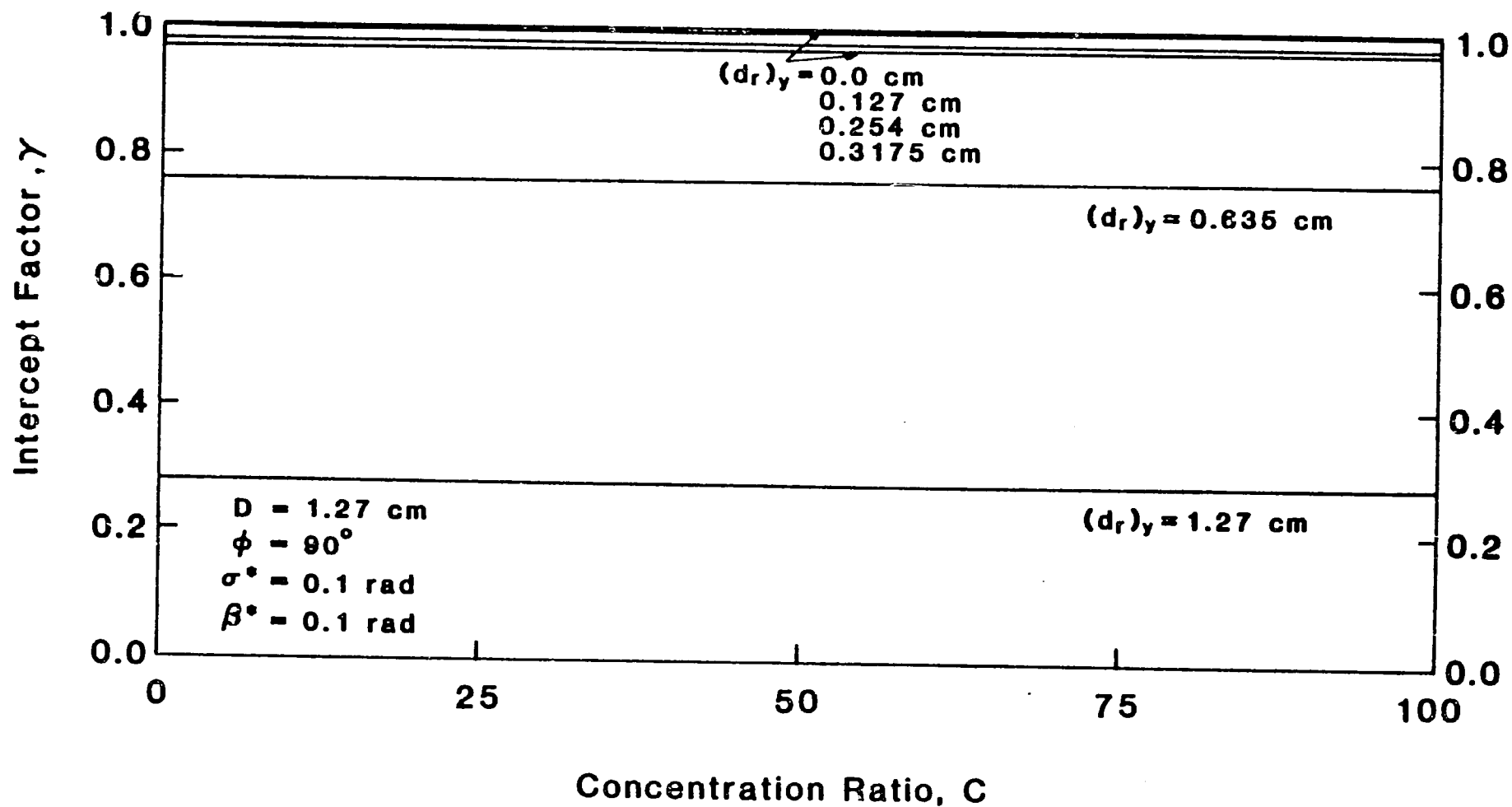


Figure 4.15 Intercept factor as a function of concentration ratio and receiver mislocation for $D = 1.27$ cm.

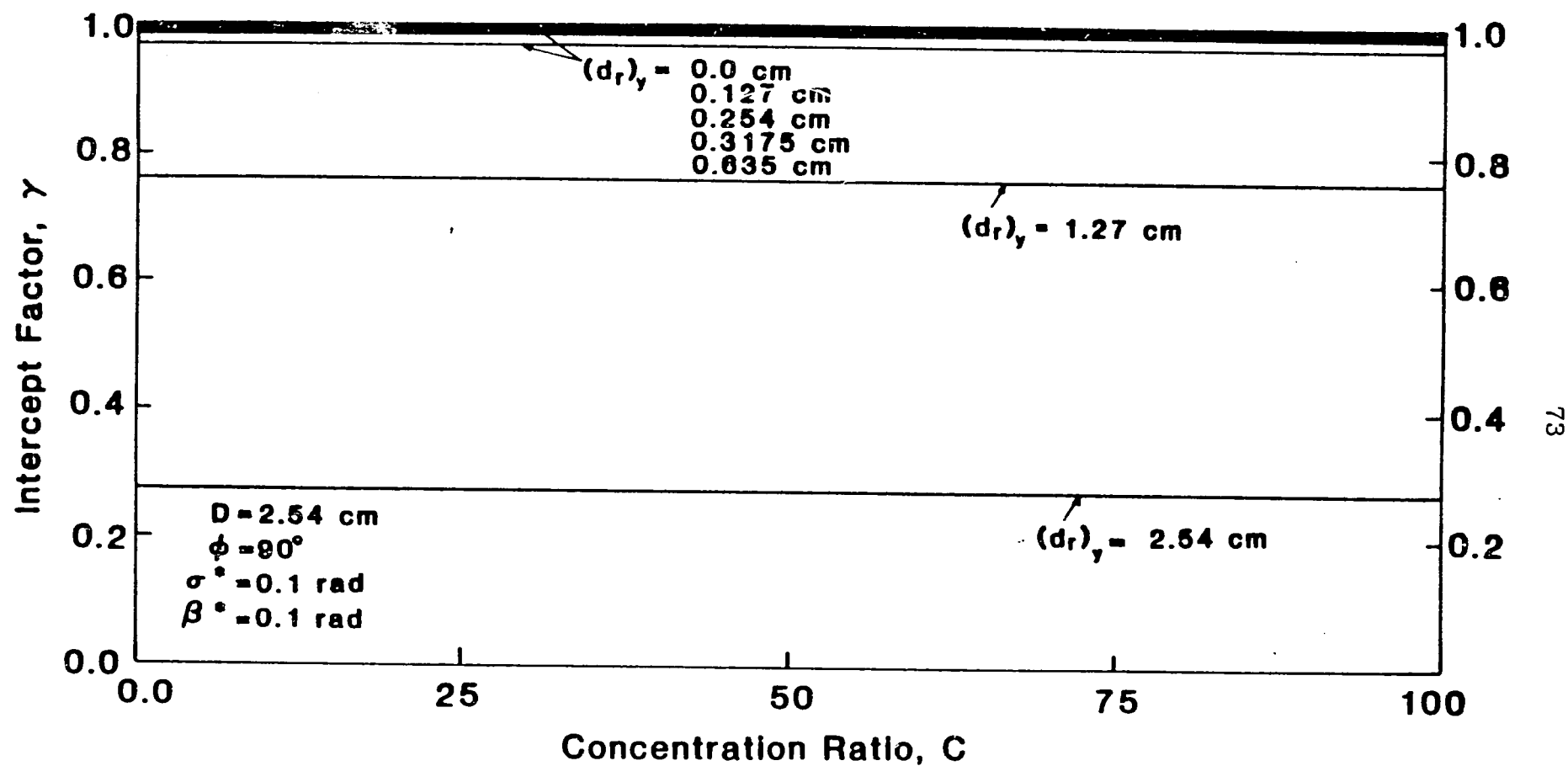


Figure 4.16 Intercept factor as a function of concentration ratio and receiver mislocation for $D = 2.54 \text{ cm}$.

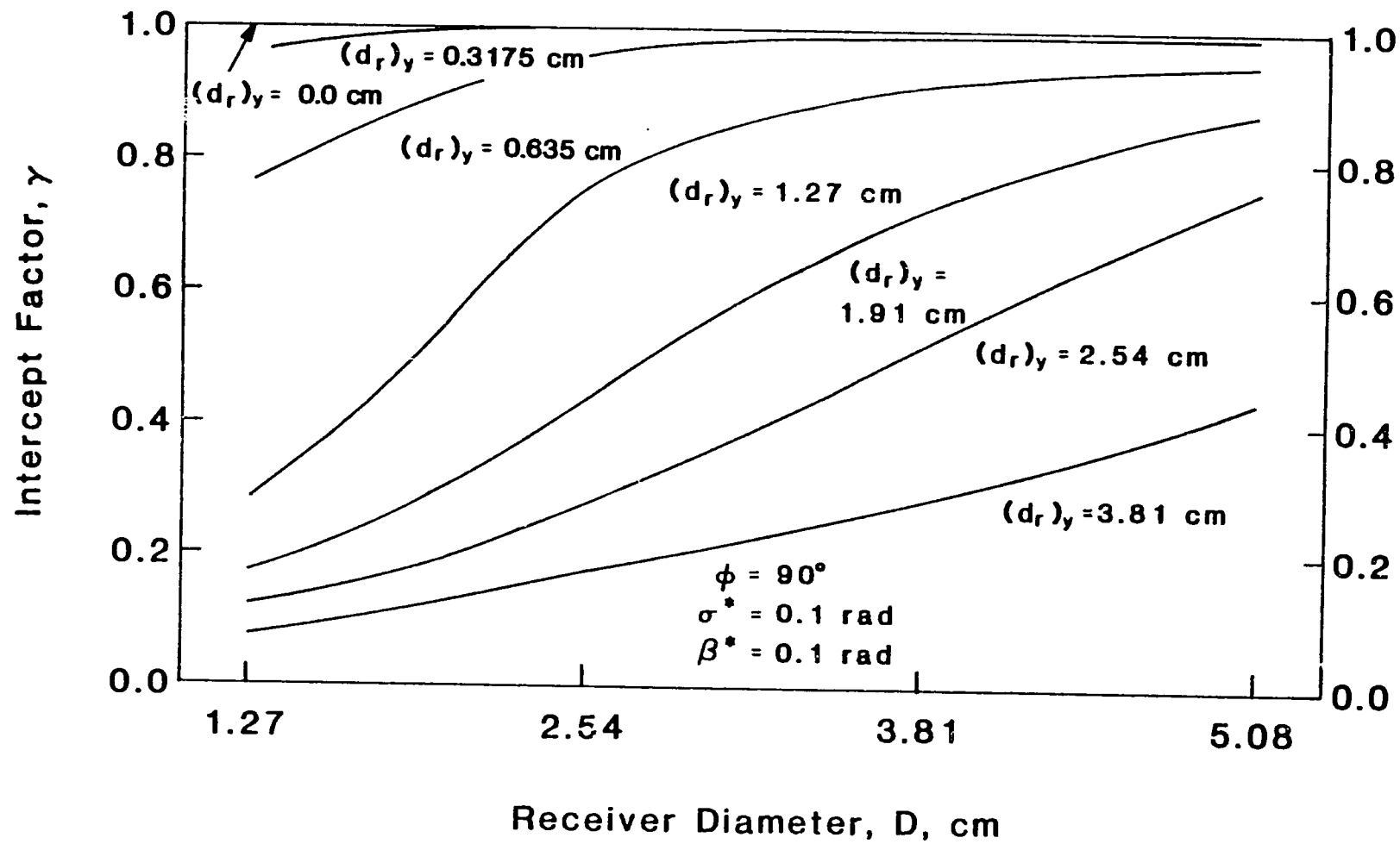


Figure 4.17 Intercept factor as a function of receiver diameter and receiver location error.

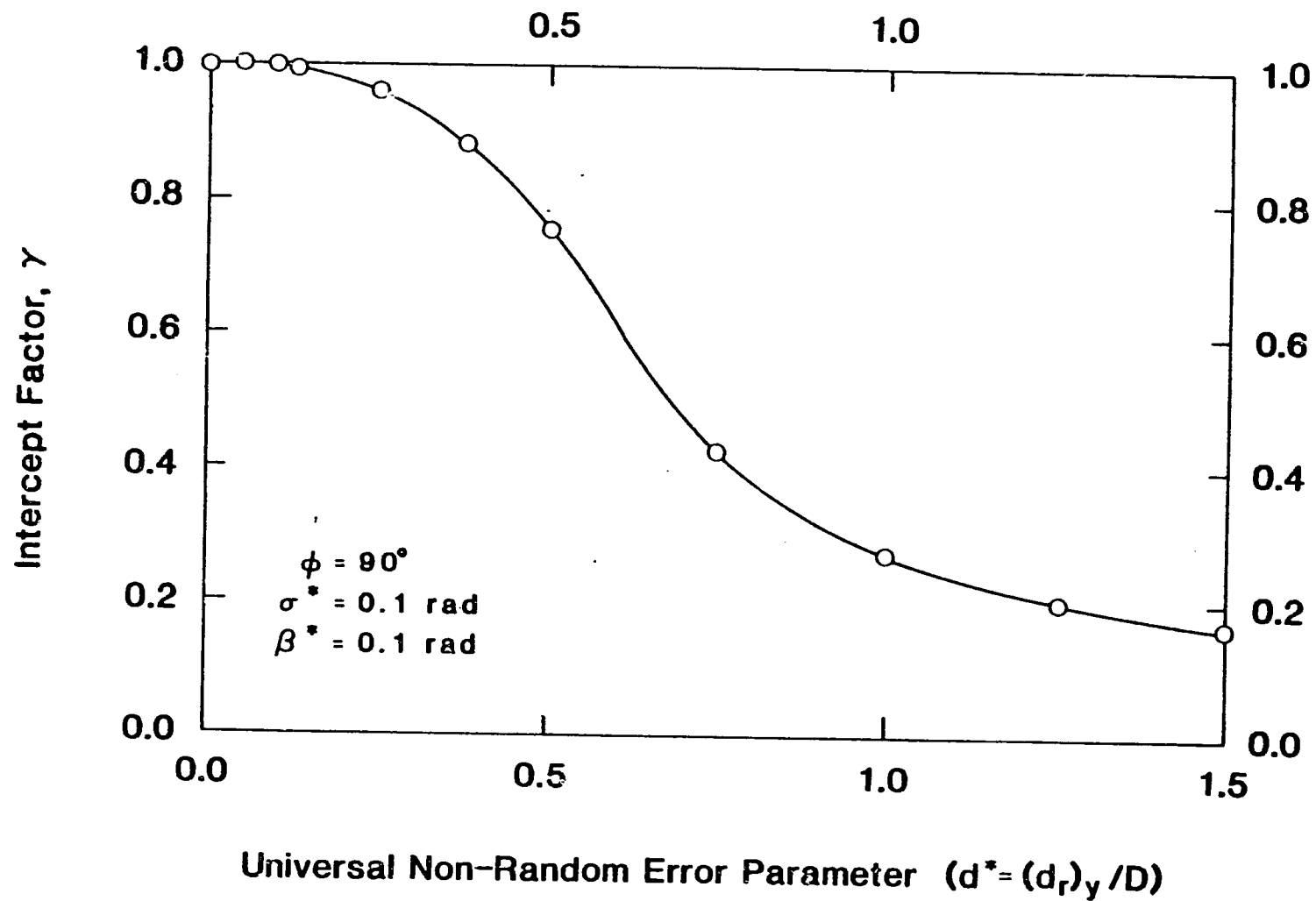


Figure 4.18 Intercept factor as a function of the universal non-random error parameter due to receiver mislocation.

errors. It is evident that for fixed values of σ^* and β^* , the intercept factor is not a function of C . Next, the intercept factor is plotted versus absorber tube diameter; this plot is shown in Figure 4.17. Finally, Figure 4.18 shows the combination of the receiver location error, $(d_r)_y$, with the absorber tube diameter, $d^* = (d_r)_y / D$, to yield the second universal non-random error parameter.

As a result of the discussed computer simulations, the number of independent variables in Eq. (4.1) have been reduced to four. Therefore, the equation can be rewritten as:

$$\gamma = \text{fn}(\phi, \sigma^*, \beta^*, d^*) \quad (4.2)$$

where,

$$\begin{aligned} \sigma^* &= \sigma C = \text{Universal random error parameter,} \\ &\quad (\sigma = \text{standard deviation of the reflected} \\ &\quad \text{energy distribution}) [\text{rad}] \\ \beta^* &= \beta C = \text{Universal non-random error parameter due to} \\ &\quad \text{angular errors,} \\ &\quad (\beta = \text{tracking or reflector misalignment error}) \\ &\quad [\text{rad}] \\ d^* &= \frac{(d_r)_y}{D} = \text{Universal non-random error parameter due to} \\ &\quad \text{receiver mislocation,} \\ &\quad ((d_r)_y = \text{distance between effective focus and} \\ &\quad \text{center of absorber tube measured along the axis} \\ &\quad \text{of the reflector profile (see Fig. 3.9))} \\ &\quad [\text{dimensionless}]. \end{aligned}$$

This reduction in the number of independent variables in (Eq. (4.1)) is a significant finding because it allows for gener-

alization of results and meaningful optimization of the collector geometry. Analytical derivation of the universal parameters are presented elsewhere [33]. The next chapter presents results of optical analysis using the universal error parameters.

Chapter Five

RESULTS OF THE COMPREHENSIVE OPTICAL ANALYSIS

5.1 Introduction

In the previous chapter, Chapter Four, the preliminary results from the comprehensive optical model were presented. As a result of the preliminary analyses, a set of universal error parameters which combine the collector geometry parameters with the error parameters were derived. In this chapter, the results of an in-depth optical analysis of PTC's (using the derived universal error parameters) are presented.

First, the effect of the random errors alone on the intercept factor is analyzed. Results from this analysis are compared with those of the previous investigators.

Second, the effect of the combined random and non-random errors are studied. In particular, the effect of changing the collector rim angle is studied. The concept of 'error-tolerant' trough design (i.e., designs which have built-in tolerances for potential manufacture, assembly and operation errors) is introduced and methods for determination of error tolerances are given. The error-tolerant trough design concept is particularly suitable for developing country applications.

Finally, the sensitivity of the error tolerances to changes

in rim angle (i.e., optimal rim angles) is studied.

5.2 Result Of Optical Analysis With Random Errors Alone

For zero non-random errors (i.e., $\beta^*=0.0$ and $d^*=0.0$) Eq.(4.2) becomes a function of rim angle and the 'universal random error parameter' only, i.e.,

$$\gamma = \text{fn}(\phi, \sigma^*)$$

With this limitation the results can be presented in two-dimensional graphs. Figure 5.1 shows a plot of γ versus σ^* for different rim angles while 5.2 shows the cross plot, γ versus rim angle for different random error levels. As shown in Figure 5.1, higher random error levels can be tolerated with higher rim angles. However, the trend starts to reverse itself after a rim angle of 105° . For example, a 105° -rim angle reflector performs better than 120° -rim angle reflector for σ^* less than 0.2 radians (curves cross each other at $\sigma^* \approx 0.22$). This is due to the increase in the average reflector-to-absorber distance of the higher rim angle reflector. As shown in Figure 5.2 the optimum rim angle based on the random errors alone, is so broad (in the range of 80° to 120°) that the final choice of rim angle can be determined by other considerations as:

- (i) non-random error-tolerances,
- (ii) mechanical strength of the reflector, and
- (iii) ease of manufacture.

The results presented in this section can be compared

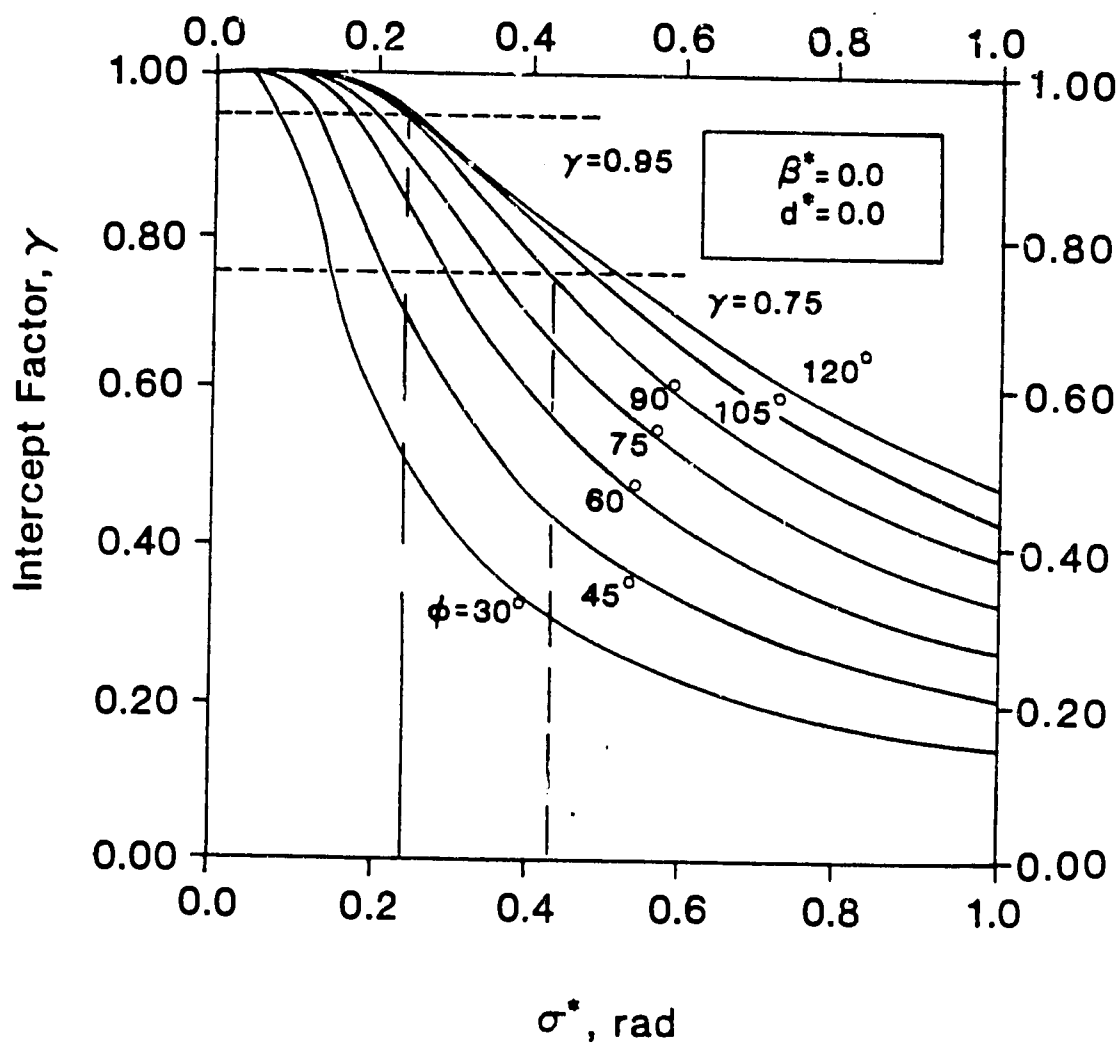


Figure 5.1 Intercept factor as a function of the universal random error parameter and rim angle (zero non-random errors).

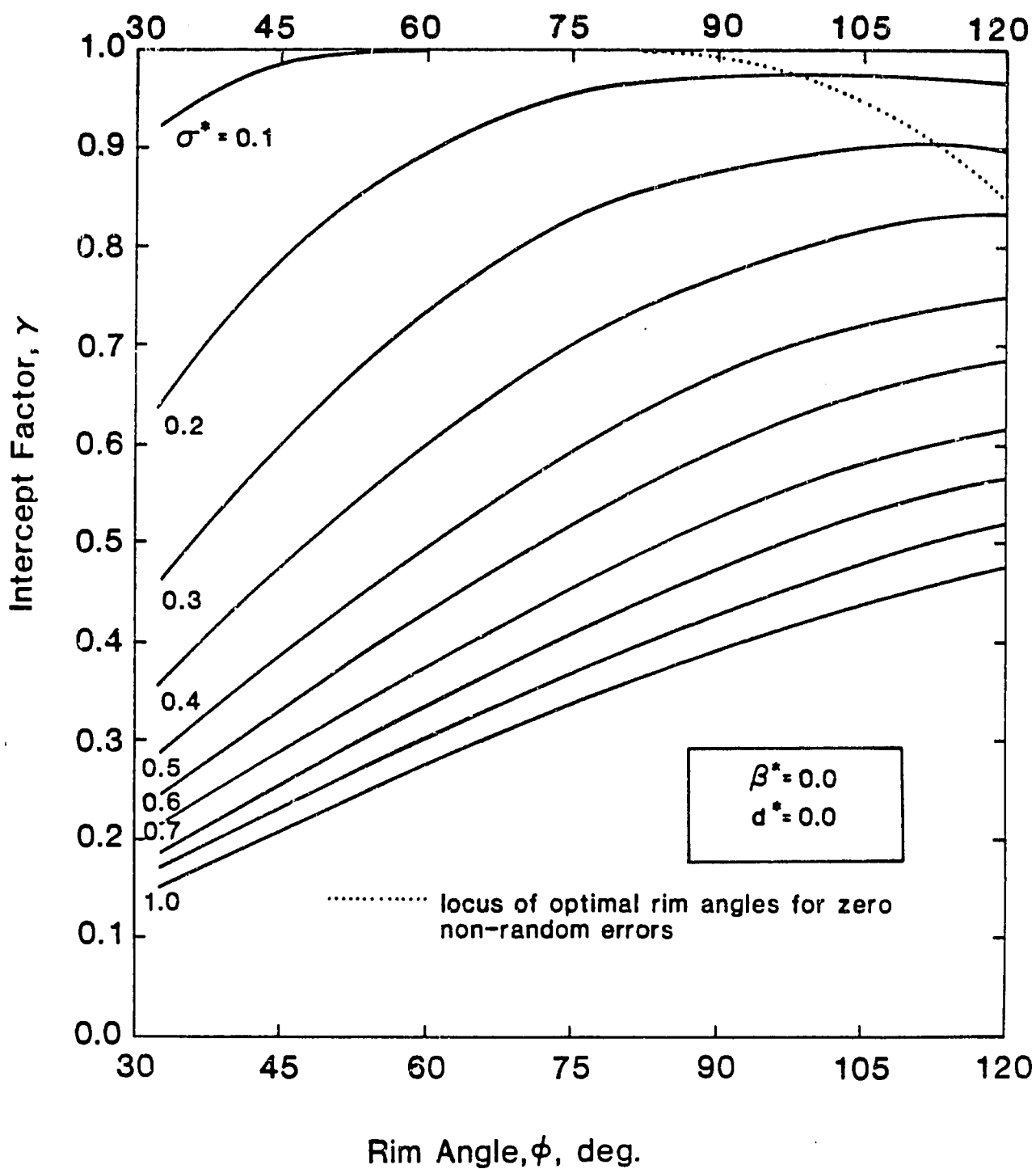


Figure 5.2 Intercept factor versus rim angle and the universal random error parameter (zero non-random errors).

to those of the previous investigators who assumed normal distributions for all optical errors. Figure 5.1 and 5.2 were compared with similar plots found in Ref. [16 and 34], where a purely analytical technique is used to calculate the geometric intercept factor (opposed to the numerical ray trace technique used in the present study); the two results are found to be almost identical. This close agreement validates the present calculational procedure. The present results could not be compared with those of any other investigators because, in their studies [13,15], they did not explicitly report the optical efficiency or the geometric intercept factor. Instead their results display only the overall collector efficiency for chosen operating conditions which makes direct comparison with the present results impossible.

5.3 Results Of Optical Analysis With Random And Non-random Errors

Figure 5.3 shows that for a given random error level (σ^*) and rim angle (ϕ) the intercept factor can be plotted as a function of β^* and d^* in a three-dimensional graph. Then, for a given intercept factor level ($\gamma=0.75, 0.95\dots$), the non-random error effects can be shown in two-dimensional curves. Figures 5.4 to 5.8 illustrate the allowable level of random and non-random errors (in order to achieve an intercept factor of 0.95) for rim angles 80° to 120° . Likewise, Figures 5.9 to 5.13 show the allowable level of error in order to achieve an intercept factor of 0.75. The vertical

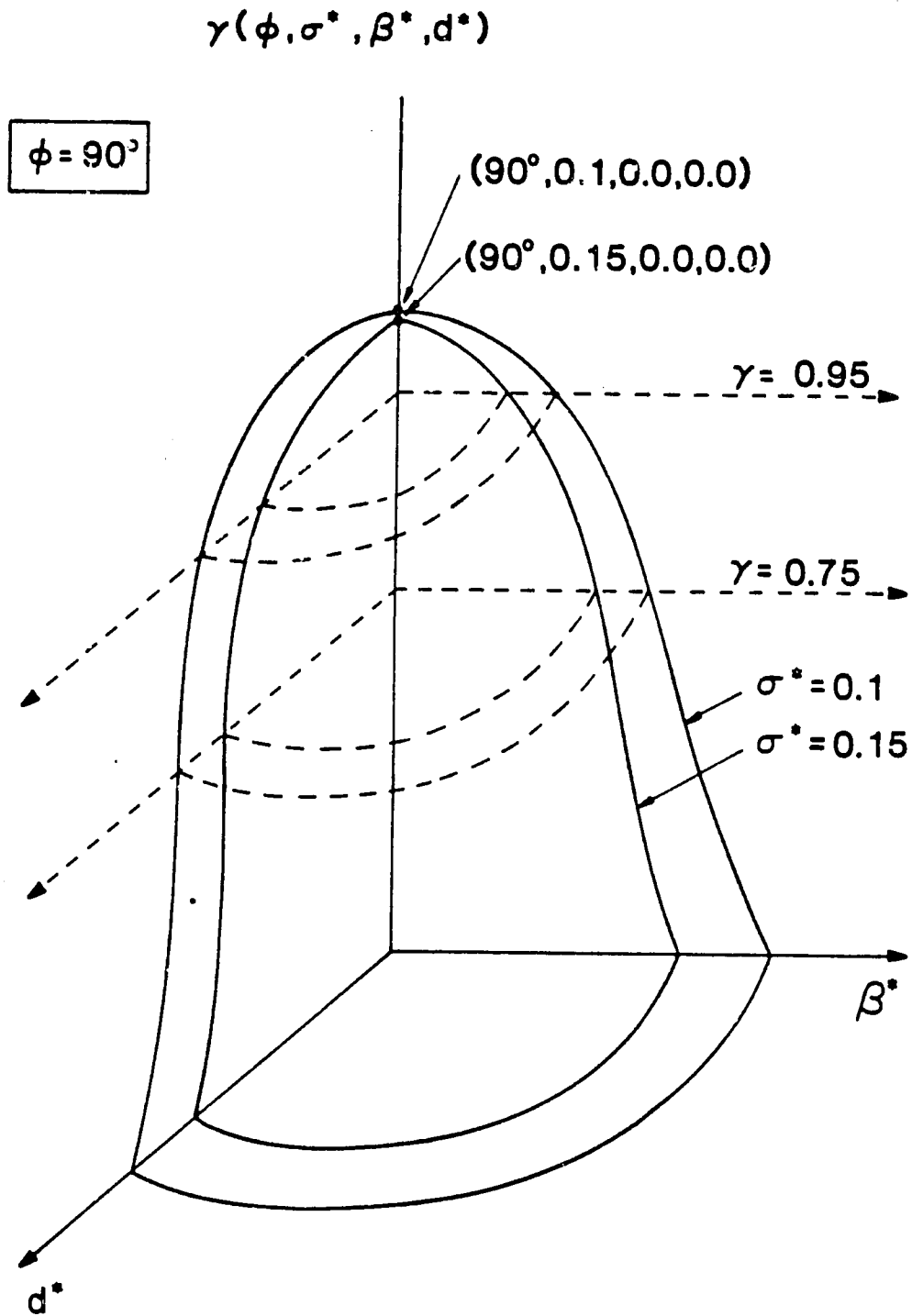


Figure 5.3 Qualitative representation of intercept factor as a function of the non-random error parameters for fixed rim angle and various values of random error parameters.

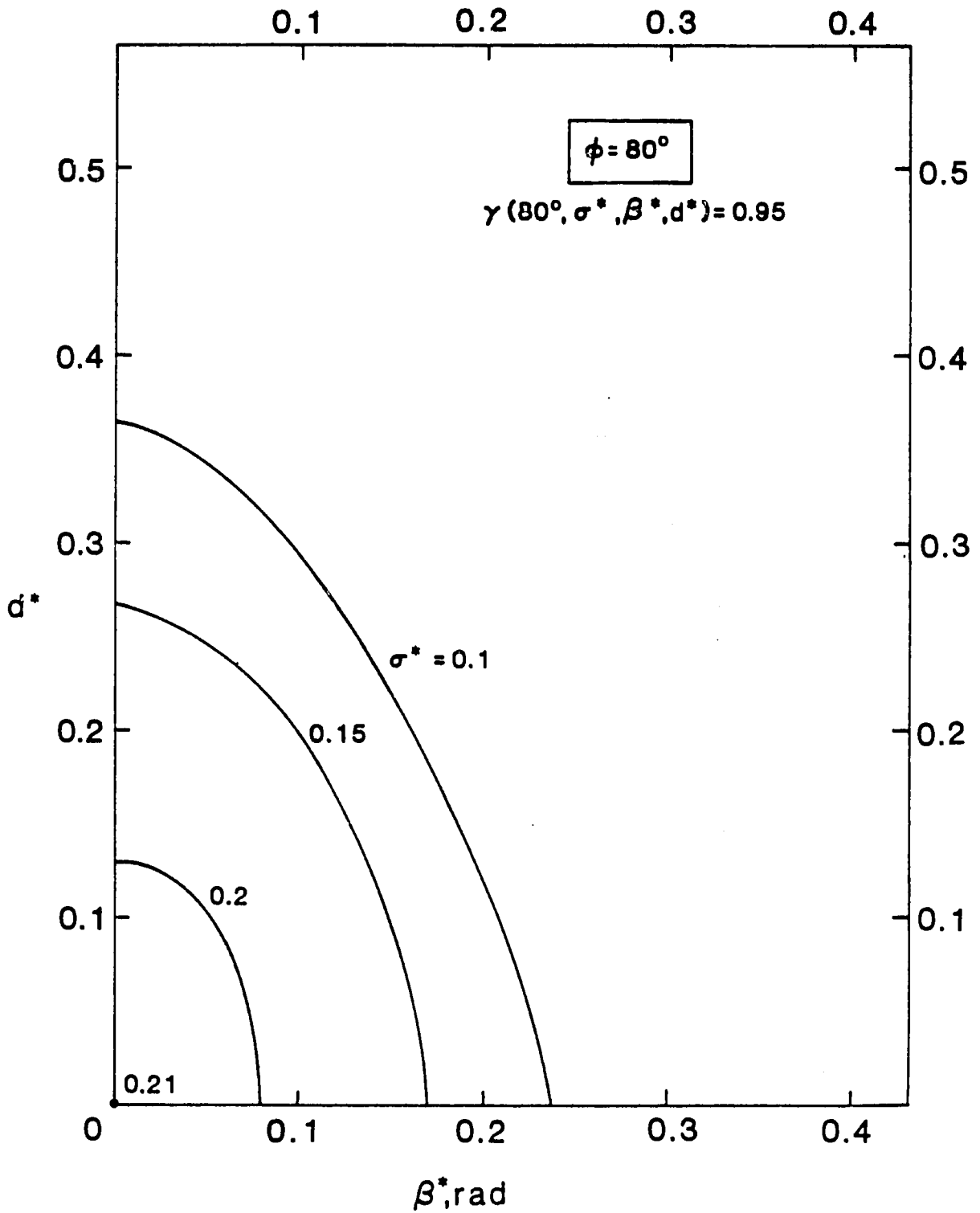


Figure 5.4 Allowable non-random error levels for $\gamma = 0.95$ and $\phi = 80^\circ$ and various random error levels.

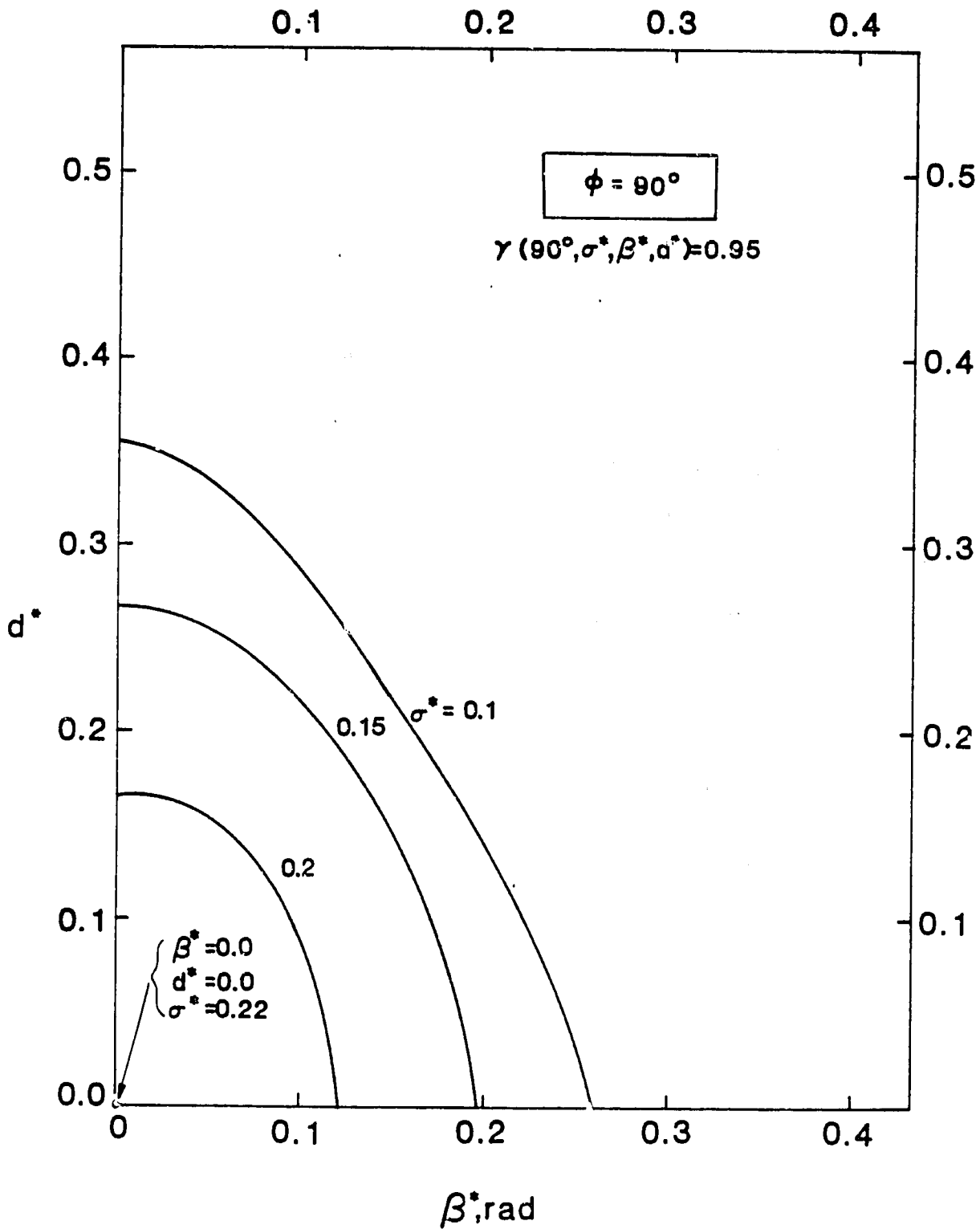


Figure 5.5 Allowable non-random error levels for $\gamma = 0.95$ and $\phi = 90^\circ$ and various random error levels.

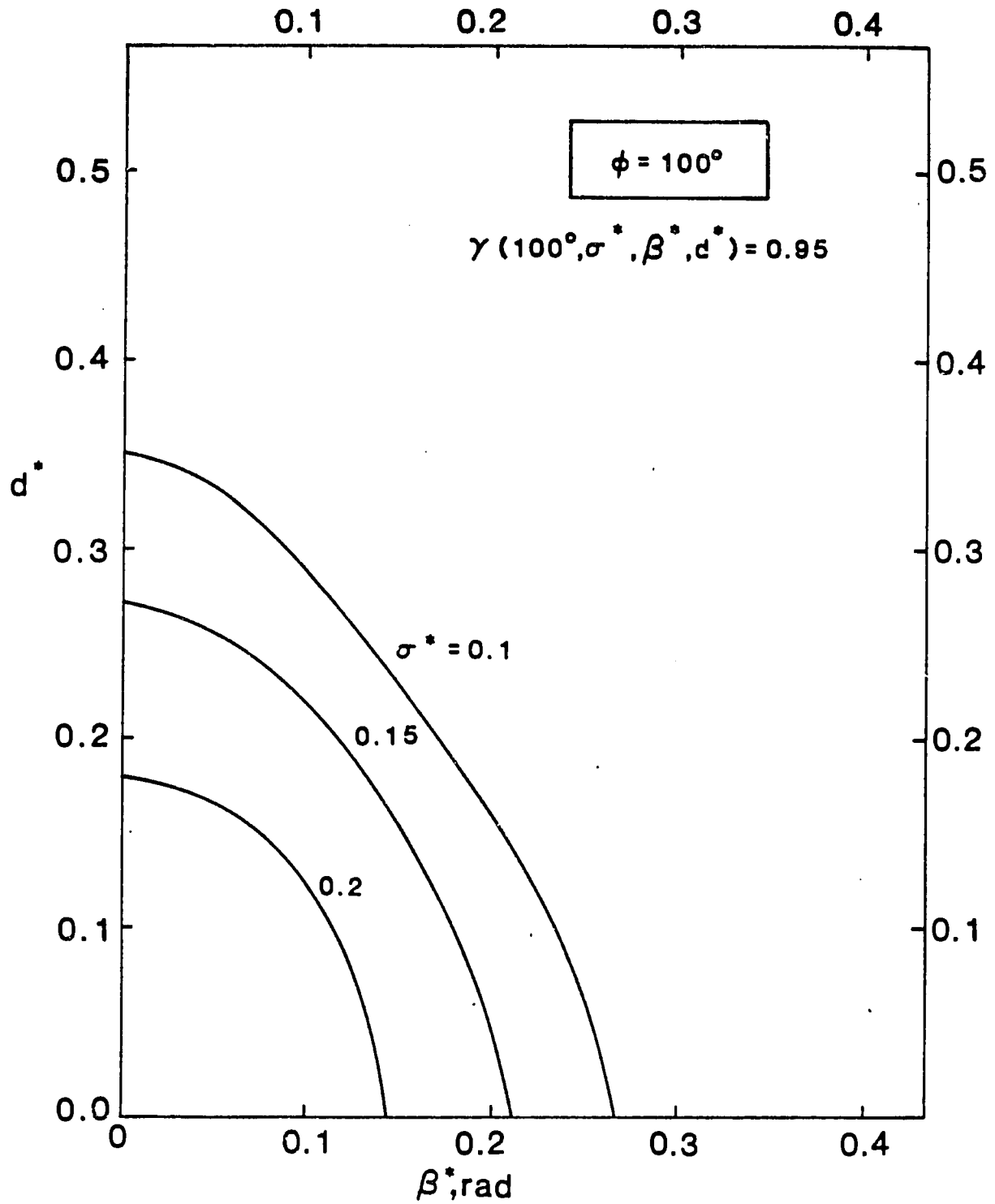


Figure 5.6 Allowable non-random error levels for $\gamma = 0.95$ and $\phi = 100^\circ$ and various random error levels.

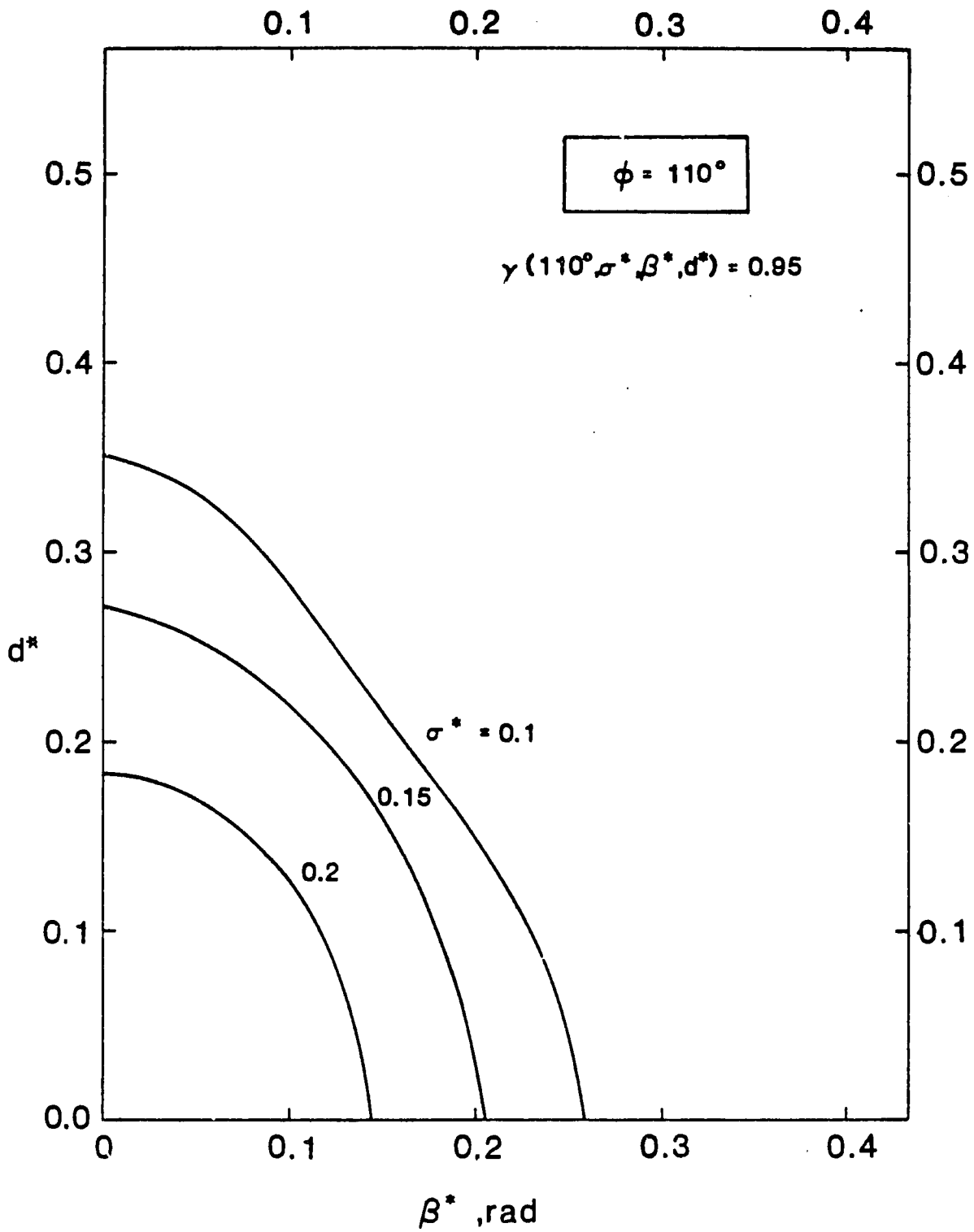


Figure 5.7 Allowable non-random error levels for $\gamma = 0.95$ and $\phi = 110^\circ$ and various random error levels.

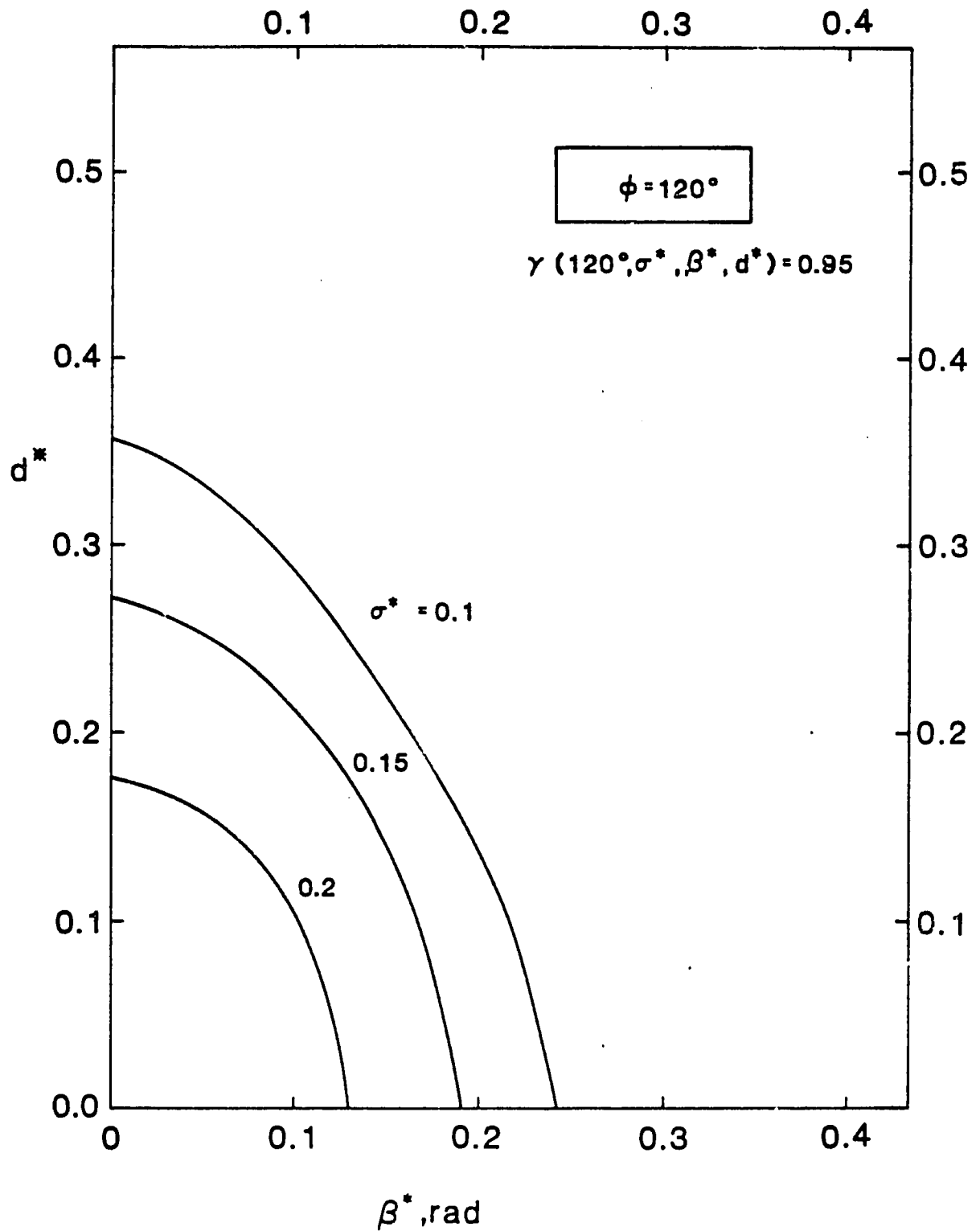


Figure 5.8 Allowable non-random error levels for $\gamma = 0.95$ and $\phi = 120^\circ$ and various random error levels.

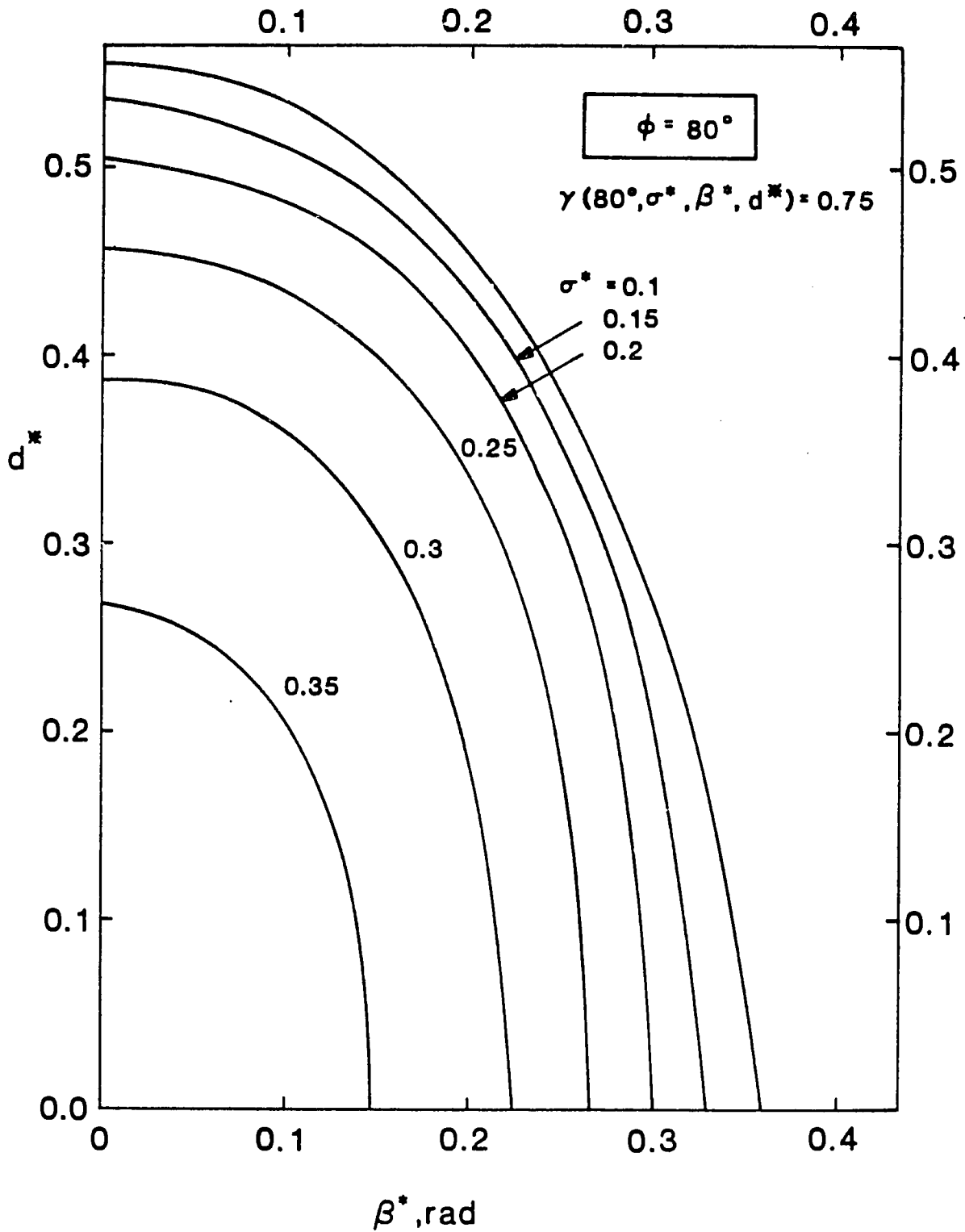


Figure 5.9 Allowable non-random error levels for $\gamma = 0.75$ and $\phi = 80^\circ$ and various random error levels.

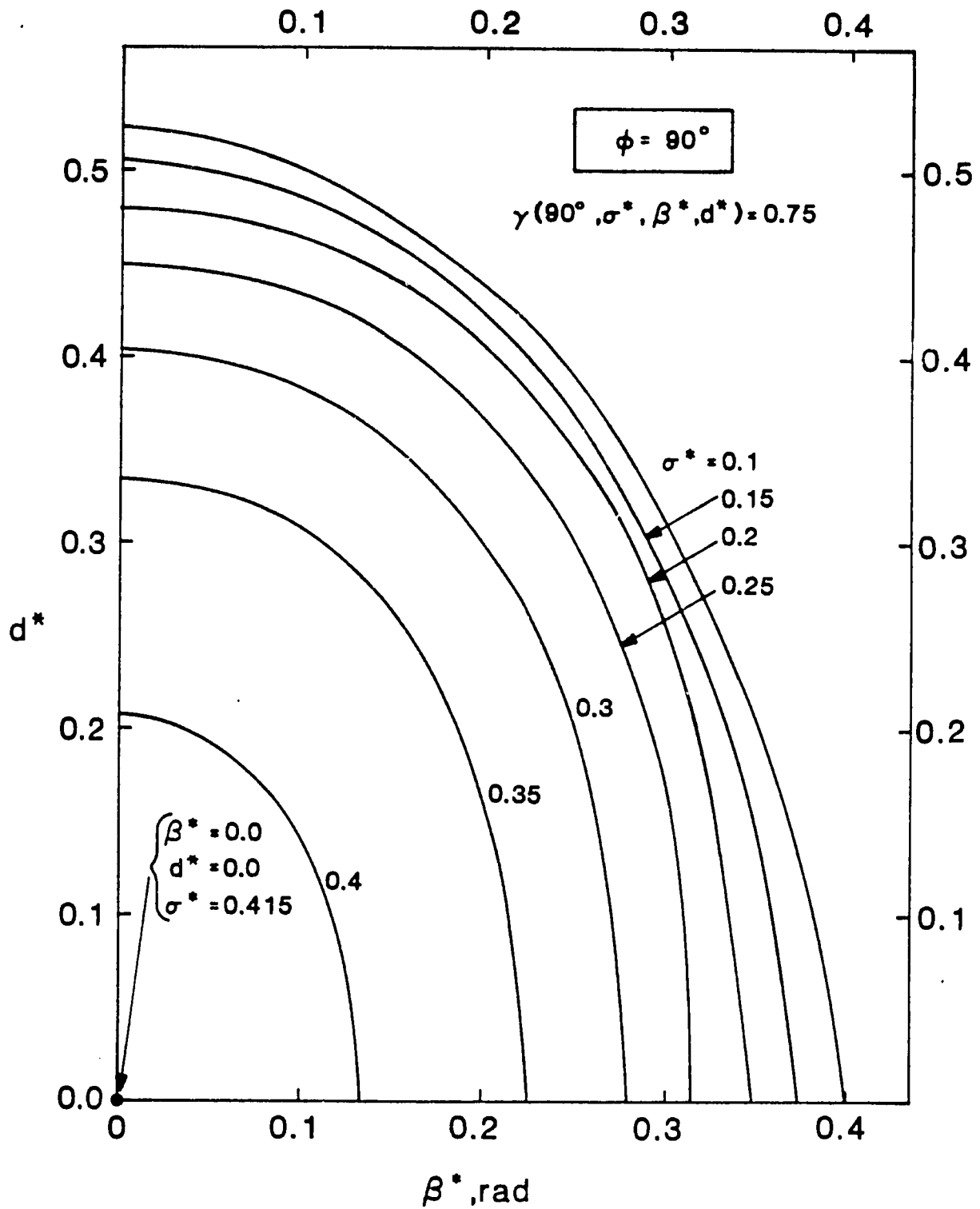


Figure 5.10 Allowable non-random error levels for $\gamma = 0.75$ and $\phi = 90^\circ$ and various random error levels.

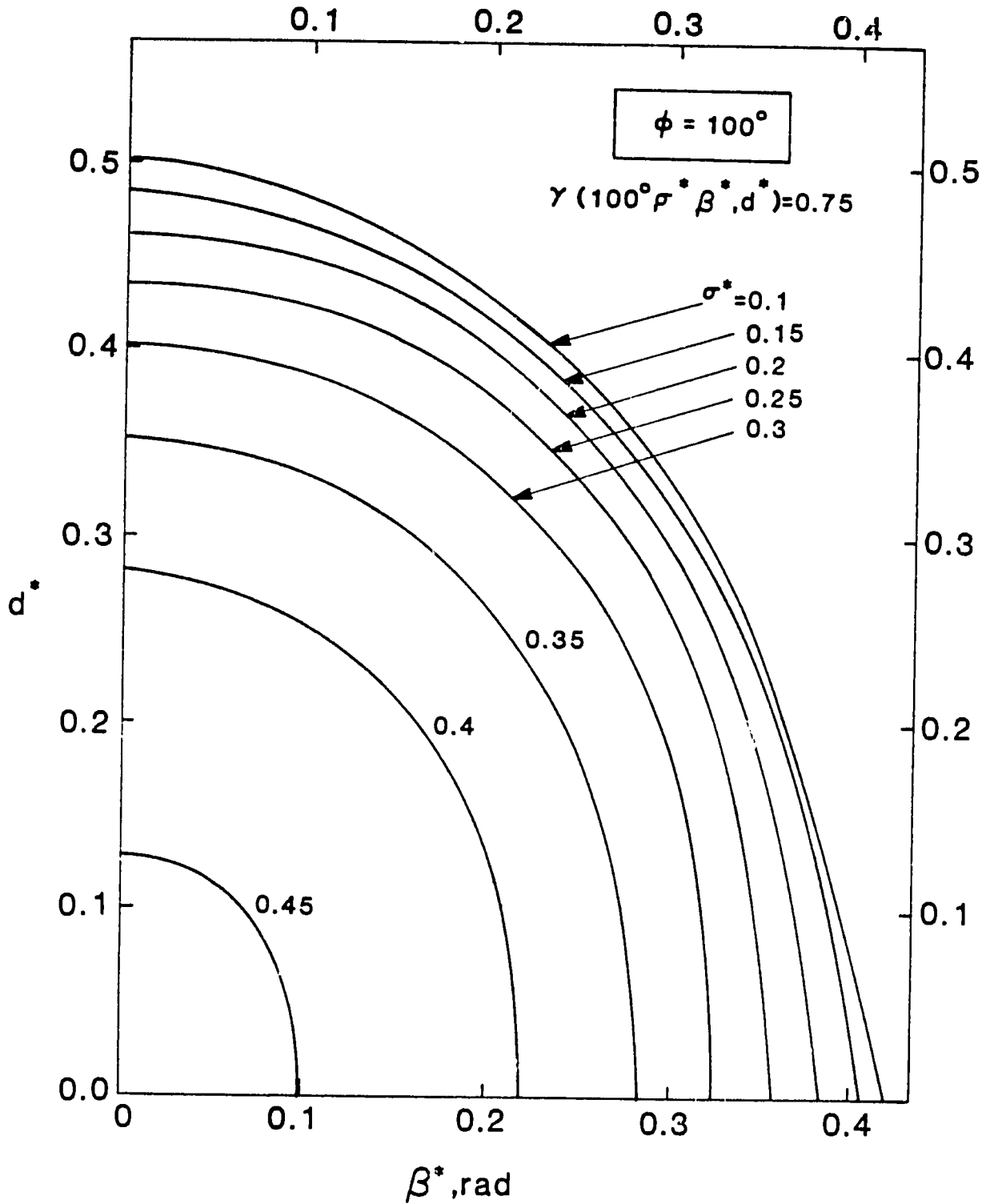


Figure 5.11 Allowable non-random error levels for $\gamma = 0.75$ and $\phi = 100^\circ$ and various random error levels.

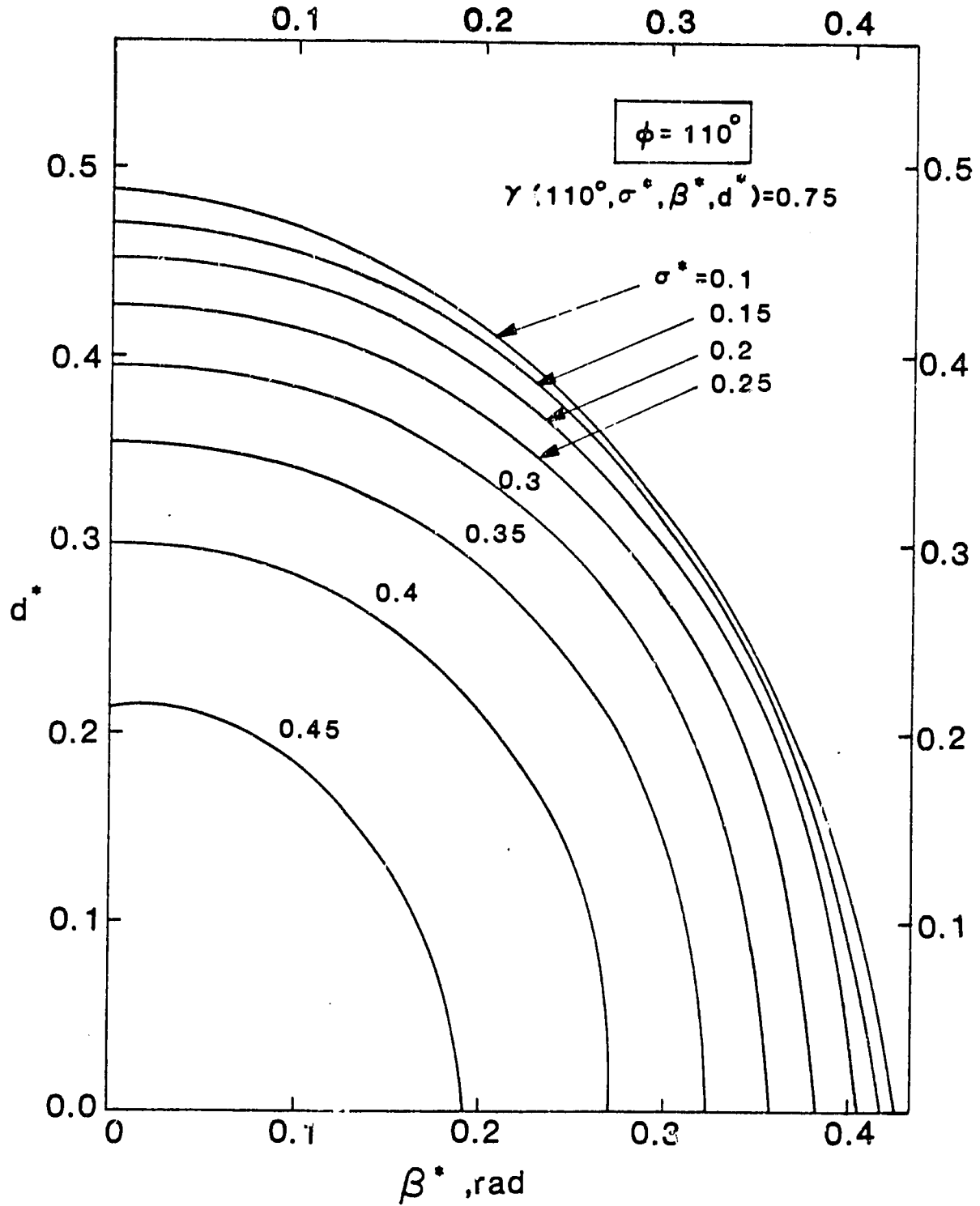


Figure 5.12 Allowable non-random error levels for $\gamma = 0.75$ and $\phi = 110^\circ$ and various random error levels.

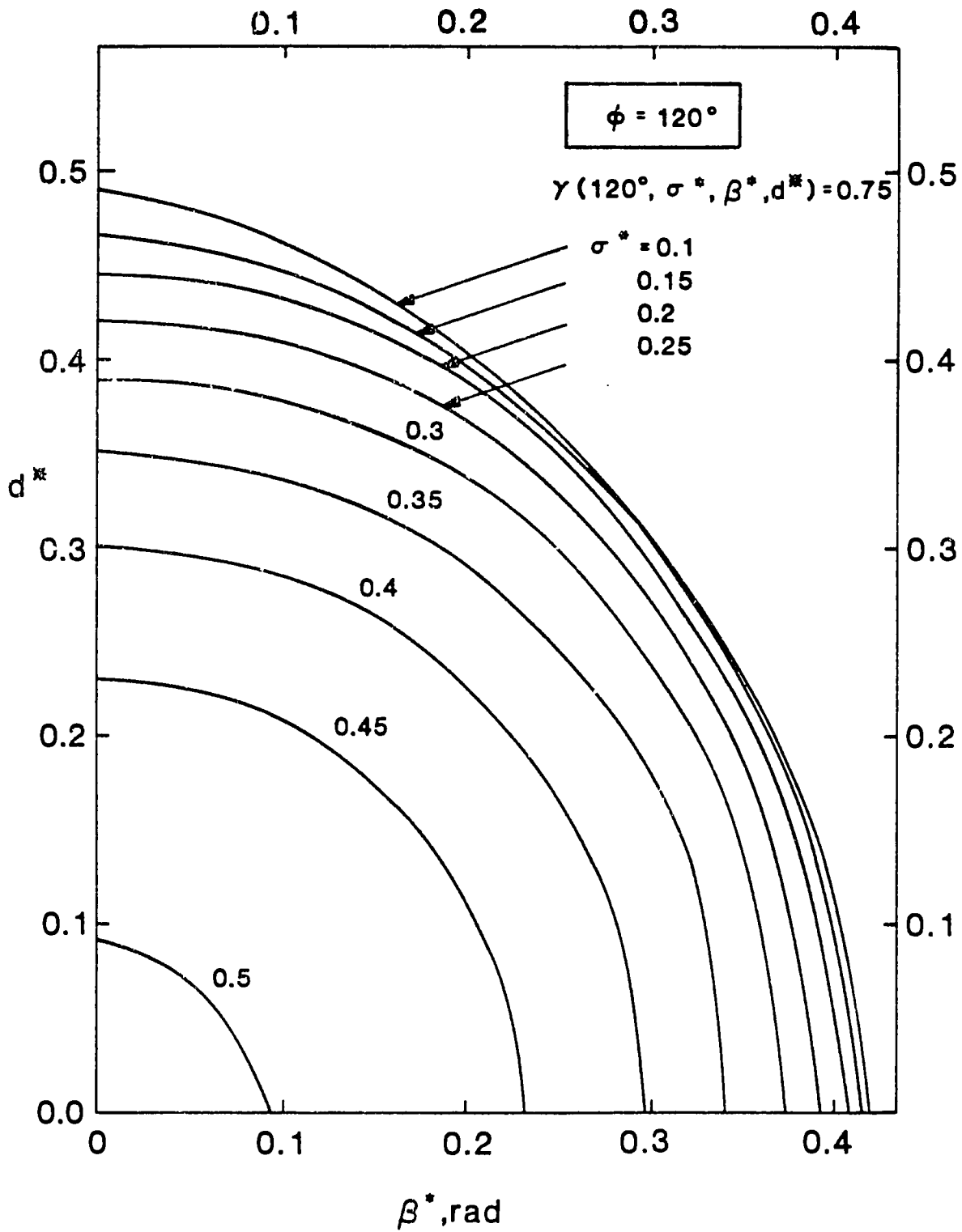


Figure 5.13 Allowable non-random error levels for $\gamma = 0.75$ and $\phi = 120^\circ$ and various random error levels.

and horizontal intercepts of the curves represent the allowable level of one non-random error (d^* or β^*) when the other (β^* or d^*) is zero. The curves themselves (solid lines) show the allowable levels of d^* and β^* (when they both are non-zero), i.e., the allowable level of receiver location and reflector misalignment errors when they exist simultaneously.

As shown in Figures 5.4 through 5.13 for a specified (or required) minimum normal-incidence factor (0.75 or 0.95), the allowable levels of non-random errors (i.e., error tolerances d^* and β^*) depend on the random error parameter σ^* and the rim angle ϕ . For example, for a given rim angle, say $\phi = 90^\circ$, and $\gamma = 0.95$:

$$\left. \begin{array}{l} d^* : 0.0 - 0.35 \\ \beta^* : 0.0 - 0.26 \text{ rad} \end{array} \right\} \quad \begin{array}{l} \text{when } \sigma^* : 0.22 - 0.1 \text{ rad.} \\ \text{(see Figure 5.5)} \end{array}$$

or for $\sigma^* = 0.15$, if $d^* \leq 0.2$, then $\beta^* \leq 0.1 \text{ rad.}$

Similarly, for $\phi = 90^\circ$ and $\gamma = 0.75$:

$$\left. \begin{array}{l} d^* : 0.0 - 0.52 \\ \beta^* : 0.0 - 0.4 \text{ rad} \end{array} \right\} \quad \begin{array}{l} \text{when } \sigma^* : 0.415 - 0.1 \text{ rad.} \\ \text{(see Figure 5.10)} \end{array}$$

In Figures 5.14, 5.15 and 5.16, for a given level of random errors, the changes in allowable level of non-random errors (error tolerances) with respect to changes in rim angle are shown. As shown in Figure 5.14, for small values of σ^* ($\sigma^* = 0.1$), the non-random error tolerance curves are not very sensitive to rim angle and the curves almost coincide

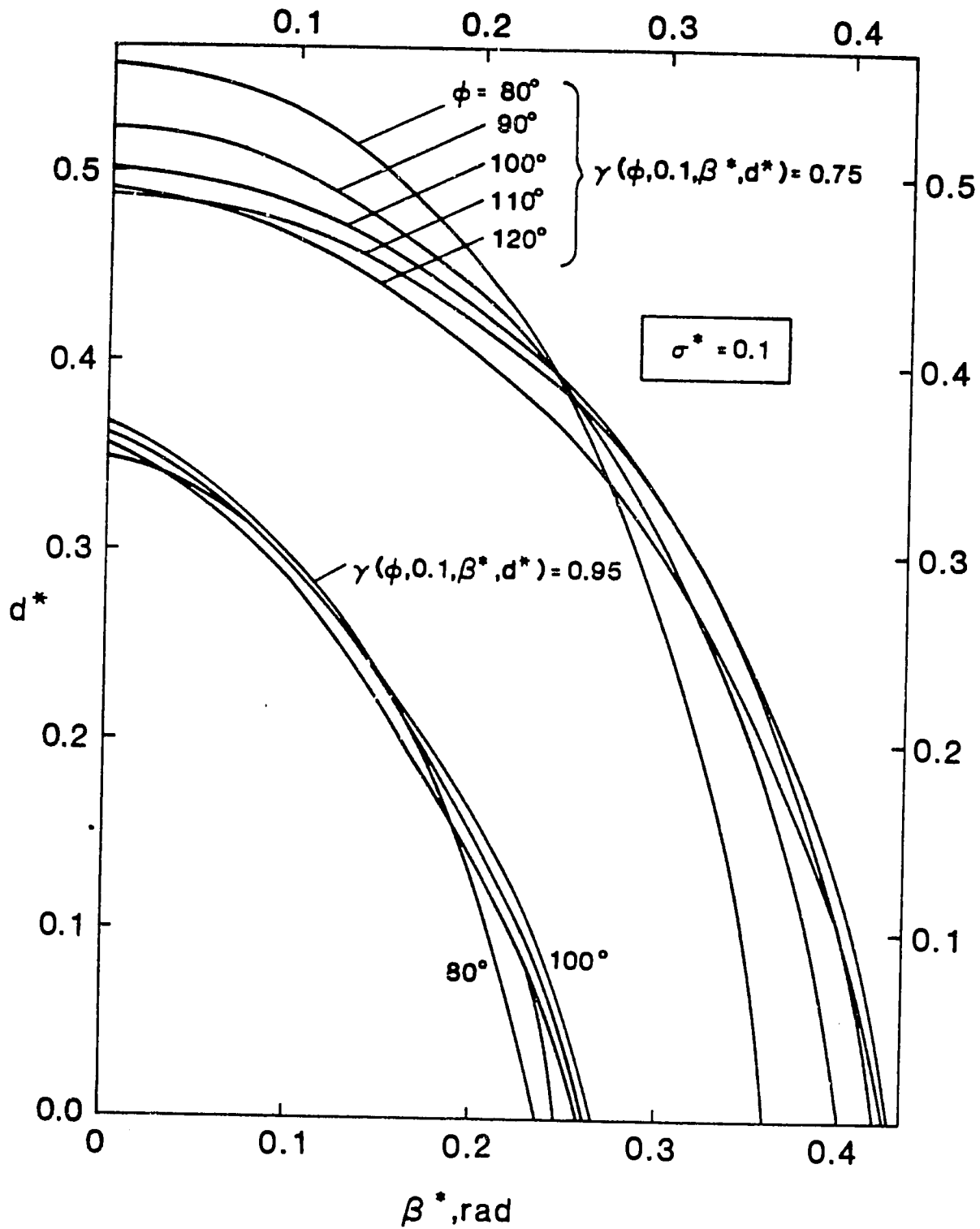


Figure 5.14 Effect of rim angle on the allowable non-random error levels for $\sigma^* = 0.1$ rad.

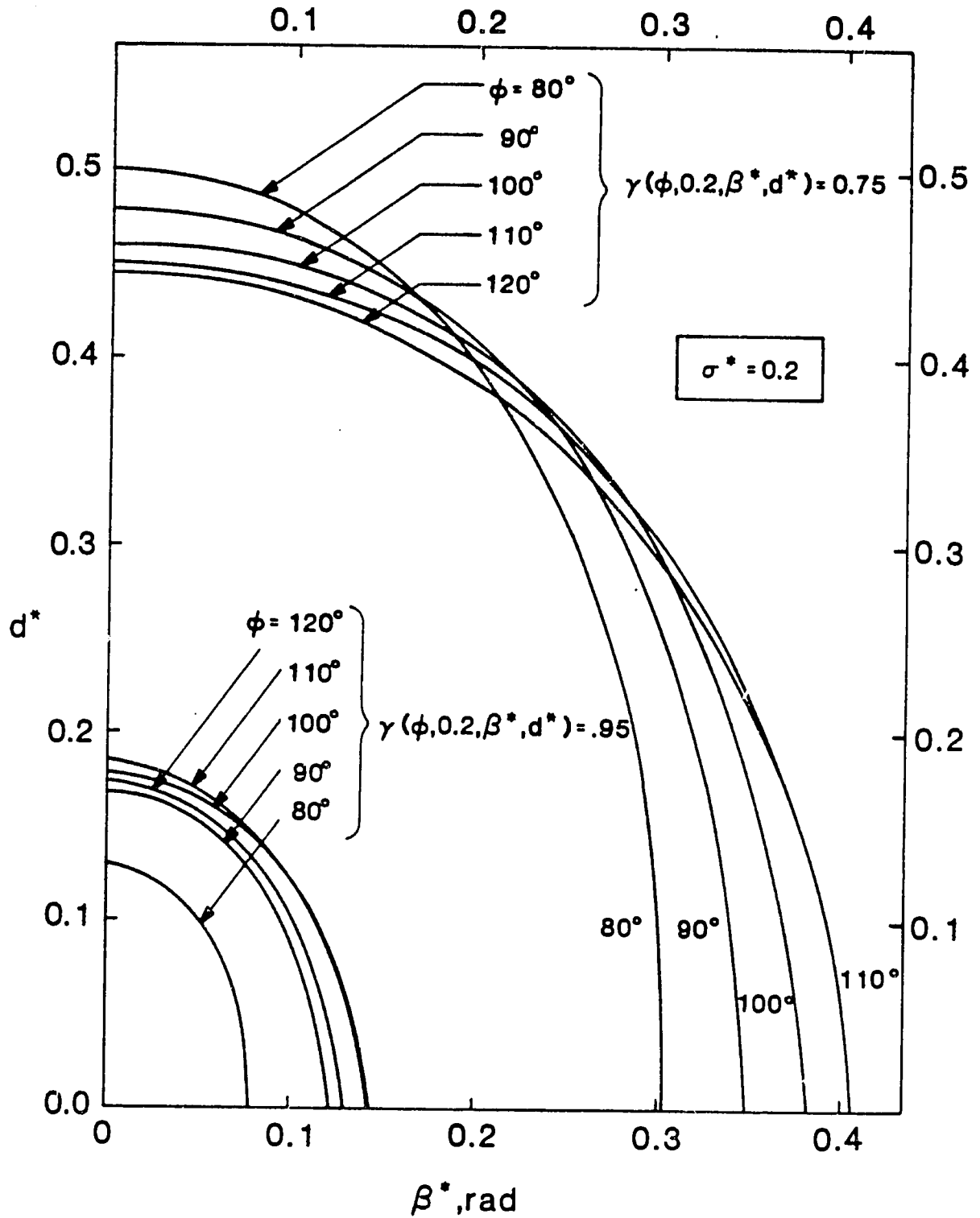


Figure 5.15 Effect of rim angle on the allowable non-random error levels for $\sigma^* = 0.2$ rad.

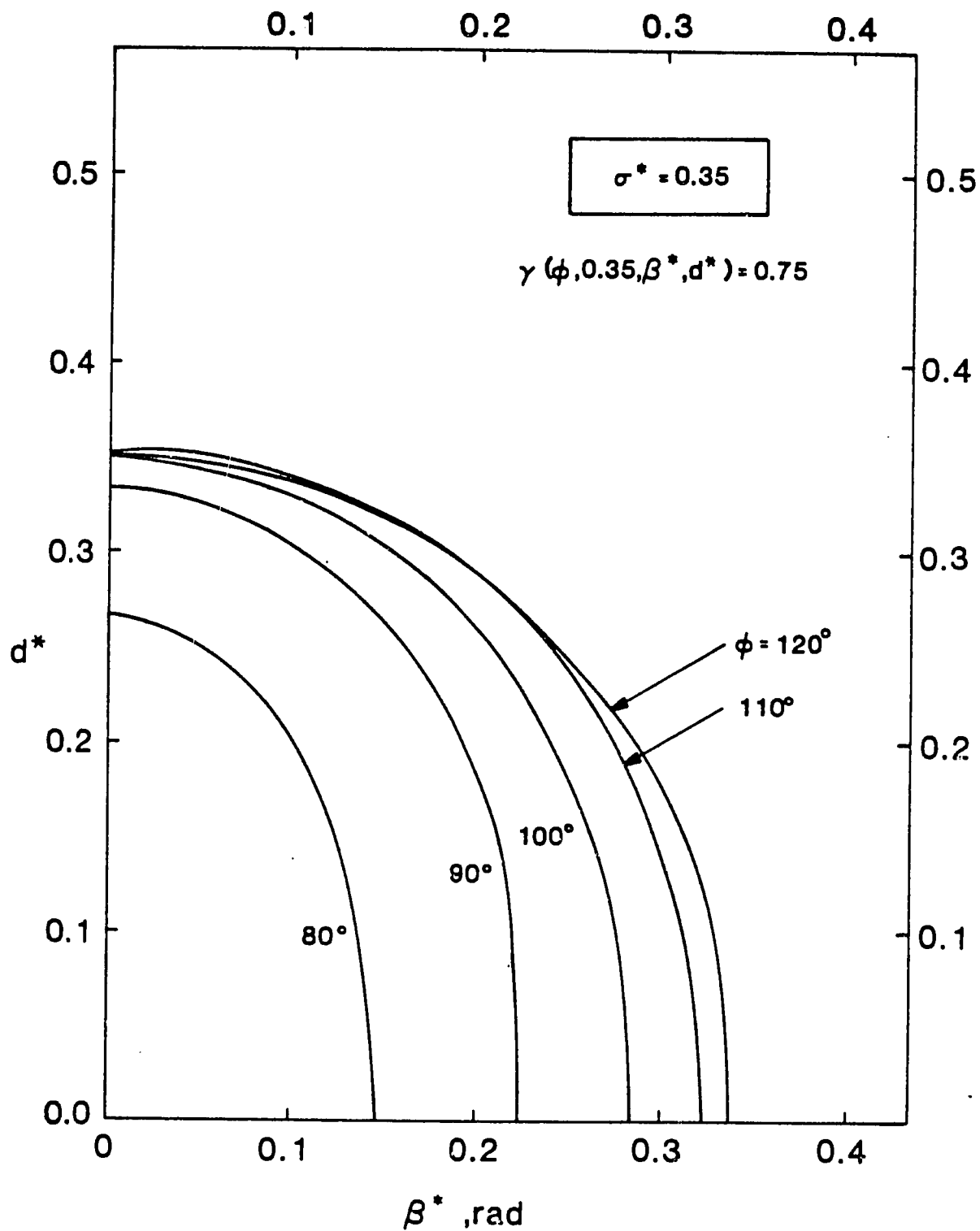


Figure 5.16 Effect of rim angle on the allowable non-random error levels for $\sigma^* = 0.35$ rad and $\gamma = 0.75$.

(this is particularly true for $\gamma = 0.95$ curves). With increasing σ^* values, the error tolerance curves start to spread out and as a result the error tolerances start to be sensitive to the rim angles. For example, the changes in allowable non-random error levels with respect to changes in rim angle are very evident in Figures 5.15 ($\gamma = 0.95$, $\sigma^* = 0.2$) and 5.16 ($\gamma = 0.75$, $\sigma^* = 0.35$). Therefore, one can conclude that the range of optimal rim angles (which was found to be between $80^\circ - 120^\circ$ for zero non-random errors) would be different in the presence of both random and non-random errors. In the following section, the sensitivity of allowable level of non-random errors to changes in rim angle is considered, and the optimal range of rim angles in the presence of both random and non-random errors is found.

5.4 Sensitivity of Error Tolerances to Changes in Rim Angle -- Optimal Rim Angles

In Figures 5.17, 5.18 and 5.19, sensitivity of allowable non-random error levels (d^* and β^*) is shown for a given random error level (σ^*) and for specified (or required) minimum intercept factors ($\gamma = 0.95$ and $\gamma = 0.75$). The locus of optimal rim angles for $\gamma > 0.75$ are in the range of:

80°- 120° for	$\sigma^* = 0.2$ rad.,
95°- 120° for	$\sigma^* = 0.3$ rad.,
105°- 120° for	$\sigma^* = 0.4$ rad.,

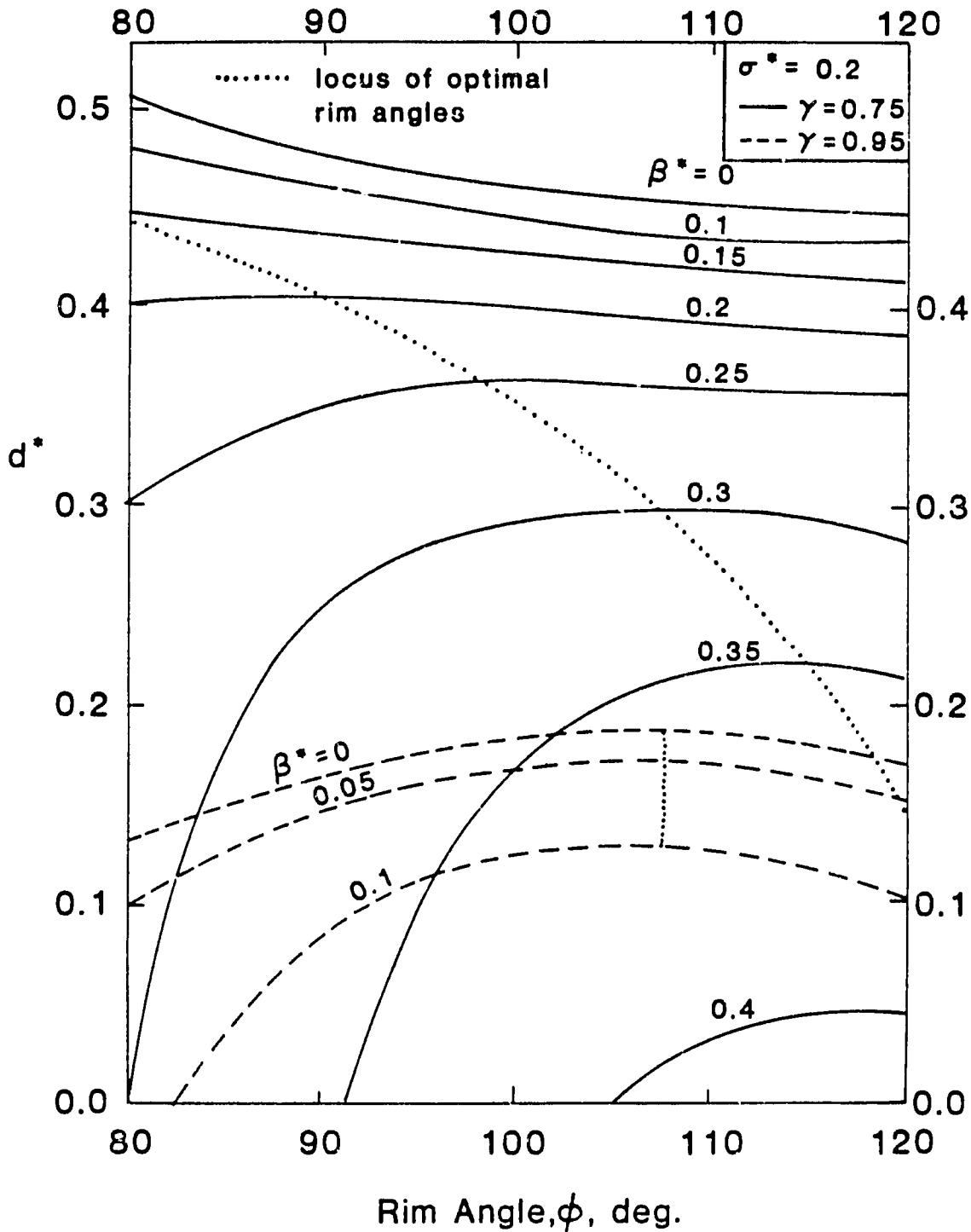


Figure 5.17 Allowable non-random error level d^* as a function of rim angle and β^* for $\sigma^* = 0.2$ and for $\gamma = 0.95$ and 0.75 .

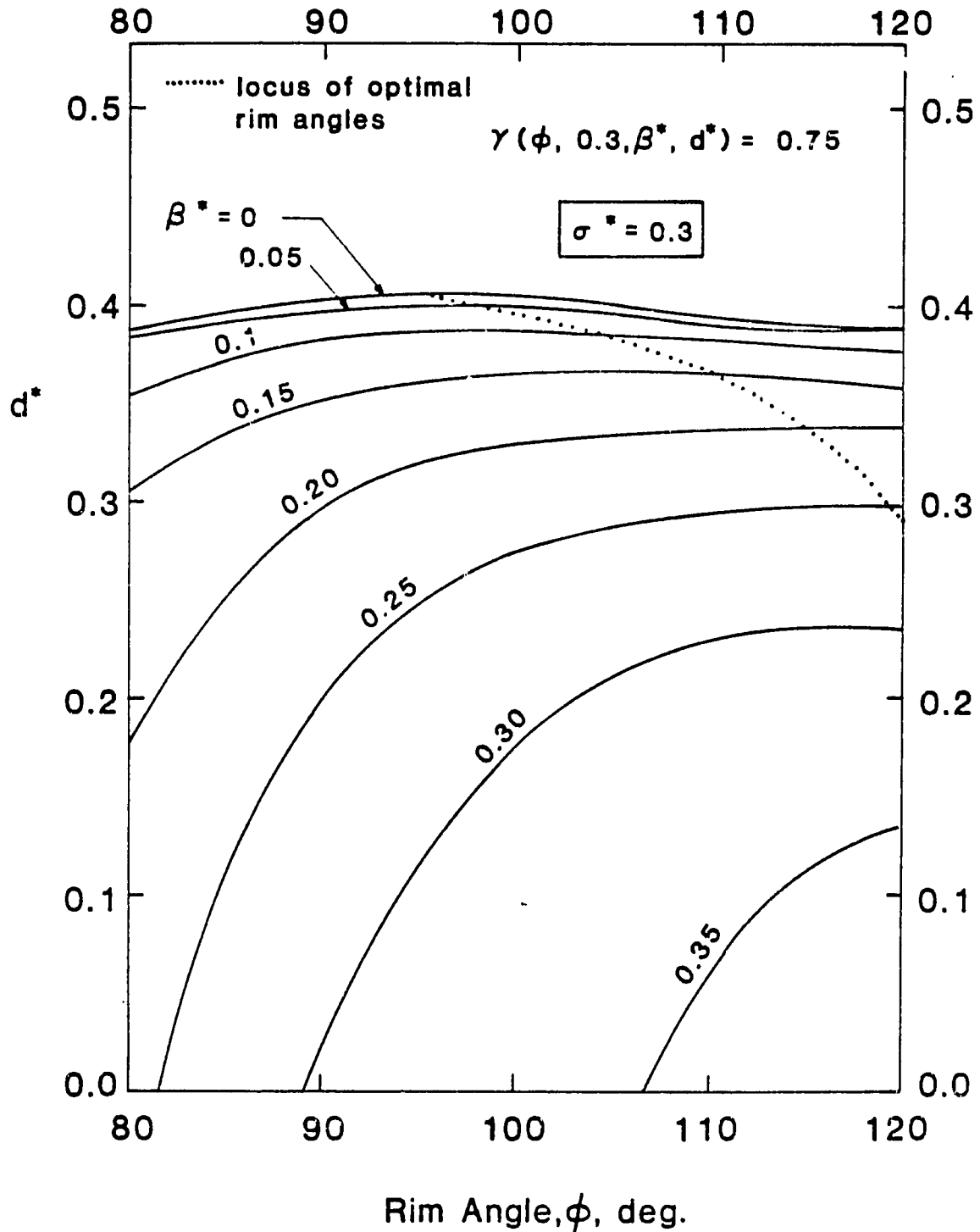


Figure 5.18 Allowable non-random error level d^* as a function of rim angle and β^* for $\sigma^* = 0.3$ and $\gamma = 0.75$.

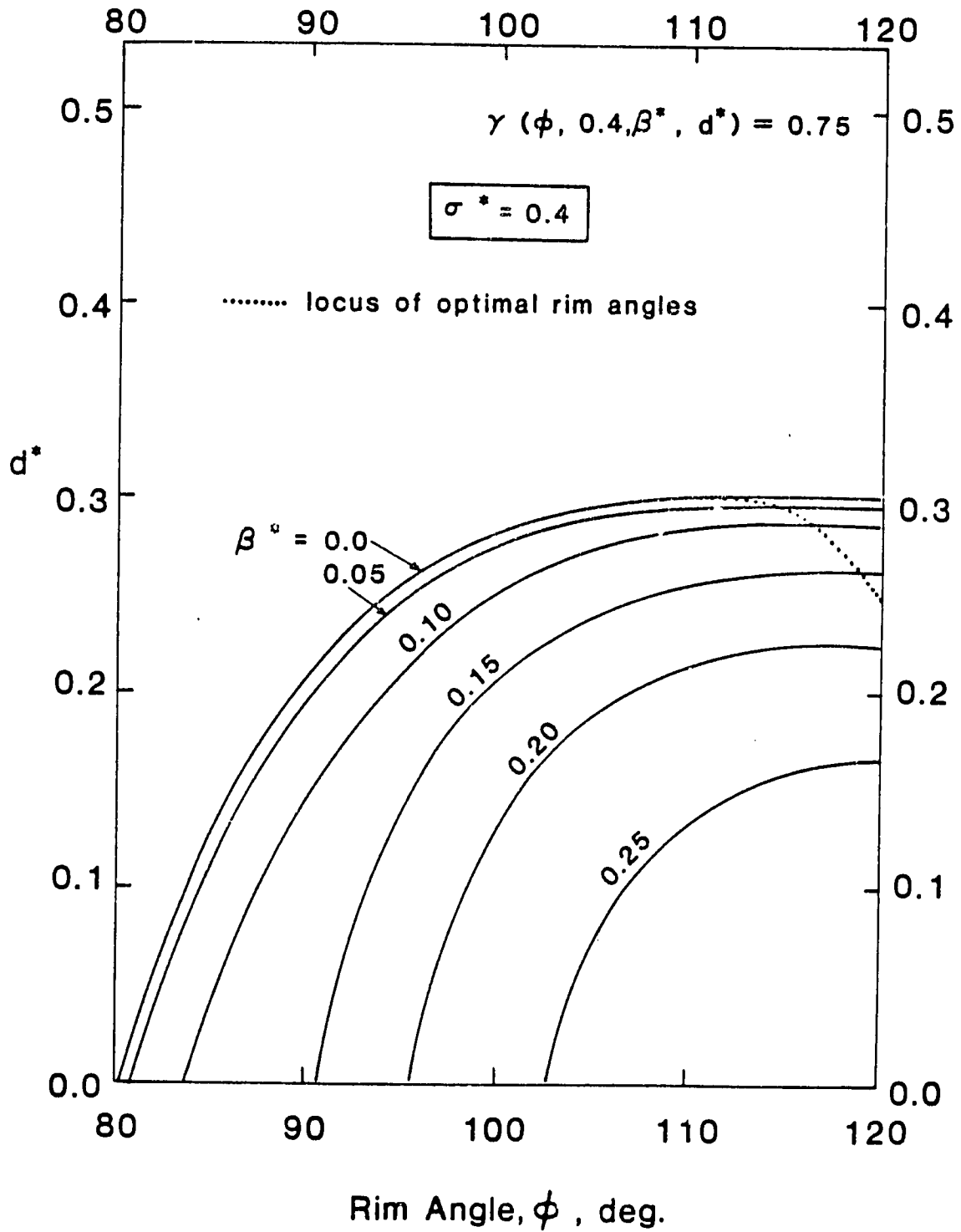


Figure 5.19 Allowable non-random error level d^* as a function of rim angle and β^* for $\sigma^* = 0.4$ and $\gamma = 0.75$

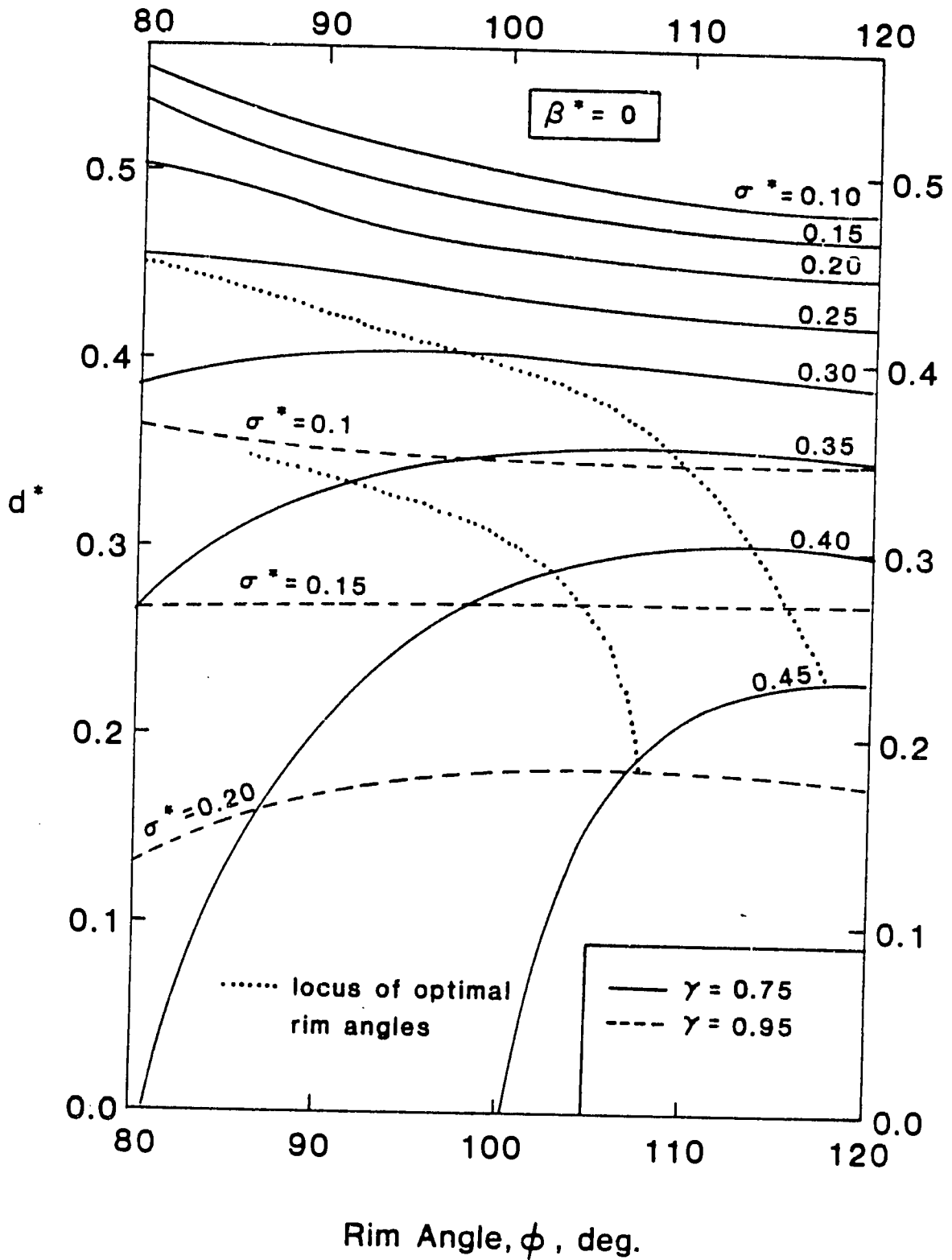


Figure 5.20 Allowable random error level d^* as a function of rim angle and σ^* for $\beta^* = 0.0$ and $\gamma = 0.95$ and 0.75 .

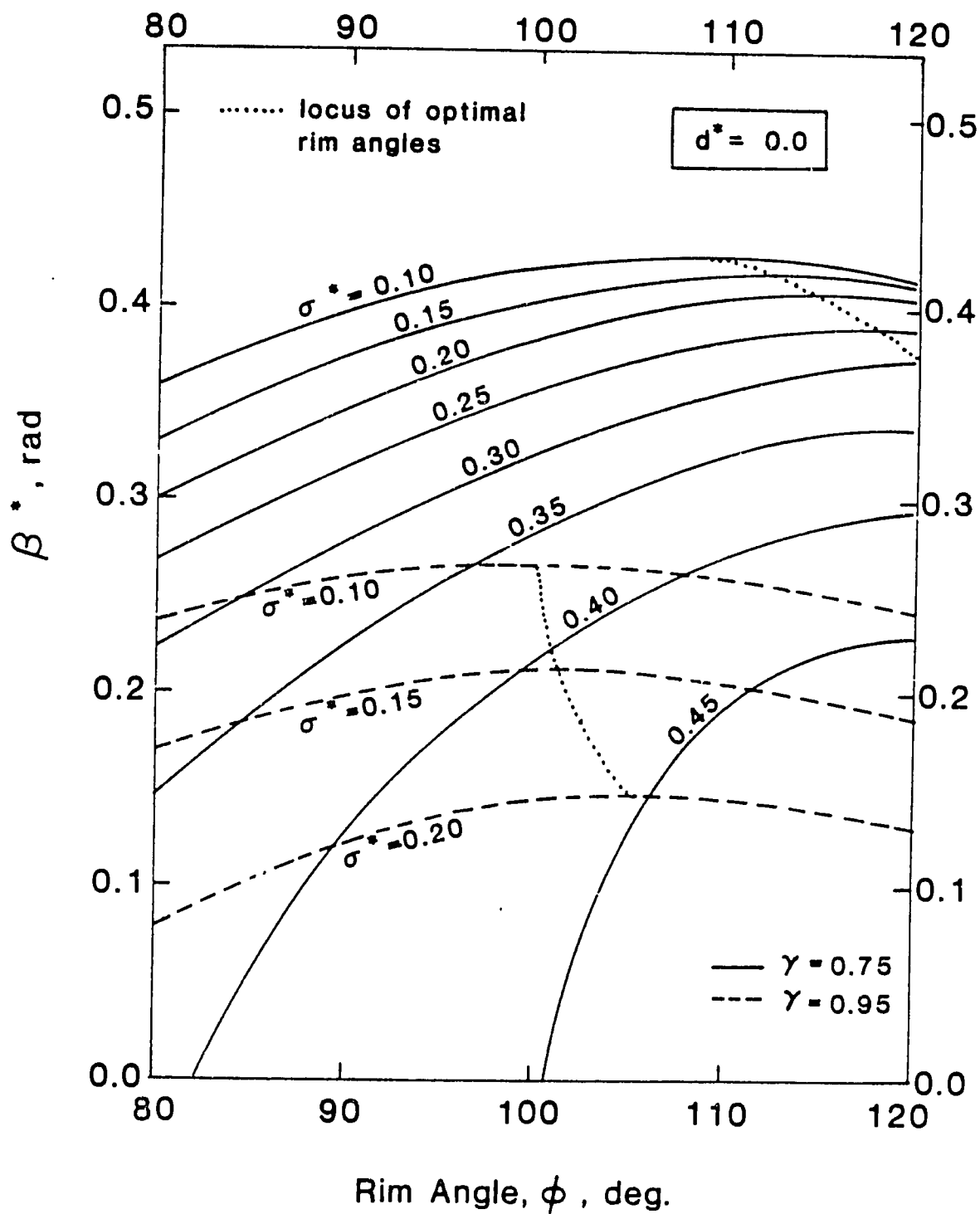


Figure 5.21 Allowable non-random error level β^* as a function of rim angle and σ^* for $d^* = 0.0$ and $\gamma = 0.95$ and 0.75 .

In Figure 5.20, optimal rim angles are shown for zero angular non-random errors (i.e., $\beta^* = 0.0$). These are in the range of 80° - 120° for an intercept factor greater than 0.75. In Figure 5.21 optimal rim angles for zero mislocation non-random errors (i.e., $d^* = 0.0$) are shown. In this case, optimal rim angles are in the range of 100° - 120° . As a result, one can conclude that the optimum rim angle based on random and non-random errors together is in the range of 105° - 120° .

5.5 Summary

In this chapter the results of the optical analysis obtained by using the comprehensive optical model and universal error parameters are presented.

The results of the optical analysis with random errors alone were presented first. These results were compared with those of the previous investigators and they were found to compare favorably. The optimum rim angle based on random errors alone was found to be broad (in the range of 80° to 120°). The optical performance of the trough was, however, found to be sensitive to both random and non-random errors. The optimum rim angle based on both random and non-random errors was found to be in the range of 105° - 120° .

It was concluded that the optical model developed in Chapter Three is a comprehensive model which can be used in a comprehensive design method. Furthermore, it is shown that the

optical model developed here will enable a designer to incorporate error tolerances into the trough design at the preliminary stage of the design process. (The concept of error tolerances is particularly useful in design of PTC's in developing countries.) The use of the developed optical model will be presented in the second technical report. The following chapter presents models for the thermal analysis of PTC's.

Chapter Six

THERMAL ANALYSIS OF PARABOLIC TROUGH COLLECTORS

6.1 Introduction

As indicated earlier, the primary function of the receiver subsystem of the PTC's is to absorb and transfer the concentrated energy to the fluid flowing through it. In the process, however, the absorbing surface of the receiver will be heated, and its temperature will become considerably higher than that of the surroundings. For example, depending on the temperature requirements of the application, operating temperatures as high as 600°F can be attained at the absorbing surface of the receiver during operation. Subsequently, the temperature difference between the absorbing surface and the surroundings will cause some of the collected energy to be transferred back to the surroundings (i.e., lost).

Proper quantification of the heat loss from the receiver is important for predicting the performance and hence designing PTC's. In this chapter, first, description of the problem and assumptions made for the analysis are presented. Then, models and empirical equations are presented for calculating the heat transfer coefficients between different components of the receiver subsystem. Finally, a method for calculating a single heat loss parameter, q_L , in W per m² of receiver surface area to characterize the thermal behavior

of the receiver is presented.

6.2 Description of the Problem and Assumptions

The cross-section of the receiver subsystem is shown in Figure 6.1. As shown, three different heat exchanges exist among the components of the receiver. These are:

1. Heat transfer from the absorber tube to the working fluid.
2. Heat exchange between the absorber tube and the glass jacket (glazing).
3. Heat exchange between the glass jacket and the surroundings.

Since the collector will be optimized based on either instantaneous or all-day average efficiency, a steady-state thermal analysis of the receiver will suffice for the design studies. In Figure 6.2, a two-dimensional steady-state energy exchange with the working fluid is shown. The working fluid will be heated as it travels through the fluid duct. Therefore, the value of the outlet temperature, $T_{f_{out}}$, will be a function of the inlet temperature ($T_{f_{in}}$), flow rate (\dot{m}), working fluid properties, length of the collector module (L), thickness and conductivity of the absorber tube and the absorber tube temperature, which will be a function of x , i.e., $T_{abs} = T_{abs}(x)$. For a known heat flux along the absorber tube axis and for given inlet and ambient conditions, and collector parameters (i.e., for given $T_{f_{in}}$, \dot{m} , T_a , L , etc.), one can solve for

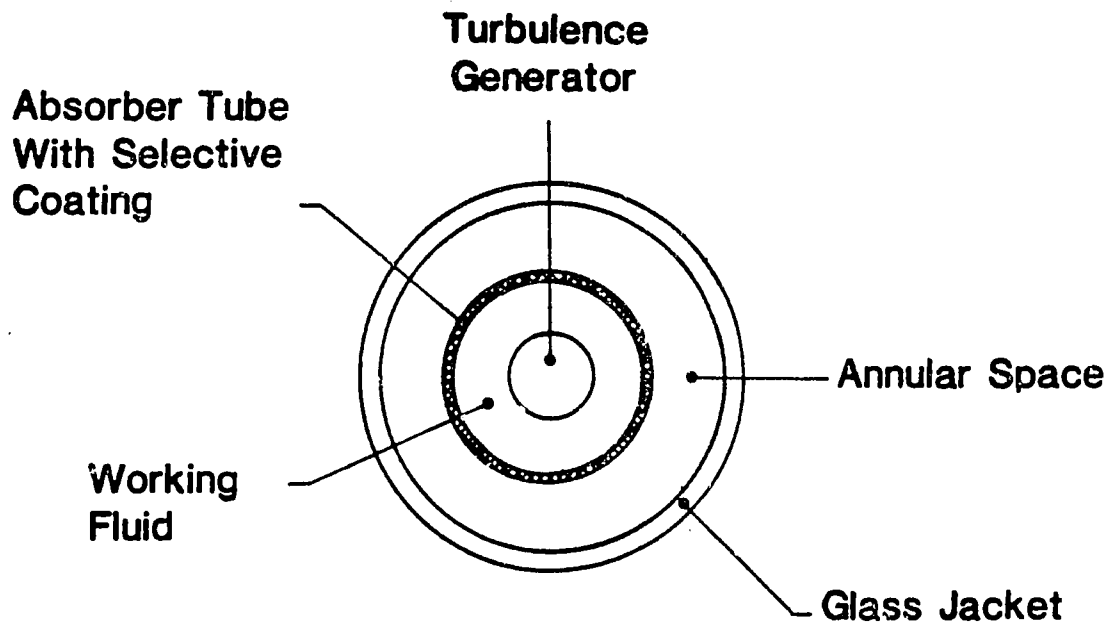


Figure 6.1 Cross section of receiver subsystem.

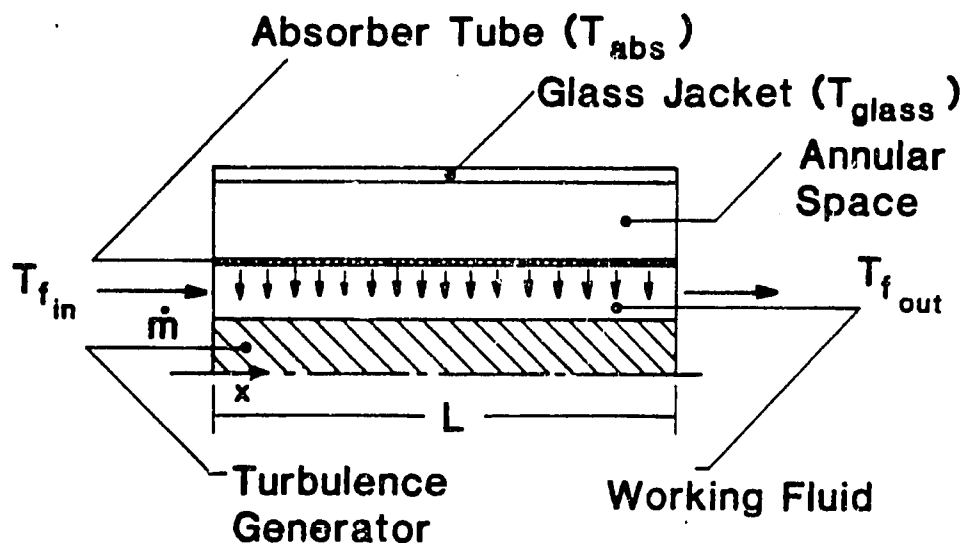


Figure 6.2 Two-dimensional energy exchange to the working fluid [35].

T_{fout} , $T_{abs}(x)$ and $T_{glass}(x)$ by setting up three energy balance equations [35]. Then the total heat loss from the collector module can be calculated by using:

$$q_{0-L} = \int_0^L U_{loss}(x)(T_{glass}(x) - T_a) dx \quad (6.1)$$

where $U_{loss}(x)$ is the heat transfer coefficient for combined convection (wind induced) and radiation heat losses from the outer surface of the glass jacket. However, this is a very cumbersome method which requires numerous iterations and more importantly, it requires a prior knowledge of the collector parameters which are not known in the present case. (The objective of the present study is to optimize the collector parameters!) Therefore, further approximations are needed.

Since at the preliminary stage of design only an average value of the heat loss per unit length of receiver will suffice, it will be appropriate to assume a known average absorber tube temperature ($T_{abs} = \text{constant}$). The heat loss can be related to this average absorber tube temperature, and the heat loss coefficients for different modes of heat transfer can be determined as a function of the average absorber tube temperature [36]. As a result, this will eliminate the need to specify the fluid inlet and outlet temperature, flow rate, fluid properties and collector parameters and, more importantly, it will allow for the use of a one-dimen-

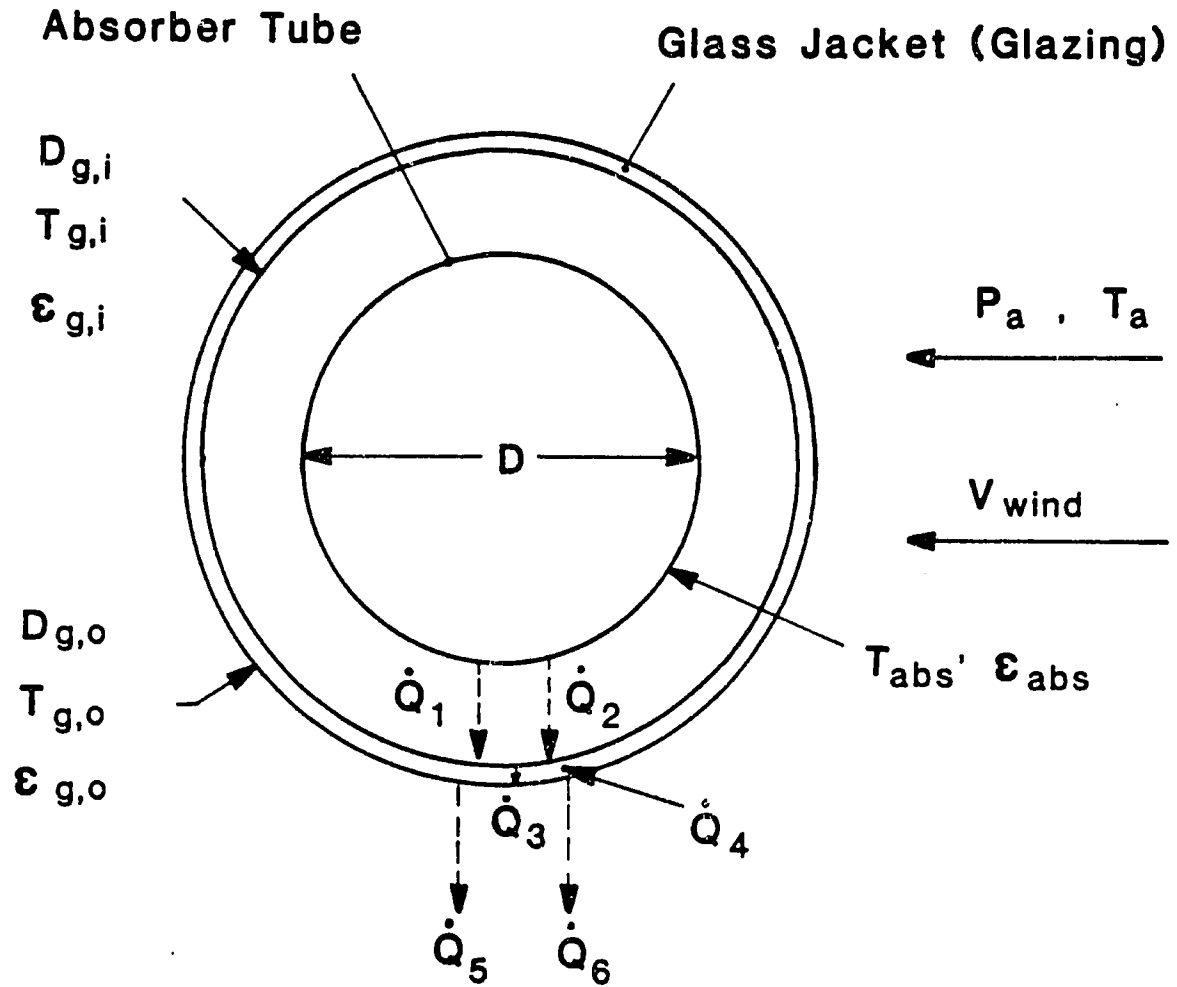
sional heat transfer model (radial). Therefore, the following assumptions can be made to facilitate the analysis of the thermal behavior of the receiver:

1. The problem is one dimensional in the radial direction,
2. Steady-state conditions hold,
3. The absorber tube and the glass jacket are concentric,
4. The surfaces are gray, diffuse emitters and absorbers in thermal radiative energy exchange,
5. The annulus is assumed to be either non-evacuated (at atmospheric pressure), partially evacuated, or back filled with heavy gases,
6. The annulus gas properties are functions of the temperature and pressure only,
7. The properties of air (surroundings), glass and selective coating are computed as a function of their temperature,
8. The surroundings acts as a blackbody at a reduced temperature T_{sink} ($T_{\text{sink}} \approx (T_a - 6)\text{K}$).

In the following section, the development of the one-dimensional heat-loss model (using the above assumptions) is presented.

6.3 One-Dimensional Heat-Loss Model

The one-dimensional receiver heat-loss model is shown in Figure 6.3. This is the model used in the literature most often (e.g., [35, 36]) for the calculation of the heat-loss from the receiver. In this model, heat balance equations can be set-up at the inner and outer surface of the glazing as



\dot{Q}_1 = Radiative heat-loss rate from tube to glazing,

\dot{Q}_2 = Conductive/convective heat-loss rate from absorber tube to glazing,

\dot{Q}_3 = Conductive heat-loss rate through glazing,

\dot{Q}_4 = Rate of heat input into glazing due to solar absorptance of glass,

\dot{Q}_5 = Convective heat-loss rate from glazing to surroundings,

\dot{Q}_6 = Radiative heat-loss rate from glazing to surroundings.

Figure 6.3 One-dimensional receiver heat-loss model.

follows:

$$\text{Inner surface:} \quad \dot{Q}_1 + \dot{Q}_2 = \dot{Q}_3 \quad (6.2)$$

$$\text{Outer surface:} \quad \dot{Q}_3 + \dot{Q}_4 = \dot{Q}_5 + \dot{Q}_6 \quad (6.3)$$

The heat-loss rate from the absorber tube, \dot{Q}_{Loss} , is then equal to:

$$\dot{Q}_{\text{Loss}} = \dot{Q}_5 + \dot{Q}_6 \quad (6.4)$$

\dot{Q}_{Loss} can be obtained by iterative solution of the Equations (6.2) and (6.3), after all the heat-loss rates in Equations (6.2) and (6.3) are modeled. Modeling of the heat-loss rates is described in detail below per unit length of receiver:

Radiative heat-loss rate from absorber tube to glazing, \dot{Q}_1 :

The radiation heat-loss rate across the annulus can be calculated by the usual radiation exchange equation between two concentric cylinders (e.g., see [37]):

$$\frac{\dot{Q}_1}{L} = \frac{\pi D \sigma (T_{\text{abs}}^4 - T_{\text{g,i}}^4)}{\frac{1}{\epsilon_{\text{abs}}} + \frac{D}{D_{\text{g,i}}} \frac{1}{\epsilon_{\text{g,i}}} - 1} \quad (6.5)$$

Conductive/Convective heat-loss rate from absorber tube to glazing, \dot{Q}_2 :

Natural convection heat-loss in the annular space will be negligible as long as the Rayleigh number* is less than 1000 [38]. Therefore, for Rayleigh numbers less than 1000, only thermal conduction heat loss will exist in the annular space,

* See next page for the definition.

and the heat-loss can be found from:

$$\frac{\dot{Q}_2}{L} = \frac{2 \pi k_{\text{gas}}}{\ln\left(\frac{D_{g,i}}{D}\right)} (T_{\text{abs}} - T_{g,i}) \quad N_{\text{Ra}} < 1000 \quad (6.6)$$

where k_{gas} is thermal conductivity at standard conditions, evaluated at mean annulus temperature, $T_m = 0.5 (T_{\text{abs}} + T_{g,i})$.

For Rayleigh number* greater than 1000, the combined conductive and convective heat-loss rate can be evaluated from an effective conduction coefficient [38], k_{ef} , which can be obtained from experimental results reported in literature (e.g., [39, 40]). The classical experimental results of Kraussold have been correlated and used by many investigators. This correlation for k_{ef} is given here (see Eq.(6.8)).

$$\frac{\dot{Q}_2}{L} = \frac{2 \pi k_{\text{ef}}}{\ln\left(\frac{D_{g,i}}{D}\right)} (T_{\text{abs}} - T_{g,i}) \quad (6.7)$$

where

$$k_{\text{ef}} = 0.1585 k_{\text{gas}} N_{\text{Ra}}^{0.2667} \quad N_{\text{Ra}} > 1000 \quad (6.8)$$

For partially evacuated annulus, the heat-loss rate can be calculated from Eq.(6.7) by using the conductivity of the annular gas at reduced pressure (e.g., see [41]). For evacuated annulus $k_e \rightarrow 0$, therefore, $\dot{Q}_2 = 0.0$. Heat transfer

*

$$N_{\text{Ra}} = \text{Rayleigh number} = \frac{C_p \rho^2 g \beta \left(\frac{D_{g,i}}{2} - \frac{D}{2}\right)^3 (T_{g,i} - T_{\text{abs}})}{k \mu}$$

in the annular space will be discussed further in a later section.

Conductive heat-loss rate through glazing, \dot{Q}_3 :

This is given by the following equation:

$$\frac{\dot{Q}_3}{L} = \frac{2 \pi k_{\text{glass}}}{\ln \frac{D_{g,o}}{D_{g,i}}} (T_{g,i} - T_{g,o}) \quad (6.9)$$

Rate of heat input into glazing, \dot{Q}_4

This will be a function of the beam insolation, I_b :

$$\frac{\dot{Q}_4}{L} = \alpha_{\text{glass}} I_b \rho W$$

where

ρ = reflectance of the reflective surface,

W = aperture width of the reflector.

However, the sensitivity of the overall heat-loss coefficient to \dot{Q}_4 is found to be small [36]; therefore, it can be assumed constant.

Convective heat-loss rate from glazing to surroundings, \dot{Q}_5

This will be a function of the wind velocity:

$$\frac{\dot{Q}_5}{L} = \pi k_{\text{air}} \text{Nu}_{\text{wind}} (T_{g,o} - T_a) \quad (6.10)$$

where

$$\text{Nu}_{\text{wind}} = \text{wind velocity induced Nusselt number} = \frac{h_w D_{g,o}}{k_{\text{air}}}$$

The heat loss coefficient will be a function of Reynolds number and its value can be obtained using Hilpert's formulation for forced convection over cylinders [42] (cross-flow over cylinders, see Figure 6.4a). Note that all properties are evaluated at $T_m = 0.5 (T_a + T_{g,o})$.

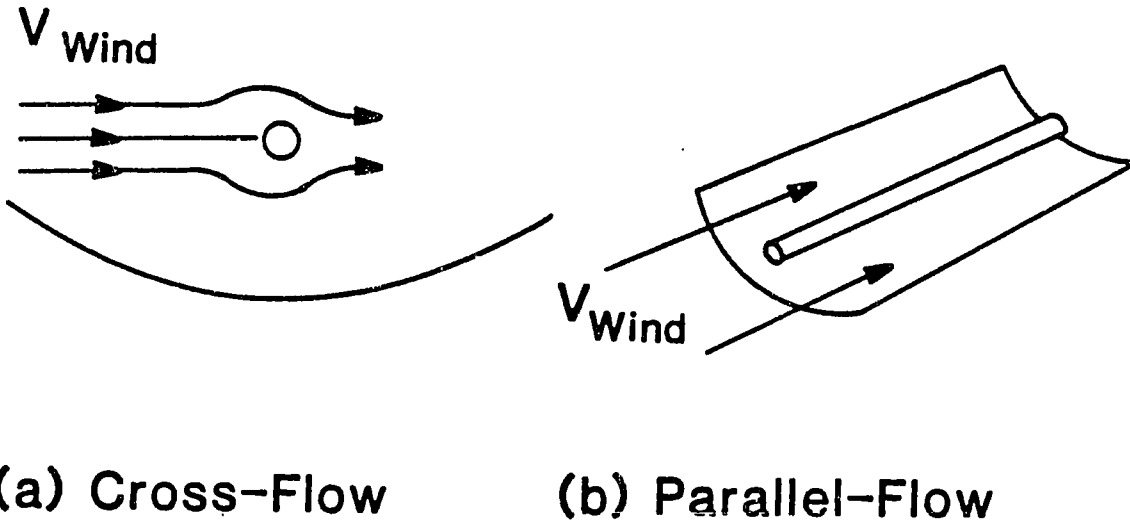


Figure 6.4 Wind induced heat-loss from receiver.

At present, there are no existing studies for calculating the heat loss rate for cylinders in parallel-flow (i.e., flow along the axis of the tube, see Figure 6.4b). Therefore only cross-flow case can be analyzed.

Radiative heat-loss rate from glazing to surroundings, \dot{Q}_6

This can be calculated from the following equation. Note that the surroundings are assumed to act as a blackbody at a reduced temperature ($T_{\text{sink}} = (T_a - 6)^\circ\text{K}$). Therefore, the heat-loss rate \dot{Q}_6 per unit receiver length is:

$$\frac{\dot{Q}_6}{L} = \epsilon_{g,o} \pi D_{g,o} \sigma (T_{g,o}^4 - T_{\text{sink}}^4) \quad (6.11)$$

where σ is the Stephan-Boltzmann constant.

6.4 Calculation of the Heat-Loss Parameter q_L

Given the receiver type (nonevacuated, evacuated, back-filled with heavy gases), and

$$T_{\text{abs}}, \epsilon_{\text{abs}}(T), \epsilon_{g,i}, \epsilon_{g,o}, D, D_{g,i}, D_{g,o}, P_a, T_a, V_{\text{wind}}, k_{\text{glass}}.$$

Equations (6.2) and (6.3) will be solved simultaneously by iteration. Initial estimates of $T_{g,o}$ and $T_{g,i}$ will be made and then corrected iteratively to obtain the unknown temperatures. Temperature-dependent convective, radiative, and fluid and gas properties will be varied also at each iteration.

Once $T_{g,o}$ is found, Equations (6.4), (6.10) and (6.11) can be used to calculate the heat-loss from the absorber tube per unit length of receiver, $\dot{Q}_{\text{loss}} / L$.

Receiver heat-loss can then be expressed as a heat-loss coefficient, U_L , that is based on absorber tube surface area. Receiver heat-loss is related to U_L by the following equation:

$$\dot{Q}_{\text{Loss}} (\text{watts}) = U_L \pi D L (T_{\text{abs}} - T_a) \quad (6.12)$$

or

$$U_L = \frac{\dot{Q}_{\text{Loss}}}{(T_{\text{abs}} - T_a) \pi D L} \quad [\text{W/m}^2_{\text{abs}} - ^\circ\text{C}] \quad (6.13)$$

and, therefore, the heat loss parameter q_L (in W per m^2 of

TABLE 6.1 REFERENCE TROUGH RECEIVER DESIGN PARAMETERS

Parameter	Value
$\epsilon_{g,i} , \epsilon_{g,o}$	0.90
α	0.95
ϵ_{abs} (Black-chrome)	0.15(100°C), 0.25(300°C)*

*Black-chrome emittance assumed linear between and beyond these limits.

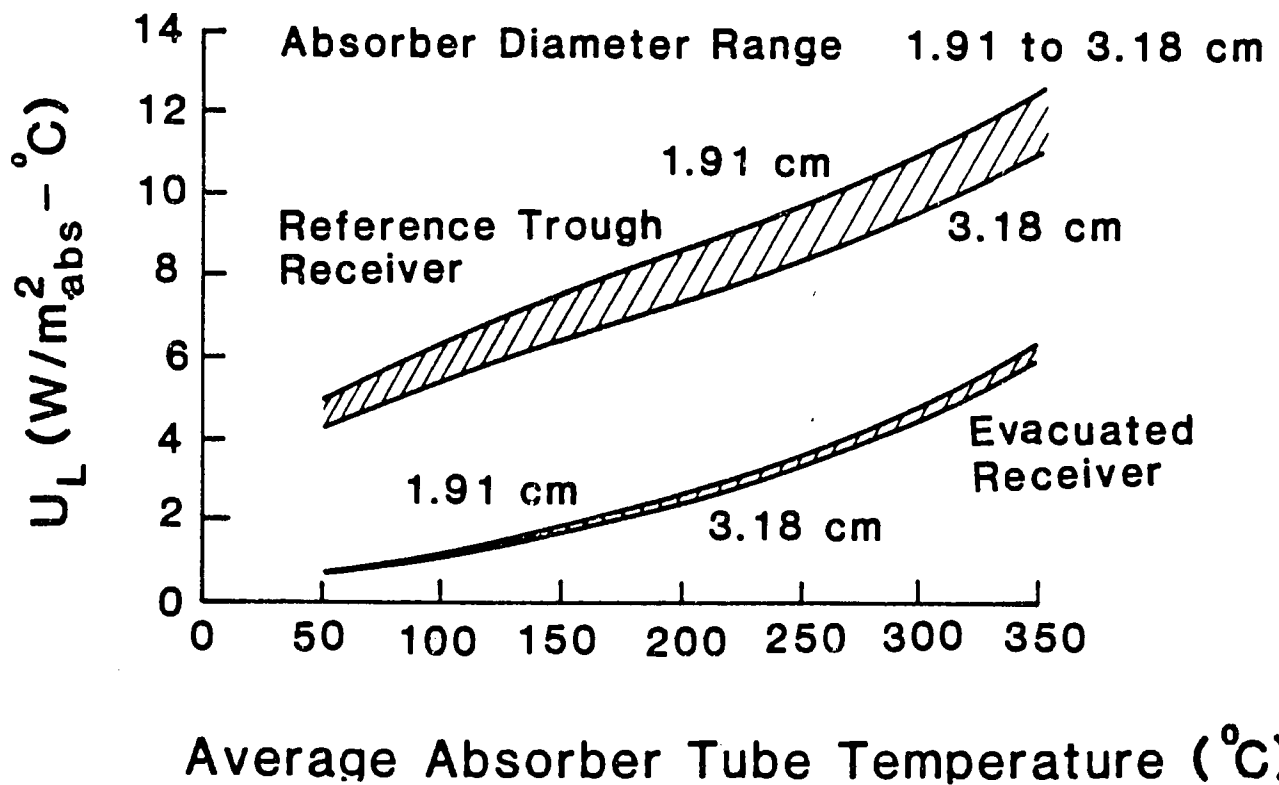


Figure 6.5 Heat-loss coefficient U_L as a function of average absorber tube temperature and absorber tube diameter (from Reference 36).

receiver surface area) can be written as:

$$q_L = \frac{\dot{Q}_{Loss}}{\pi D \ell} = U_L (T_{abs} - T_a) \quad (6.14)$$

For example, Gee et. al. [36] have calculated the heat -loss coefficient, U_L as a function of average absorber tube temperature and absorber tube diameter for a "reference" receiver and an evacuated receiver (Figure 6.5) using such a procedure. The reference receiver parameters are given in Table 6.1. In this example, the annular gap is assumed to be sized such as to keep Rayleigh number in the range 0 - 1000. A wind velocity of 2 m/s (4.5 mph) over the receiver is assumed as representative of average wind conditions. A yearly average ambient temperature of 10°C is assumed. Curves similar to the ones shown in Figure 6.5 can be obtained for other receiver design parameters, ambient temperature and wind velocity using the equations given in the preceding section. Figure 6.5 will be used in the second technical report to solve example problems.

6.5 Annulus Gap Sizing

In typical high temperature absorber tube designs, the rate of energy loss by combined thermal conduction and natural convection in the annulus is of the same order of magnitude as that due to thermal radiation, and can amount to approximately 6% of the total rate at which energy is absorbed by the collector [38]. Therefore elimination or

reduction of conduction and natural convection losses can significantly improve the performance of a collector field.

As mentioned earlier three different techniques can be used for reducing or eliminating these losses. They are:

- . Evacuation,
- . Back-filling the annulus with a heavy gas (gas with low thermal conductivity),
- . Oversizing the annular space (to minimize conduction losses).

Ratzel et. al. [43, 44, 45] have investigated these heat reduction techniques extensively as part of Sandia's PTC development program. Some of their conclusions are:

- . Overall collector efficiency could be improved by 11 to 12 percent if annulus pressures can be maintained below 10^{-2} Pa [35]. However, maintaining a vacuum in the annulus was found to be very difficult.
- . Heavy gas utilization in the annular space can reduce receiver heat-loss by 50 percent. This corresponds to a 4-5 percent improvement in overall collector efficiency [43].
- . The gap size should be made as large as possible while suppressing convection in the annulus, i.e., Rayleigh number should be less than 1000. In Figure sizing of the annulus gap is shown for an absorber temperature of 315°C [41].

In Figure 6.7 sizing of the annulus gap for an absorber temperature of 200°C is shown [36]. (Reference trough receiver data is given in Table 6.1.) As shown, for an evacuated receiver, annulus gap sizing is not thermally significant because no conduction or convection occurs in the annulus.

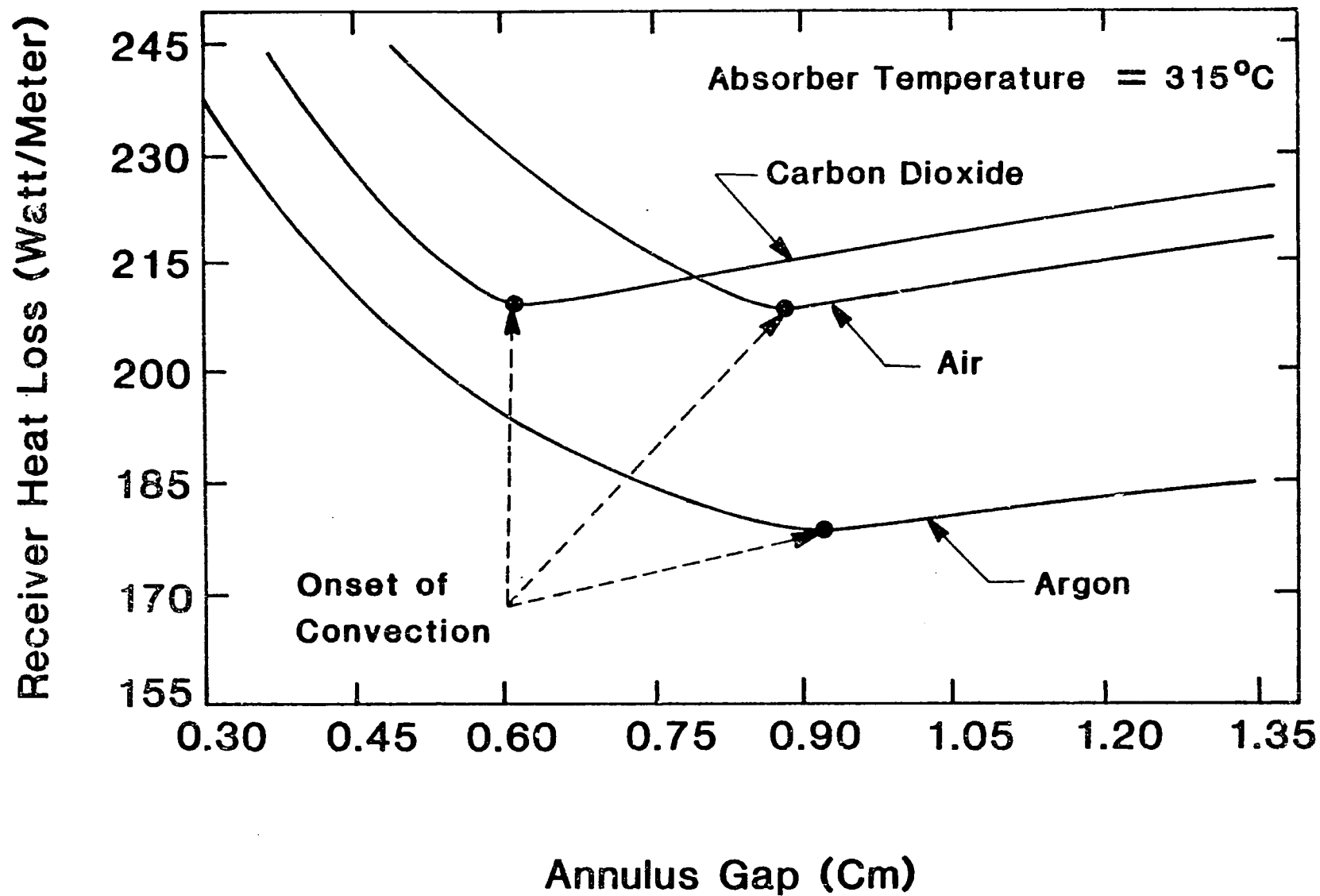
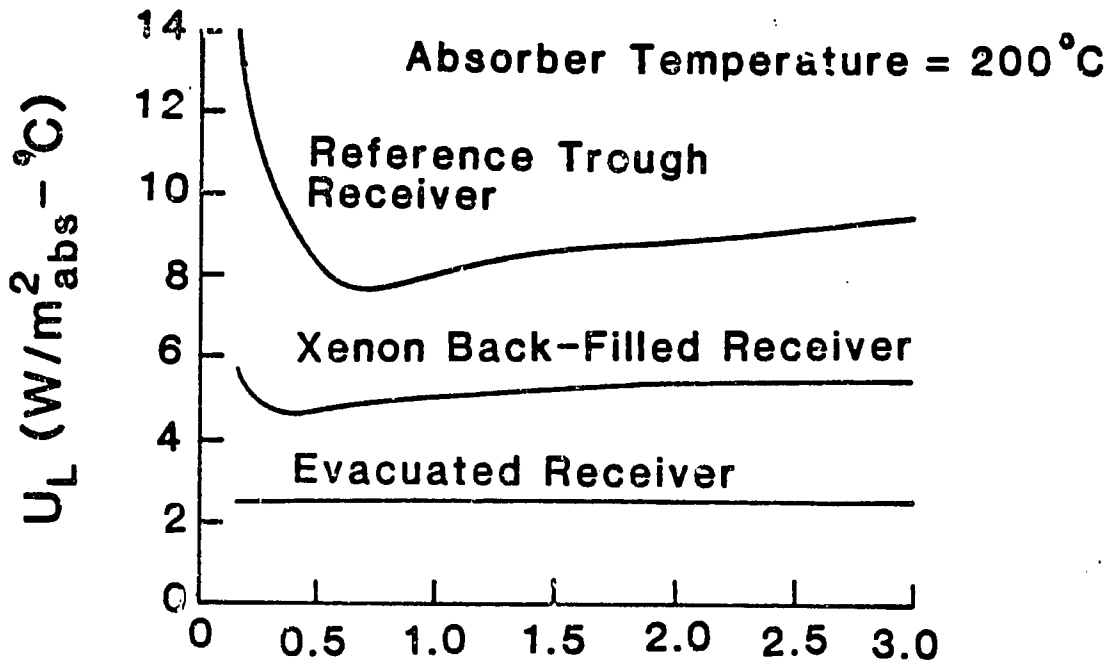


Figure 6.6 Annulus gap sizing for alternate gases using a 2.54 cm absorber tube for an absorber temperature of 315°C (nonevacuated receiver). Source: Ref. 41



Absorber to Glass Gap Size (cm)

Figure 6.7 Annulus gap sizing for an absorber temperature of $200^\circ C$ (from Reference 36).

6.6 Summary

In this chapter, a one-dimensional heat transfer model for the thermal analysis of the receiver subsystem was presented. It was shown that this model could be used to calculate a heat-loss parameter q_L in W per m^2 of receiver surface area to characterize the thermal behavior of the receiver. It was shown that the presented thermal analysis could be used to size the annulus gap size. The method developed in this chapter can be used in a comprehensive design and optimization method. This is demonstrated by illustrative examples in the second technical report.

Chapter Seven

CLOSURE

The need for comprehensive models for optical and thermal analysis of PTC's to be used in comprehensive design studies was established in this report. It was shown that available PTC optical models were not comprehensive; they had restrictive assumptions which limited their usefulness in a comprehensive design method which could be used for design of PTC's in developing country design environments. In this report, the development of a comprehensive optical model for PTC's was presented.

In the presented optical model particular emphasis was placed on the modeling of different kinds of errors (operational, manufacture, assembly, materials, etc.). Errors were divided into two groups as random and non-random. One random and two non-random error parameters were used to characterize different kinds of errors. Subsequently, error parameters were combined with geometric parameters (concentration ratio, C , and absorber diameter D) to yield error parameters universal to all collector geometries. These parameters were called 'universal error parameters'. The results of the developed optical model were presented using the universal error parameters.

A thermal model suitable for design and optimization purposes was also presented. The use of the results of the thermal analyses available in the literature in a comprehensive design method was discussed too.

It was concluded that the optical and thermal models presented in this report are comprehensive models which can be used in a comprehensive design method. Furthermore, it was shown that the

optical model will enable a designer to incorporate error tolerances into the trough design at preliminary stage of the design process. The concept of error tolerances is particularly useful when designing PTC's for developing countries.

An experimental study to investigate the effect of non-random (systematic) errors on the performance of the trough is highly recommended. (No such data was found to exist in the literature.) Such a study will help validate the modeling of the non-random errors presented in this report. A study to investigate the wind induced parallel-flow heat loss from receiver (see Figure 6.4b) is also recommended.

REFERENCES

1. Güven, Halil M., "A Comprehensive Method for Computer-Aided Design of Practical Energy Systems", Doctoral Dissertation, Department of Mechanical Engineering, University of Houston - University Park, December 1983.
2. Kreith, F., Bezdek, R., "Can Industry Afford Solar Energy?", Mechanical Engineering, March 1983
3. Kreith, F., "Solar One", J. of Solar Energy Engineering, v. 104:209, 1982.
4. Kreith, F., "Solar Energy for Developing Countries", J. of Solar Energy Engineering, v. 102:174, 1980.
5. Banas, J. F., "Technology Assessment: Line-Focus Concentrators" SAND 79-2221, Sandia Laboratories, Albuquerque, N.M., 1980.
6. Tabor, H., "Solar Energy Collector Design", Bulletin of the Research Council of Israel, N5C, No.1 (1955).
7. Löf, G. O. G., Fester, D. A., Duffie, J. A., "Energy Balance on a Parabolic Cylinder Solar Collector" Journal of Engineering Power, Transactions ASME Series A 84, 24, 1962.
8. Hassan, Kamal-Eldin, and El-Refaie, M. F., "Theoretical Performance of Cylindrical Parabolic Solar Concentrators", Solar Energy, Vol. 15, No. 3, September 1973, pp. 219-244.
9. Edenburn, M. W., "Performance of a Focusing Cylindrical Parabolic Solar Energy Collector: Analysis and Computer Program" SLA-74-0031, Sandia Laboratories, Albuquerque, N.M. July 1974
10. McCulloch, W. H., Treadwell, G. W., "Design Analysis of Asymmetric Solar Receivers", SAND 74-0124, Sandia Laboratories, N.M. August 1974.
11. Treadwell, G. W., "Selection of Parabolic Solar Collector Field Arrays" SAND-74-0376, Sandia Laboratories, Albuquerque, N.M., May 1975.
12. Treadwell, G. W., McCulloch, W. H., Rusk, R. S., "Test Results from a Parabolic Cylindrical Solar Collector", SAND 75-5333, Sandia Laboratories, Albuquerque, N.M. July 1975

13. Ratzel, A. C., "Receiver Assembly Design Studies for 2-m 90° Parabolic-Cylindrical Solar Collectors," SAND 79-1026, Sandia Laboratories, Albuquerque, N.M., 1979.
14. Treadwell, G. W., Grandjean, N. R. and Biggs, F., "An Analysis of the Influence of Geography and Weather on Parabolic Trough Solar Collector Design," SAND 79-2032, Sandia Laboratories, Albuquerque, N.M., 1980.
15. Treadwell, G. W., "Design Considerations for Parabolic Cylindrical Solar Collectors," SAND 76-0082, Sandia Laboratories, Albuquerque, N.M., 1976.
16. Bendt, P., Rabl, A., Gaul, H., and Reed, K. A., "Optical Analysis and Optimization of Line Focus Solar Collectors," SERI/TR 34-092 Solar Energy Research Institute, Golden, CO., September 1979.
17. Pettit, R. B., and Butler, B. L., "Laser Ray Trace and Bi-Directional Reflectometry Measurements of Various Solar Concentrators," Solar Concentrating Collectors, Georgia Tech, pp. 6-31 - 6-40, 1978.
18. Gaul, H., and Rabl, A., "Incidence-Angle Modifier and Average Optical Efficiency of Parabolic Trough Collectors," Transaction of ASME, Journal of Solar Energy Engineering, Vol. 102, pp 16-21, Feb. 1980.
19. Evans, D. L., "On the Performance of Cylindrical Parabolic Solar Concentrators with Flat Absorbers," Solar Energy, Vol. 19, pp 379-385, 1977.
20. Wen, L., Huang, L., Poon, P. and Carley, W., "Comparative Study of Solar Optics for Paraboloidal Concentrators," Transactions of ASME, J. of Solar Energy Engineering, Vol. 102, pp. 305-315, November 1980.
21. Biggs, F. and Vittitoe, C. N., "The Helios Model for the Optical Behavior of Reflecting Solar Concentrators," SAND 76-0347, Sandia Laboratories, Albuquerque, N.M., Mar. 1979.
22. Pettit, R.B., Vittitoe, C. N. and Biggs, F., "Simplified Calculational Procedure for Determining the Amount of Intercepted Sunlight in an Imaging Solar Concentrator," Transactions of ASME, J. of Solar Energy Engineering, Vol. 105, 1983.
23. Grether, D. and Hunt, A., "Description of the LBL Reduced Data Base and Standard Profiles," Lawrence Berkeley Lab., Aug. 9, 1977, or see [27] pp. 123.

24. Siegel, R. and Howell, J. R., Thermal Radiation Heat Transfer, McGraw-Hill, 1972.
25. Pettit, R. B., "Characterization of the Reflected Beam Profile of Solar Mirror Materials," Solar Energy, Vol. 19, No. 6, 1977.
26. Treadwell, G. W. and Grandjean, N. R., "Systematic Rotation and Receiver Location Error Effect on Parabolic Trough Annual Performance," SAND 81-0159, Sandia Laboratories, Albuquerque, N.M., april 1981.
27. Kreider, J. F., Medium and High Temperature Solar Processes, Academic Press, 1979.
28. Butler, B. L. and Petit, R. B., "Optical Evaluation Techniques for Reflecting Solar Concentrators," Society of Photo-Optical Instrumentation Engineers (SPIE) Vol. 114, Optic Applied to Solar Energy Conversion, 1977.
29. Bendt, P., Gaul, H. and Rabl, A., "Determining the Optical Quality of Focusing Collectors without Laser Ray Tracing," Transactions of ASME, J. of Solar Energy Engineering, Vol. 102, pp.128-133, May 1980.
30. Jeter, S. M., Jarrar, D. I. and Moustafa, S. A., "Geometric Effects on the Performance of Trough Collectors," Solar Energy, Vol. 30, No. 2, pp.109-113, 1983.
31. Dudley, V. E. and Workhoven, R. M., "Summary Report: Concentrating Solar Collector Test Results Collector Module Test Facility," Albuquerque, N.M., Sandia Laboratories, 1978.
32. Biggs, F., EDEP: "A Computer Program for Modeling the Parabolic Trough Solar Concentrator," unpublished notes provided by G. W. Treadwell, Sandia Laboratories Albuquerque, N.M., (1978).
33. Güven, H.M. and Bannerot, R.B., "Comprehensive Error Analysis and Derivation of Universal Error Parameters for Parabolic Troughs," in preparation (to be published in 1985).
34. Rabl, A., Bend, P. and Gaul, H. W., "Optimization of Parabolic Trough Solar Collectors," Solar Energy, Vol. 29, No. 5, pp. 407-417, 1982.
35. Ratzel, A. C., "Evaluation of the Evacuated Solar Annular Receivers Used at the Midtemperature Solar Systems Test Facility (MSSTF)", SAND 78-0983, Sandia Laboratories, Albuquerque, N.M., July 1979.

36. Gee, R., Gaul, H. W., Kearney, D., Rabl, A., "Long Term Average Benefits of Parabolic Trough Improvements", SERI/TR-632-439, Solar Energy Research Institute, Golden, Co., March 1980.
37. Kreith, F., Kreider, J. F., Principles of Solar Engineering, New York, McGraw Hill, 1978.
38. Ratzel, A. C., Hickox, C. E., and Gartling, D. K., "Energy Loss by Thermal Conduction and Natural Convection in Annular Solar Receivers", Thermal Conductivity, Edited by Vladimir V. Mirkovich, Plenum Publishing Company, N.Y., 1978.
39. Kraussold, H., "Wärmeabgabe von zylindrischen Flüssigkeitsschichten bei natürlicher Konvektion", Forsch Hft. Ver. Dt. Ing., Vol. 5, No. 4, 1934, pp. 186-191.
40. Keuhn, T. H., and Goldstein, R. J., "Correlating Equations for Natural Convection Heat Transfer Between Horizontal Circular Cylinders", Int. J. Heat Mass Transfer, Vol. 19, 1976, pp. 1127-1134.
41. Ratzel, A. C., Hickox, C. E., and Gartling, D. K., "Techniques for Reducing Thermal Conduction and Natural Convection Heat Losses in Annular Receiver Geometries", J. of Heat Transfer, vol. 101, 1979, pp. 108-113.
42. Hilpert, R., "Wärmeabgabe von geheizten Drähten und Rohren im Luftstrom", Forsch. a.d. Geb. d. In genieurwes., vol. 4, 1933, p. 215.
43. Ratzel, A. C., "Utilization of Heavy Fill Gases in Annular Solar Receiver Geometries for Heat Loss Reduction", ASME paper No. 79-WA/Sol-18, 1980.
44. Ratzel, A. C., Sisson, C. E., "Annular Solar Receiver Thermal Characteristics", SAND 79-1010, Sandia Laboratories, Albuquerque, N.M., October 1980.
45. Ratzel, A. C., Simpson, C., "Heat Loss Reduction Techniques for Annular Solar Receiver Designs", SAND-78-1769, Sandia Laboratories, Albuquerque, N.M., February 1979.